4418

UNIVERSITY OF HAWAII LIBRARY

INTERANNUAL VARIATIONS OF THE BOREAL SUMMER INTRASEASONAL OSCILLATION

A DISSERTATION SUBMITTED TO THE GRADUATE DIVISION OF THE UNIVERSITY OF HAWAII IN PARTIAL FULFILLMENT OF THE REQUIREMENTS FOR THE DEGREE OF

DOCTOR OF PHILOSOPHY

IN

METEOROLOGY

December 2003

By

Haiyan Teng

Dissertation Committee:

Bin Wang, Chairperson
Thomas A. Schroeder
Fei-Fei Jin
Tim Li
Bo Qiu

Table of Contents

1 Introduction **1**

1.1 Previous studies 1

1.1.1 The MJO and ENSO 5

1.1.2 Intraseasonal and interannual variations of the Indian summer monsoon 8

1.2 Objective and research approach 10

1.3 Dissertation organization 11

2 Data **12**

2.1 The NCEP/NCAR Reanalysis 13

2.2 The CMAP data 13

2.3 The OLR data 14

2.4 The 29 Indian subdivision monthly rainfall 15

2.5 The JTWC's best tracks 15

2.6 The TMI data 15

2.7 QuikSCAT wind 18

2.8 Indices 18

3 Finite domain wavenumber-frequency analysis **21**

3.1 Wavenumber-frequency analysis 22

3.2 Wavenumber-frequency analysis in a finite domain 24

3.3 Other supporting analysis methods 26

4 Characteristics of the Summertime ISO **27**

4.1 Distinct summertime characteristics 27

4.2 The interannual variations 32

5 The Madden-Julian Oscillation **46**

5.1 Seasonal-dependence of the MJO's interannual variability 46

5.2 The interannual variations of the early-summer MJO 50

5.2.1 Relationship with the seasonal mean state 51

5.2.2 Comparison with Slingo et al. (1999) index 52

6 How does ENSO affect the WNP ISO? **67**

6.1 Westward propagating ISO index 67

6.2 Northward propagation 69

6.3 Why is the western North Pacific ISO intimately linked to ENSO? . 72

6.4 How does ENSO affect the phase of the WNP ISO? 75

6.5 Roles of atmosphere-ocean interaction 80

7 Intraseasonal and Interannual Variations of the Indian Summer Monsoon **97**

7.1 Satellite-observed northward propagating ISO 97

7.2 Interannual variations of the northward propagating ISO 106

7.2.1 The northward propagating ISO index 106

7.2.2 Sensitivity test 108

7.3 Mechanism for the interannual variations of the ISO: the mean state . 109

7.3.1 ENSO 112

7.3.2 Indian Ocean SST 113

7.3.3 Mean vertical shear 115

7.4 Relationship with the Indian summer monsoon intensity 117

7.4.1 Indian rainfall 118

7.4.2 Monsoon circulation 119

7.5 Conclusion 120

8 Summary and Future Work **149**

8.1 Tasks performed in this study 149

8.2 Major results 150

8.3 Limitations of this study 153

8.4 Future work 154

List of Figures

2.1 2000-2002 May-September mean SST from (a) the TMI, (b) the NCEP Reanalysis and the 3-year mean standard deviation of the 20-50-day anomalies in May-September from (c) the TMI, (d) the NCEP Reanalysis. 19

2.2 Same as Fig. 2.1 but for the precipitation rate (mm/day) of the TMI (left) and the NCEP Reanalysis (right). 20

4.1 Standard deviation of 20-70 day CMAP (Xie and Arkin 1996) in (a) May-October and (b) November-December averaged for the period of 1979-2001. It denotes the intensity of the intraseasonal variability. Contour levels are 6, 9, 12 mm/day. The length of the vector is the maximum one-pentad lag correlation coefficient between a given grid and its surrounding grid points. The direction indicates the propagation tendency of the ISO. Only those vectors that are significant at the 95% confidence level (correlation coefficients of ± 0.14 (Lau and Chan 1986)) within the 6 mm/day contour are plotted. 35

4.2 Same as Fig. 4.1 but for (a) May-Jul and (b) Aug-Oct. 36

4.3 1979-2001 averaged wavenumber-frequency spectrum for OLR at the equator in (a) May-Oct and (b) Nov-Apr. The longitude domain is 40°E-120°W. 37

4.4 Same as Fig. 4.3 but for sepctrum at 15°N. 38

4.5 First EEOF mode of 20-70-day CMAP (shading) and 850 hPa zonal wind (contour) at from $t-4$ pentad to $t+4$ pentad in November-April, 1979-2001. 39

4.6 Same as Fig. 4.5 but for CMAP and 200 hPa zonal wind. 40

4.7 Same as Fig. 4.5 but for May-October. 41

4.8 Same as Fig. 4.6 but for May-October. 42
4.9 (a) 1979-2001 averaged boreal summer ISO intensity and (b) the 23-year standard deviation of May-Oct seasonal mean in CMAP. Both units are (mm/day). 43
4.10 1979-2001 interannual standard deviations of the boreal summer ISO intensities using (a) CMAP, (b) 850 hPa zonal wind and (c) 850 hPa meridional wind. The unit is mm/day, m/s and m/s for (a), (b) and (c), respectively. 44
4.11 Linear correlation coefficients between May-Oct Niño3.4 SST anomaly and the summer ISO intensities in (a) CMAP during 1979-2001, (b) 850 hPa zonal and (c) meridional winds during 1958-2001. Shading indicates the 95% confidence level. Contours with values between -0.2 and 0.2 are omitted. 45

5.1 The Slingo et al. (1999) MJO index. 55
5.2 1979-2001 averaged ISO intensity in Jan-Mar, Apr-Jun, Jul-Sept, and Oct-Dec. The ISO intensity is defined as the standard deviation of the 20-70-day CMAP anomalies. The unit is mm/day. 56
5.3 1979-2001 mean spectra as a function of latitude and period for zonally propagating wavenumber-1 OLR anomalies in (a) Jan-Mar, (b) Apr-Jun, (c) Jul-Sept, and (d) Oct-Dec. The longitudinal domain is shown in Fig. 5.2. 57
5.4 1979-2001 MJO index in the four seasons. The index is defined as the mean spectrum density of the eastward propagating 20-70-day OLR anomalies. 58
5.5 Correlation coefficients between the MJO index and the ISO intensity in Fig. 5.2. 59
5.6 May-Jul MJO index in 500 hPa vertical velocity (solid) during 1958-2001, the OLR MJO index (dash) during 1979-2001 and May-Jul mean Niño3.4 SST anomaly (bar) during 1958-2001. The MJO index is defined as the mean spectrum density for 20-50-day eastward propagating wavenumber-1 (at 40°E-180°E) anomalies averaged at 2.5°S-5°N for the vertical velocity and at 5°S-10°N for OLR. 60

5.7 The *Hovmöller* diagrams of OLR anomalies averaged at 10°S-10°N in the years of stronger May-Jul MJO (1982, 1987, and 1997) and the weaker MJO (1983, 1984, 1988, 1989, 1998, 1999). 61
5.8 Correlation coefficients between the May-Jul MJO index and May-Jul mean CMAP rainfall (upper panel) and the total ISO intensity during May-Jul (lower panel). 62
5.9 Correlation coefficients between the May-Jul MJO index (using OLR) and May-Jul mean SST during the period of 1979-2001. 63
5.10 The upper panel is the global average (10°S-10°N) 200 hPa zonal wind, the 20-100-day intraseasonal component, and the Slingo et al. (1999) index in the year of 1987. The middle and lower panels are the *Hovmöller* diagrams of the zonal wind and its 20-100-day component. 64
5.11 Same as Fig. 5.10 but for the year 1998. 65
5.12 Comparison of the Slingo et al. (1999) index with the present MJO index in the boreal winer (upper panel) and summer (lower panel). . 66

6.1 1958-2001 July-October mean Niño3.4 SST anomaly (bar) and mean spectrum density of 10-50-day wavenumber1-3 (at 100°E-180°E) westward propagating 850 hPa meridional wind anomaly (dash) averaged at 5°N-20°N. Wavenumber 1 corresponds to wavelength of 80 deg of longitude. 81
6.2 Correlation coefficients between 1958-2001 Niño3.4 SST anomaly and spectrum density of the westward propagating intraseasonal anomalies of v_{850} as a function of latitude and period. (a)-(c) are for wavenumber-1, wavenumber-2, wavenumber-3 westward propagating anomalies within 100°E-180°E, respectively. Shading indicates the 95% confidence level. Contours with values between -0.2 and 0.2 are omitted. 82
6.3 (a) Mean and (b) standard deviation of 1958-2001 spectra as a function of longitude and period for wavenumber-1 northward propagating 850 hPa zonal wind anomalies in May-October. The reference map shows the meridional spatial decomposition domain (5°S-25°N) and longitudinal domain of interest. 83

6.4 Linear correlation coefficients of the spectrum density for the wavenumber-1 northward propagating u_{850} anomalies with reference to Niño3.4 SST anomaly in the period of 1958-2001. Shading indicates the 95% confidence level. 9-point smoothing has been applied on the coefficients. . 84
6.5 Same as Fig.10 but for correlation with OLR spectrum during 1979-2001. Contours with values between -0.2 and 0.2 are omitted. 85
6.6 Correlation coefficients between the boreal summer ISO intensity and May-Oct seasonal mean both using 850 hPa zonal wind in the period of 1958-2001. Shading indicates the 95% confidence level. Contours with values between -0.2 and 0.2 are omitted. 86
6.7 (a) 1958-2001 May-October averaged $u_{850}-u_{200}$ shear; (b) May-October $u_{850}-u_{200}$ shear difference between 7 strong El Niño summers (63, 65, 72, 82, 87, 91, 97) and 7 strong La Niña summers (64, 70, 73, 75, 88, 98, 99). Shading indicates two-sample t-test's 95% confidence level. . 87
6.8 The dominant SVD mode between Jul-Oct mean $u_{850}-u_{200}$ vertical wind shear and the v_{850} boreal summer ISO intensity in Jul-Oct 1979-2001. They account for 84.6% of the total covariance, compared with 5.6% from the second dominant mode. The dominant mode of the vertical shear (a) contributes to 49.4% of its total variance. The dominant mode of the boreal summer ISO intensity (b) contributes to 26.5% of its total variance. Correlation between the two temporal coefficients of the first SVD mode is 0.94. 88
6.9 Fractional variance that the first SVD mode (Fig.6.8) contributes to the interannual variance of a) the mean $u_{850}-u_{200}$ and b) the boreal summer ISO intensity using v_{850} at each individual grid point in Jul-Oct from 1979 to 2001. The values are in percentage. Contours with values below 20 are omitted. 89
6.10 Domain (120°−150°E, 10°−20°N) average of 1958-1999's climatological NCEP 850 hPa vorticity and 1979-1999's climatological CMAP (upper panel) and total numbers of tropical depression, tropical storm, and typhoon at this domain in 1958-1999. 90

6.11 Composites for 850 hPa relative vorticity in 21 warm (solid line) and 21 cold (dash line) summers from 1958 to 1999. Warm/cold summers are defined as that with June-October averaged Nino3,4 SST anomaly above/below zero. Dots denote two-sample t-test's 95% significant level. 91
6.12 Total numbers of tropical depression, tropical storm, and typhoon that have stayed at least 5 days in the domain of $120° - 150°$E, $10° - 20°$N, in 21 warm summers (upper panel) and 21 cold summers (lower panel). The definitions of warm and cold summers are same as Fig.6.11 . . . 92
6.13 Same as Fig.6.12 but for 7 El Nino summers and 7 La Nina summer. 93
6.14 Domain averaged 850 hPa vorticity at $120° - 150°$E, $10° - 20°$N for 7 El Nino summers and La Nina summers. 94
6.15 Composite of 850 hPa vorticity in three selected period, in 7 El Nino summers and 7 La Nina summers. Shading indicates T-test's 95% and 90% significance levels. 95
6.16 Composite of domain ($120° - 150°$E, $10° - 20°$N) averaged NCEP skin temperature (upper panel) and surface total shortwave radiation (lower level) in 9 warm summers (82, 86, 87, 90, 91, 92, 93, 94, 97, with June-October Nino3,4 SST anomaly above zero) and 9 cold summers (83, 84, 85, 88, 89, 95, 96, 98, 99) from 1982-1999. Solid and dash lines represent the composites in warm and cold summers respectively. Dots denotes two-sample t-test's 95% significant level. 96

7.1 Domain averaged 20-50-day TMI rainfall (mm/day) at 75E-100E,5S-5N in May-September, 1999, 2000 and 2001. 128
7.2 The contours are the composite of TMI 20-50-day rainfall (mm/day) at from phase $-\pi$ to $3\pi/4$. Shading indicates the 90% confidence level. The vectors are the composite of QuikSCAT wind. Only those are significant at the 90% level are drawn. 129
7.3 Composite of the NCEP Reanalysis precipitation rate (mm/day) at the 8 phases. 130

7.4 Vertical crosssection at 90°E at phase (a) $\pi/4$, (b) $\pi/2$, (c) $3\pi/4$, (d) $-\pi$, (e) $-3\pi/4$, and (f) $-\pi/4$. The three colums are vertical velocity (Pa/s), divergence (s^{-1}), and specific humidity (g/kg). The black shading is the TMI rainfall anomaly at 90°E, which indicates the latitude of the maximum convection center. Yellow shading indicates the 90% confidence level. 131
7.5 Same as Fig. 7.2 but for TMI SST. 132
7.6 Same as Fig. 7.5 but for 850 hPa zonal wind of the Reanalysis dataset. 133
7.7 The northward propagating ISO index from 1948 to 2001. 134
7.8 Hovemuller diagram of 8 selected years with the strongest northward propagating ISO. 135
7.9 Same as Fig. 7.8 but for the years with the weakest ISO. 136
7.10 Difference of May-Sept mean in (a) CMAP, (b) NCEP 850 hPa and (c) 200 hPa wind between 10 years with the ISO index > 0 and 13 years with the ISO index < 0. Shading indicate the 90% confidence level using two-sample student's t-test. 137
7.11 The anomalous wind response at 850 hPa (b) and 200 hPa (c) to a heating (a) put at the surface of the equatorial eastern Indian Ocean. The maximum amplitude of the heating rate is $2°Cday^{-1}$. 138
7.12 The dominant SVD mode between May-Sept mean CMAP and the CMAP boreal summer ISO intensity in May-Sept 1979-2001. They account for 39.7% of the total covariance, compared with 14.7% from the second dominant mode. The dominant mode of the mean CMAP (a) contributes to 22.6% of its total variance. The dominant mode of the boreal summer ISO intensity (b) contributes to 14.6% of its total variance. Correlation between the two temporal coefficients of the first SVD mode is 0.81. 139
7.13 Fractional variance that the first SVD mode (Fig. 7.12) contributes to the interannual variance of a) the May-Sept mean CMAP and b) the boreal summer ISO intensity using CMAP at each individual grid point in May-Sept from 1979 to 2001. The values are in percentage. 140
7.14 Scatter plot of the 20-50-day mean variance of the northward propagating zonal wind vs. Nino3.4 SST. The upper, middle and lower panel are for the zonal wind at 700, 850, and 925 hPa respectively. 141

7.15 Same as Fig. 7.10 but for the composite difference between yeas with May-Sept Nino3.4 smaller (1981, 1984, 1985, 1988, 1989, 1995, 1996, 1998, 1999, 2000) and larger (1979, 1980, 1982, 1983, 1986, 1987, 1990, 1991, 1992, 1993, 1994, 1997 and 2001) than zero. 142
7.16 (a) Same as Fig. 7.10 but for SST; (b) Domain averaged CMAP (dash) and SST (solid) at 90°E-105°E, 10°S-5°S and Nino3.4 SST anomaly during 1979-2001. 143
7.17 The dominant SVD mode between May-Sept mean SST and the CMAP boreal summer ISO intensity in May-Sept 1979-2001. They account for 50.3% of the total covariance, compared with 22.0% from the second dominant mode. The dominant mode of the mean SST (a) contributes to 36.5% of its total interannual variance. The dominant mode of the boreal summer ISO intensity (b) contributes to 12.7% of its total interannual variance. Correlation between the two temporal coefficients of the first SVD mode is 0.79. 144
7.18 a) average and b) standard deviation of $u_{850} - u_{200}$ vertical wind shear during 1948-2001. 145
7.19 Same as Fig. 7.10 but for $u_{850} - u_{200}$ zonal wind shear. 146
7.20 Map of the 29 India subdivisions. 147
7.21 May-September Variance of 20-50-day Wang and Fan index (solid) and the northward propagating ISO index (dash). The 54-year correlation coefficient of the two time series is 0.68. 148

8.1 Schematic diagram that describes how El Niño modifies (a) the May-Jul MJO and (b) the northwestward propagating ISO in Jul-Oct. Solid and dash contours indicate the region where (a) May-Jul and (b) Jul-Oct mean CMAP rainfall has positive and negative correlation with May-Oct mean Nino3.4 SST anomaly. Shading within the contour shows correlation above the 95% confidence level. Black arrow denotes that (a) the MJO is enhanced in May-Jul and (b) the northwestward propagating ISO is enhanced over the western North Pacific in Jul-Oct in an El Niño summer. 156

ACKNOWLEDGEMENTS

I am deeply indebted to my advisor, Dr. Bin Wang for his long-term support, encouragement and guidance.

Thanks also go to the other committee members: Drs. Thomas A. Schroeder, Tim Li, Fei-Fei Jin and Bo Qiu for their interests in this study and academic advices.

My gratitude must go to the departmental friends, Liguang, Xiaowei, Cliff, Bo and many others for their friendship and encouragement. I thank my church friends from the bottom of my heart for their prayers.

I thank my parents for devoting their lives to me and being my best friends.

This study could not have been finished without love and support from my husband Xiaodong and my son Au.

Finally, I give thanks to the Lord for his love and grace.

ABSTRACT

A new diagnostic approach based on wavenumber-frequency spectral analysis was proposed for the boreal summer intraseasonal oscillation (ISO). The wave characteristics of the MJO, the northwestward-propagating ISO in the western North Pacific (WNP) and the northward-propagating ISO in the Indian Ocean are subjectively measured.

The strongest interannual variations of the ISO are found in the off-equatorial western North Pacific. In summers when *El Niño* is developing, both the westward and northward propagating waves with periods of 15-40 days and 8-10 days are enhanced in July-October.

ENSO affects the northwestward-propagating ISO in the WNP by changing the mean vertical shear in the zonal wind. During July-October in *El Niño* developing years, the easterly vertical zonal-wind shears over the tropical western Pacific are considerably increased, in contrast to a westerly-vertical-shear mean state in the *La Niña* years. The easterly vertical shear promotes development and northwestward emanation of Rossby waves away from the equatorial western-central Pacific in the lower troposphere, reinforcing the WNP ISO.

The stronger WNP ISO in *El Niño* summers cools the local SST. The WNP SST drops under the climatology at the climatological wet phases in the warm summers, while it is sustained above the climatology in the cold summers.

In the Indian summer monsoon region, the life cycle of the northward-propagating

ISO was revealed by QuikSCAT and TRMM satellite data. The composite scenario suggests that the intraseasonal convective anomalies are first generated in the equatorial Indian Ocean between 60°E-70°E, associated with the low-level convergence and upper-level divergence at the monsoon's break phase. The anomalies then propagate eastward and intensify at 70°E-100°E about 10 days later. Thereafter, the northward propagation takes place in two steps: At the first step, Rossby waves are emanated from the equatorial convection and propagate northwestward to 15°N, 70°-90°E in less than 10 days. There is also a Rossby-wave response center in the southern hemisphere. During the second step, the southeast-northwestward titled rainband moves northeastward to the inner land region and decays. The second step takes about 20 days.

In order to measure the seasonal activity of the northward-propagating ISO, an index was constructed from 1948 to 2001 based on the 20-50-day wavenumber-one northward propagating u850 anomalies averaged at 65°E-90°E. The weak-ISO years are characterized by isolated intraseasonal convection at the equator and 20°N, whereas the two regions are connected by the Rossby-wave-emanation process in the strong ISO years.

The seasonal activity of the northward-propagating ISO is found significantly influenced by the mean convection in the equatorial eastern Indian Ocean (EEIO), which is the source for the Rossby-wave emanation. ENSO modifies the northward-propagating ISO mainly through influencing the mean convection in the EEIO. The

ISO is significantly weaker in *El Niño* developing May-Sept, and stronger in the *La Niña* summer.

The seasonal activity of the northward-propagating ISO is not related to the overall performance of the Indian summer monsoon. Averaged rainfall at the 29 Indian subdivisions were examined from 1948 to 2001. During 1979-2001, two divisions in the southern Peninsular have a positive correlation with the ISO intensity, and 4 divisions in the west central India and central Northeast India have a negative correlation with the ISO intensity. This confirms the ISO-mean rainfall relationship revealed by the CMAP rainfall. But neither the All Indian rainfall index or the monsoon circulation index (Wang et al. 2001) has a significant correlation with the seasonal activity of the northward propagating ISO.

The interannual variations of the MJO have a seasonal dependence. The May-Jul MJO is closely related with ENSO. At *El Niño* 's developing stage, the MJO is enhanced. This is in a sharp contrast with the wintertime MJO, which is not sensitive to the ENSO condition.

Chapter 1

Introduction

1.1 Previous studies

The Madden-Julian Oscillation (MJO; Madden and Julian 1971, 1972) arises from eastward propagating circulation and convection anomalies trapped in the equatorial region. It is the dominant mode of the boreal winter tropical intraseasonal oscillation (ISO). During the boreal summer, the MJO substantially weakens due to northward migration of the warmest sea surface temperature (SST), the inter-tropical convergence zone (ITCZ) and associated maximum boundary-layer moist static energy (Wang and Rui 1990; Li and Wang 1994). Meanwhile, the summertime ISO exhibits prominent northward propagation in the Indian summer monsoon region (Yasunari 1979, 1980; Krishnamurti et al. 1982) and northwestward propagation in the western North Pacific (WNP; Murakami et al. 1984; Lau and Chan 1986). The time scales of the intraseasonal variability in the off-equatorial region are richer

than the MJO. For instance, a 10-20-day westward propagating mode is noted in the off-equatorial Asian summer monsoon region (Krishnamurti and Ardanuy 1980). Higher-frequency variability associated with 6-9 days (Lau and Lau 1990) and 7-21 days (Schrage and Vincent 1996) has also been observed in the WNP. In addition, typhoon activity suggests a 2-3 week periodicity (Frank 1987). All these features (activity centers, frequency, and propagation) indicate that the canonical MJO can not sufficiently represent the boreal summer ISO.

Apart from comprehensive observations (reviewed by Madden and Julian 1994; Wang and Ding 1992), numerous theoretical studies have been carried out to understand the dynamics of the MJO. The MJO is commonly explained by wave-CISK (conditional instability of the second kind; Chang 1977; Lau and Peng 1987; Chang and Lim 1988) and wind-induced surface heat exchange (WISHE; Emanual 1987; Neelin et al. 1987) mechanisms. Wave-CISK assumes that the heating is controlled by low-level moisture convergence. The eastward propagation of the convective envelope is maintained through selective amplification of Kelvin waves. WISHE assumes that the convection develops in the vicinity of enhanced surface momentum and evaporative fluxes to the east of the main center of convection. This maintains the eastward propagation. WISHE is not mutually exclusive of wave-CISK. These theories have been reviewed by Hayashi and Golder (1993). Although both mechanisms can explain the slow eastward propagation, they have their own drawbacks. The wave-CISK theory requires that the large-scale environment is unstable, which

can hardly be satisfied by the reality; For the WISHE theory, the weak westerly or quiescent mean zonal wind in the eastern hemisphere jeopardizes the mean-easterly assumption that the theory is established on. More details of the MJO dynamics have been reviewed by Wang (1992).

It is more challenging to understand the summertime ISO due to its more complicated behavior. Wang and Xie (1997) proposed that the northwestward propagating ISO in the WNP is generated by the decoupling of Kelvin-Rossby wave package at the dateline due to the mean subsidence in the western hemisphere, and by the Rossby wave emanation thereafter. The mean easterly vertical shear at the Asian-Pacific summer monsoon region enhances the Rossby wave in the lower troposphere, leading to the northwestward propagation of the intraseasonal anomalies. Jiang et al. (2003) explained that the mean easterly vertical shear in the Indian summer monsoon region helps to generate barotropic mode from baroclinic mode, which induces boundary layer convergence and leads the ISO to move northward. Meanwhile, both the monsoon mean flow and the intraseaonal wind increase the gradient of specific humidity in the boundary and contribute to the northward propagation. Drbohlav and Wang (2003) found the mean easterly vertical shear can generate the intraseasonal northward propagation in the Asian monsoon region in a 2-D intermediate model. Webster (1983) proposed that the latent heat flux can destabilize the boundary layer ahead of intraseasonal convection over land and lead the northward movement of the convection zone. Furthermore, air-sea interaction may play an important role in the

summertime ISO (Kemball-Cook and Wang 2001). Both JASMINE (Joint Air-Sea Monsoon Interaction Experiment; Webster 2000) and the recent satellite microwave sensor (Vecchi and Harrison 2001) found large intraseasonal variability associated with the ISO. Fu et al. (2003) and Waliser et al. (1999) have demonstrated how an interactive SST can improve the simulation of the ISO, which has been a serious shortcoming of AGCMs (Park et al. 1990; Slingo et al. 1996).

All current theoretical understandings of the ISO are built upon the framework of CISK and tropical wave dynamics (Matsuno 1966; Gill 1980). Fundamental questions still remain: Is the ISO chaotic in nature? Is it an intrinsic atmospheric mode or an atmosphere-ocean coupled mode? How does it react to the slowly varying boundary layer conditions such as SST? While intermediate models and GCMs are taken as an active approach, they have their limitations. Simplicity of the intermediate model undermines the reality of the model-produced ISO. The GCMS suffers from systematic errors in simulating of monsoon or annual cycle (Slingo et al. 1996). The complicated physical processes involved in the GCMs make it difficult to diagnose and improve the simulation. On the other hand, we have accumulated longer than 50 years of the NCEP-NCAR reanalysis data and various other data sources, but a plausible conclusion of how the summertime ISO varies from year to year in the state-of-art observations has not been reached.

Most of the previous investigations regarding the interannual variations of the ISO have targeted on the wintertime MJO. Its relationship with ENSO has gone

through an intense debate. During the boreal summer, the ISO in the Indian summer monsoon region has been a major research interest, due to a possible linkage with the strength of the monsoon. The summertime MJO and the northwestward propagating ISO mode in the WNP have not received much attention. Thus, the previous studies can generally fall into two categories: The MJO-ENSO relationship and the ISO-Indian summer monsoon relationship.

1.1.1 The MJO and ENSO

After the strong *El Niño* of 82/83, Lau and Chan (1986, 1988) first related the MJO to ENSO. Their hypothesis was supported by the observed pattern of the total OLR variance during 82/83. It is similar to the variability on the intraseasonal time scale. A decrease in the intensity of the ISO during the 82/83 event was also documented (Wang and Murakami 1988; Lau and Chan 1988). Gray (1988) used four island records in the Indian Ocean and the Pacific and found the dominant intraseasonal frequency peak changes from ENSO to non-ENSO years. He hypothesized that warmer SST could produce convergence which breaks the equatorial zonal circulation cells into smaller spatial scales and causes the ISO to shift to higher frequencies in ENSO warm events. Gutzler (1991) studied more than twenty years of rawinsonde data from six tropical islands. He found that the 40-50 day variance of equatorial lower-tropospheric zonal wind tends to increase east of the dateline and decrease to the west during an ENSO warm event. However, he was not able to describe the

propagation features because of the sparse distribution of the stations. Applying Complex Empirical Orthogonal Function (CEOF) analysis on the 1974-1988 OLR data, Anyamba and Weare (1995) found that the behavior of ISO during the 82/83 event is quite different from the 76/77 and 86/87 events. Their study suggested that the equatorial east-west dipole structure is responsible for the eastward propagation of the ISO. It is hypothesized that SST may affect the dipole structure, and the eastward propagation of the ISO. Fink and Speth (1997) found the intraseasonal OLR variance is enhanced in ENSO warm events. But they could not confirm whether the local variance is associated with the MJO.

The above studies indicate large interannual variability in the MJO, but they are unable to measure it quantitatively. As a result, the MJO-ENSO relationship became more controversial. In recent years, several MJO indices were developed. Salby and Hendon (1994) proposed a MJO index using a wavenumber-frequency filter to measure the eastward propagating intraseasonal OLR, zonal wind and tropospheric temperature. The MJO activity was found unrelated with ENSO. Hendon et al. (1999) followed the definition of the index. They also defined another MJO index based on the first two EOF modes. Both indices are uncorrelated with ENSO or local SST. Slingo et al. (1999) proposed a MJO index based on variance of 20-100-day global mean zonal wind at 850 hPa. Unlike Hendon et al. (1999) index, this index presents a continuous daily measure of the MJO activity. Besides large interannual variability, it also contains significant seasonal change. Hendon et al.

(1999) have compared their index, which is for the wintertime MJO, with Slingo et al. (1999). They generally agree with each other. Kessler (2001) used the EOF modes to represent the MJO and found the eastward extension of the MJO during ENSO warm events accounts for large intraseasonal variance in the central Pacific.

There are relatively few studies which support that the summertime ISO in the Indian summer monsoon region is modulated by ENSO. They include: In 1972 the active/break cycle of cloudiness was much longer ($\sim$ 60 days) than the years ($\sim$ 30$-$40 days) between 1966 and 1973 (Yasunari 1980); The northward propagation of the low-level ridge and trough over the Indian subcontinent was more regular during the northern summer of 1979, 1982 and 1983 but irregular during for the summers of 1980, 1981 and 1984 (Mehta and Krishnamurti 1988); In 1987, the ISO had stronger and better organized eastward propagations than in 1988 (Vernekar et al. 1993). These results were crucially limited by lack of observations. There was only one ENSO event included. On the other hand, Singh et al. (1992) studied the interannual variability of the ISO using 80 years of daily rainfall data from 365 stations over Indian. Their analysis does not reveal any relationship between the intensity of the ISO and ENSO.

Studies on the interannual variability of the summertime ISO in the WNP are scarce. Nitta (1987) compared several years cloud data and found the intraseasonal northward propagating Pacific-Japan pattern is related to the local SST. But he was unable to identify ENSO's signal due to the short observational records.

Overall, the evidence for a MJO-ENSO linkage is limited to that *El Niño* can

facilitate the wintertime MJO to propagate further eastward to the central Pacific. ENSO does not seem to influence the summertime ISO in the Indian summer monsoon region.

1.1.2 Intraseasonal and interannual variations of the Indian summer monsoon

Because the Indian summer monsoon exhibits strong intraseasonal activity, characterized by active/break cycles with dominant periods of 10-20 days and 30-50 days, it has been long speculated that there is an intimate relationship between the variability at the two different time scales. For example, the extraordinary long Indian monsoon break directly caused the historical drought in 1972 (Yasunari 1980). However, the relationship between the ISO and the interannual variability of the monsoon remains poorly understood after numerous studies. From the previous work, three contradictory conclusions can be drawn:

The first group believes that the ISO and the Indian summer monsoon are the same dynamic mode except that they possess different frequencies. Ferranti et al. (1997) analyzed five 10-year European Centre for Medium-Range Weather Forecasts Atmospheric Model Intercomparison Project integrations, which differ only in the initial conditions. The spatial pattern of both the frequencies is dominated by oscillation between two rain bands: one at 5°N-10°S, and the other at 5°N-20°N. This result is also supported by Goswaimi and Mohan (2001), who analyzed 42-year Re-

analysis data and 24-year OLR data. Increased occurrence of active (break) condition would lead to an enhanced (suppressed) seasonal mean.

The second group examined the long-term rain gauge records in India. They found the ISO intensity is irrelevant with the monsoon strength (Singh 1992; Krishnamurthy and Shukla 2000). The boundary forcing, which Charney and Shukla (1981) postulated to explain the interannual variability of the monsoon rainfall, does not reign on the intraseasonal time scale. Annamalai et al. (1999) examined the intraseasonal and interannual variability using the NCEP/NCAR reanalysis and ECMWF reanalysis. They found the two are different dynamics modes.

The third opinion is that the ISO has an inverse relationship with the Indian summer monsoon. Lawrence and Webster (2001) constructed a 22-year ISO activity index based on wavelet spectrum of the OLR data. The index has a significant negative correlation with the all Indian-rainfall index. They also related the ISO with the averaged OLR at a larger spatial domain, which covers both India and the Bay of Bengal, but found they were not correlated.

All the above review suggests that lack of a good representation of the ISO may have caused the controversial results and hindered revealing the potential mechanisms for its interannual variability. Unlike the MJO, the summertime ISO consists of various propagation patterns at different locations: Equatorial eastward propagation, off-equatorial westward propagation and northward propagation in the Bay of Bengal and the WNP. The above review suggests that the summertime MJO and the ISO in

the WNP are under-investigated. Furthermore, there also exists sub-seasonal change in the ISO's behavior (Kemball-Cook and Wang 2001). None of the previous studies have measured the ISO intensity regarding the above characteristics. Therefore a more accurate document of the summertime ISO is called for.

1.2 Objective and research approach

Since the fundamental features of the interannual variability of the summertime ISO have not been systematically documented, a diagnostic approach is taken in this study. Because lack of a subjective measure of the ISO has been a big obstacle in the previous studies, this study is aimed at building an observational framework for diagnosing the interannual variations of the summertime ISO. The numerical methods can be applied in future to evaluate the GCMs' performance on the intraseasonal time scale. The analysis results of this study can also serve as a benchmark to be compared with. Because how the ISO responses to the large-scale change associated with ENSO and the Indian summer monsoon reveals important dynamic characteristics, the ISO-ENSO, ISO-monsoon relationships will be exclusively examined.

Various statistical analysis methods have been used. Regional wavenumber-frequency spectral analysis is specifically designed and applied to the Asian summer monsoon region to quantify the strength of the eastward, northward and westward propagating ISOs. Other statistical methods, such as singular vector decomposition, EOF analysis are also used.

1.3 Dissertation organization

This dissertation is organized in the following manner. The datasets are introduced in Chapter 2, followed by the analysis methods. In Chapter 4, the climatological characteristics of the summertime ISO are described. The strength of its interannual variability is roughly estimated. The interannual variations of the MJO is examined in Chapter 5. The northwestward propagation of the ISO in the WNP is investigated in Chapter 6. How it varies from year to year, how ENSO modifies the ISO, what role the air-sea interaction plays are addressed. The northward propagating ISO in the Indian summer monsoon region is studied in Chapter 7. Its relationship with the summer mean convection/circulation, and its relationship with the Indian summer monsoon are investigated. The major results are summarized in Chapter 8, followed by some suggestions on future study.

Chapter 2

Data

The primary data sets are 1979-2001 daily OLR (Liemann and Smith 1996) from NOAA operational polar-orbiting satellites, 1979-2001 pentad-mean Climate Prediction Center (CPC) merged analysis of precipitation (CMAP) (Xie and Arkin 1997) and 1948-2001 daily National Center for Environmental Prediction/National Center for Atmospheric Research (NCEP/NCAR) Reanalysis (Kalnay et al. 1996).

Monthly rain gauge records at 29 Indian subdivisions during 1948-2001 have been supplemented to provide longer history of the Indian summer monsoon. The best tracks from the Joint Typhoon Warning Center (JTWC) in the WNP are also employed to describe the tropical storm activity. Some recent (2000-2002) high-resolution satellite data sets are used, which provide an unprecedented life cycle for the ISO. Besides, various indices are employed, such as the Nino3.4 SST index and the all-India rainfall index.

2.1 The NCEP/NCAR Reanalysis

The NCEP/NCAR reanalysis project uses a frozen state-of-the-art analysis system (the Global Data Assimilation System, GDAS) and a forecast model with T63 horizontal resolution and a data base as complete as possible (Kalnay et al. 1996). Because of the unchanged analysis methods and model, the data is expected to be devoid of artificial climate jumps. Yet the quality of the Reanalysis dataset has been dramatically improved in the mid-1970s after satellite observation became available. It requires special cautions to avoid drawing the conclusions upon the early decade' data.

The most comprehensively used variables in the study include winds at 850 and 200 hPa, and the skin temperature as an approximation of SST. Both daily averaged and monthly mean data sets are employed. The period ranges from 1948 to 2001.

2.2 The CMAP data

This dataset consists of monthly-averaged and pentad mean precipitation rates (mm/day) for the period of 1979-2001. It has a global coverage with a 2.5°x2.5° resolution. The CMAP analyses are created by merging several kinds of individual data sources of precipitation, including gauge observations, satellite estimates and optionally, the precipitation fields from the NCEP/NCAR reanalysis (Xie and Arkin 1997).

Two versions of pentad CMAP datasets are created. In the first version, the NCEP/NCAR model output was merged into the observations to ensure a complete global coverage. In the second version, only observation-based input datasets are used so that the resulting merged analyses are clear of any influences from numerical models. In this work, the second version is chosen.

2.3 The OLR data

OLR has been intensively used for the ISO studies. Although the OLR may have contamination from cirrus clouds, surface temperature, and moisture content, it provides a good estimation of deep convection over the tropical ocean.

Archived OLR data from the Advanced Very High Resolution Radiometer (AVHRR), which flew onboard polar-orbiting satellites has been obtained from National Oceanic and Atmospheric Administration (NOAA). The satellite observations are interpolated to $2.5° \times 2.5°$ grids. Detailed descriptions of the data set and the interpolation methods are addressed by Liemann and Smith (1996). In this study daily mean OLR from 1979 to 2001 (averaged from two observations each day) was used.

2.4 The 29 Indian subdivision monthly rainfall

Monthly rainfall at 29 Indian meteorological subdivisions can date back to 1871 (Parthasarathy et al. 1995). The district rainfall is computed from averaging all stations in the district. The period of 1948-2001 is chosen in this study.

2.5 The JTWC's best tracks

The best tracks of the tropical cyclones in the WNP are obtained from the web site of the Joint Typhoon Warning Center (www.npmoc.navy.mil/jtwc.html). The dataset includes the location (longitude and latitude) and wind speed of named tropical storm (maximum sustained wind speed exceeds 17 m/s) for every 6 hour. The resolution of the wind speed is 5 m/s. The dataset in the WNP starts from 1945. After 1965, the data quality is dramatically improved because satellite monitoring of weather events became operational.

2.6 The TMI data

The Tropical Rainfall Measuring Mission's (TRMM) Microwave Imager (TMI) is a passive microwave sensor designed to provide high-resolution quantitative rainfall information over a wide swath under the TRMM satellite. Besides, there are four other sensors onboard: Precipitation Radar (PR), VIRS (Visible Infrared Scanner), LIS (Lightning Imaging Sensor) and CERES (Clouds and the Earth's Radiation En-

ergy System). TMI measures the intensity of radiation at five separate frequencies: 10.7, 19.4, 21.3, 37, 85.5 GHz. It also has a wide swath (780 km), which is more than three times wider than the PR swath. Compared with the previous satellite (Special Sensor Microwave/Imager, SSM/I) which has served the rainfall measuring missions, TRMM has a lower altitude of 350 km (860 km of SSM/I) and a higher spatial resolution. The 10.7 GHz channel was also added to improve the rainfall measurement. The five sensors are complementary. For example, the PR can provide the vertical profile of rainfall. Unfortunately, a collaborated product combining different sensors are still unavailable to the public. In this study, only the TMI is used. It is downloaded from Remote Sensing System (http://www.ssmi.com/).

Six geophysical parameters were derived from TMI including SST, surface wind speeds at two different radiometer channels, atmospheric water vapor, liquid cloud water and precipitation rates. The TMI data was provided as daily maps (separated into ascending and descending orbit segments), 3-day mean maps, weekly mean maps and monthly mean maps. The data are available from December 1997 to the present. All images cover a global region extending from 40°S to 40°N at a pixel resolution of 0.25 deg (25 km). In this study, the most recently updated version-3a 3-day mean data during 2000-2002 was used, which covers most area of the global tropical oceans. The retrieval over land requires more complicated algorithm and is currently unavailable.

Traditional infrared SST observations require a cloud-free field of view, yet the microwave sensor can measure through the clouds. Furthermore, microwave retrievals

are not affected by aerosols and are insensitive to atmospheric water vapor. However, the microwave retrievals are sensitive to sea-surface roughness, while the infrared retrievals are not. A primary function of the TRMM SST retrieval algorithm is the removal of surface roughness effects. Combining the microwave and infrared SST in the future will provide a more reliable SST data set.

Similarly, previous global rainfall estimation (such as CMAP) is calibrated according to the relation of rain gauge data and satellite visible or IR observations. However, TMI and PR directly observe precipitation through clouds by microwaves. Having a larger swath, TMI can observe a broader area. But TMI also has larger uncertainty over land because of the stronger background emission by land. PR gives more accurate rainfall rate over land. It also detect the vertical profile of rainfall.

The TMI SST and precipitation rate are compared with the NCEP/NCAR Reanalysis. Fig.2.1 shows the comparison of SST. The seasonal mean of the two datasets are quite similar. TMI shows stronger intraseasonal variability in the Arabian Sea, the Bay of Bengal and the South China Sea, and the central Indian Ocean south of the Indian Peninsular.

Large difference exists in the precipitation rate between the two datasets. The TMI precipitation rate is higher than the Reanalysis in both the seasonal mean and the ISO intensity. The spatial pattern of the variability centers are different. The eastern equatorial Indian Ocean west of Sumatra is a convection center on both seasonal mean and the intraseasonal time scales. This feature is missed by the Reanalysis.

2.7 QuikSCAT wind

NASA's Quick Scatterometer (QuikSCAT) was lofted into space in June 1999 to fill in the gap created by the loss of NASA Scatterometer (NSCAT) data in 1997. The SeaWinds instrument on the QuikSCAT satellite is a specialized microwave radar that measures near-surface wind speed and direction under all weather and cloud conditions over the oceans. The data is available in quasi-realtime on the NASA site: airsea-www.jpl.nasa.gov. In this study, daily-averaged 1°x1° zonal and meridional winds are employed from 2000 to 2002.

2.8 Indices

1958-2001 CPC Nino3.4 SST anomalies are used to categorize ENSO events. This study focuses on the boreal summer season from May to October; hence *El Niño /La Niña* summers are selected by May-October mean Nino3.4 anomaly above/below one standard deviation (about 0.7°C). Following such a criterion, 63, 65, 72, 82, 87, 91 and 97 are identified *El Niño* summers, 64, 70, 73, 75, 88, 98 and 99 are *La Niña* summers.

1948-2000 all India rainfall index (AIRI) (Parthasarathy et al. 1994) is utilized for categorizing strong and weak monsoons.

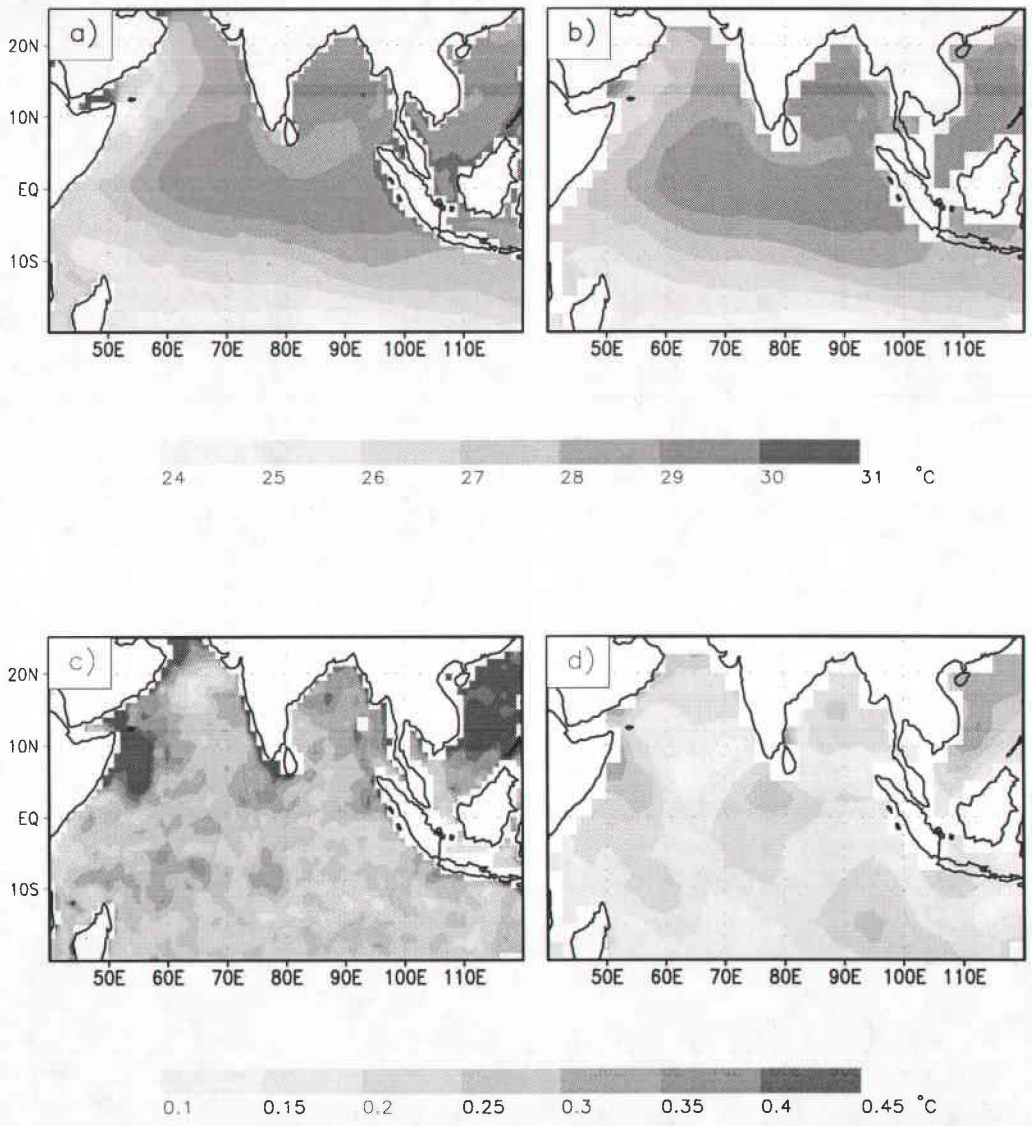

Figure 2.1: 2000-2002 May-September mean SST from (a) the TMI, (b) the NCEP Reanalysis and the 3-year mean standard deviation of the 20-50-day anomalies in May-September from (c) the TMI, (d) the NCEP Reanalysis.

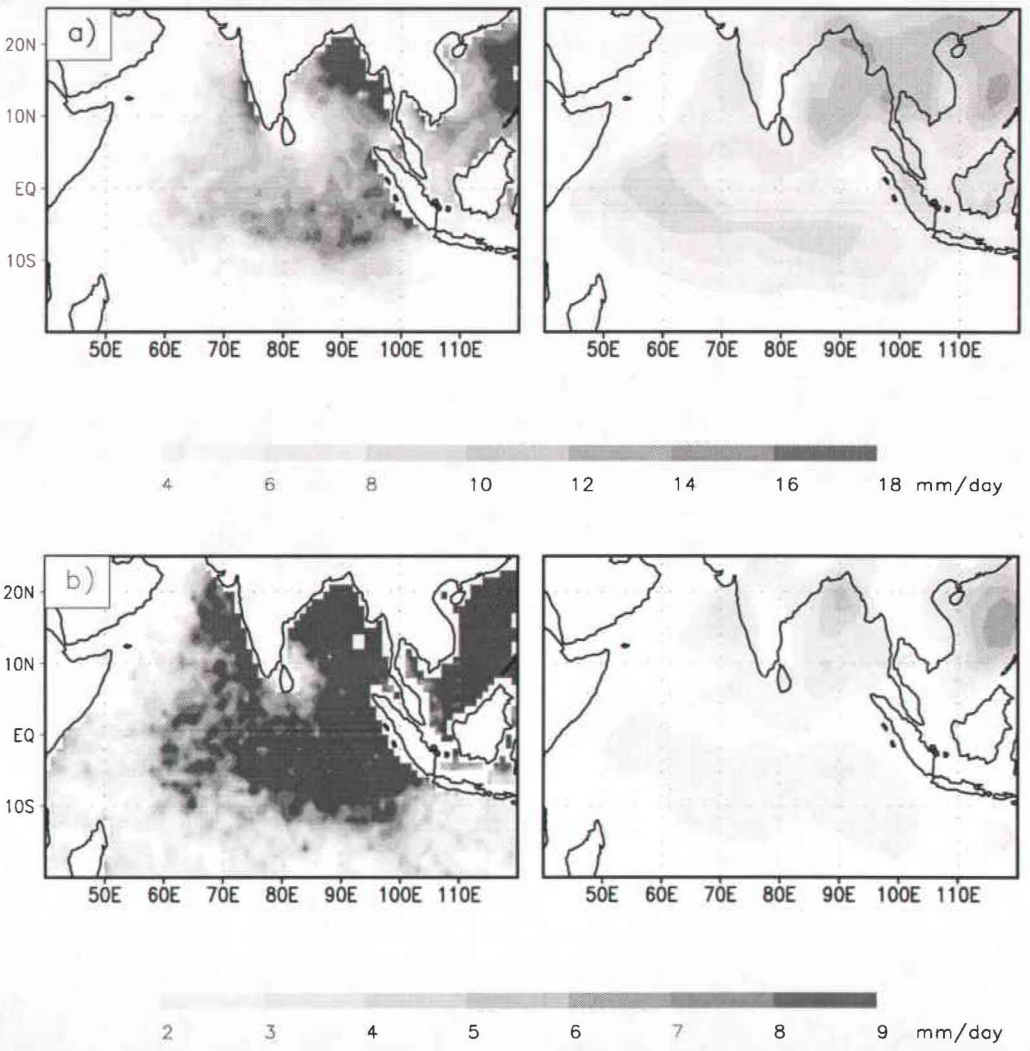

Figure 2.2: Same as Fig. 2.1 but for the precipitation rate (mm/day) of the TMI (left) and the NCEP Reanalysis (right).

Chapter 3

Finite domain wavenumber-frequency analysis

Unlike variations such as ENSO or tropical cyclones, the ISO is more difficult to measure. Quantification of the boreal summer ISO is even more challenging due to its complicated propagation characteristics. Conventional methods, such as *Hovmöller* diagram, extended EOF, or complex EOF analyses have difficulties in quantitatively measuring wave propagation, especially for dispersive waves. The intensity, propagation and frequency, which are intrinsic wave properties are usually studied separately.

Closely resembling the normal mode method in theoretical studies, the wavenumber-frequency analysis transforms a time series from a spatial-temporal domain to a wavenumber-frequency domain. Salby and Hendon (1994) and Hendon et al. (1999) used a wavenumber-frequency filter to measure the intensity of the MJO. Using this

method, Wheeler and Kiladis (1999) identified the dispersion relationship of the tropical waves, verifying in part the theory of Matsuno (1966). But all these studies do not distinguish propagating waves from stationary waves.

In this study, wavenumber-frequency analysis is applied in a finite domain, instead of the conventional global domain, to specifically investigate variance of the propagating intraseasonal anomalies, in both the zonal and meridional directions.

3.1 Wavenumber-frequency analysis

This method has been thoroughly reviewed by von Storch and Zwiers (1999). The original concept was developed by Deland (1964) and Kao (1968, 1970), assuming the wave evolved in a deterministic way. Hayashi (1971, 1982) and Pratt (1976) improved the method by including statistics for the stochastic waves.

The analysis is performed in four steps:

1) In order to separate variability with different spatial (horizontal) scales, the field of interest is decomposed of a time series of sine and cosine functions, assuming a periodic boundary condition at the ends.

$$f(x,t) = \sum_{k=1}^{\infty} (c_{kt} cos(\frac{2\pi kx}{L}) + s_{kt} sin(\frac{2\pi kx}{L})), \tag{3.1}$$

where L is the reference length, which is usually chosen as the circumference of Earth at a given latitude. k denotes the wavenumber. C_{kt} and S_{kt} are the two

Fourier coefficients:

$$c_{kt} = \begin{cases} \int_0^L f(x,t)dx, & k = 0 \\ 2\int_0^L f(x,t)cos(\frac{2\pi kx}{L})dx & k > 0 \end{cases} \tag{3.2}$$

$$s_{kt} = \begin{cases} \int_0^L f(x,t)dx, & k = 0 \\ 2\int_0^L f(x,t)sin(\frac{2\pi kx}{L})dx & k > 0 \end{cases} \tag{3.3}$$

2) The covariance of C_{kt} and S_{kt} at different time scales indicates the propagation direction of the original field. Therefore, the cross-spectrum of C_{kt} and S_{kt} is calculated.

3) The cross-spectrum is divided into variances of the waves propagating in eastward and westward directions. The wavenumber-frequency spectrum is given as:

$$\Gamma_{cs}^{fw}(\omega) = \frac{\Gamma_{cc}(\omega) + \Gamma_{ss}(\omega)}{2} - \Psi_{cs}(\omega), \tag{3.4}$$

where $\Psi_{cs}(\omega)$ is the quadrature spectrum, $\Gamma_{cc}(\omega)$ and $\Gamma_{ss}(\omega)$ is the spectrum density of C_{kt} and S_{kt}, respectively.

4) Hayashi (1982)'s formalism is adopted to attribute the coherent part of the eastward and westward traveling variance to standing waves:

$$\Gamma_{cs}^{st}(\omega) = C(\omega)\sqrt{\Gamma_{cs}^{fw}(\omega)\Gamma_{cs}^{fw}(-\omega)}, \tag{3.5}$$

with

$$C^2(\omega) = \frac{(\Gamma_{cc}(\omega) - \Gamma_{ss}(\omega))^2 + 4(\Lambda_{cs}(\omega))^2}{(\Gamma_{cc}(\omega) + \Gamma_{ss}(\omega))^2 - 4(\Psi_{cs}(\omega))^2}, \tag{3.6}$$

Λ_{cs} is the co-spectrum. The propagating variance is then defined as the remainder.

$$\Gamma_{cs}^{pro}(\omega) = \Gamma_{cs}^{fw}(\omega) - 0.5 * \Gamma_{cs}^{st}(|\omega|) \tag{3.7}$$

3.2 Wavenumber-frequency analysis in a finite domain

Conventionally, the spatial decomposition is carried out along a full latitudinal circle as is granted by the earth's spherical boundary condition. The wavenumbers are discrete integers from 0 to nlon/2, where nlon is the total number of the grid points at a given latitude.

The wavenumber-frequency analysis is extended from a global domain to a finite domain. This is because the boreal summer ISO is effectively trapped in the northern summer monsoon region by the lower-boundary conditions (such as SST, land and ocean surface moisture distribution), and the mean three-dimensional monsoon flows (Wang and Xie 1997). The assumption underlying the regional wavenumber-frequency spectral analysis lies in the fact that these summer ISO modes nearly vanish

at the two ends of certain latitude or longitude domains. Numerous computations have been performed to assure the insensitivity of the results to the choice of the longitude (latitude) domains. Finite domain wavenumber-frequency analysis reveals detailed regional characteristics, which are overwhelmed in the global domain analysis.

For the summertime MJO, the focus is the wavenumber-1 anomaly from 40°E to 180°E in May-July, although its averaged behaviors in May-Oct and Aug-Oct have also been investigated. For the off-equatorial westward propagating ISO, the WNP ISO (100°E-180°E in July-October is intensively studied. Choice of the two different temporal and spatial domains is based on the subseasonal change in the ISO's characteristics according to case studies (Kemball-Cook and Wang 2001) and *Hovmöller* diagrams at different latitudes.

The northward propagating ISO in the Asian-Pacific summer monsoon region is normally restricted to the latitudinal domain from the equator to 25°N. The equatorial region and the off-equatorial region often possess opposite active/break phase, which compromises the ascending/descending branch of a transient meridional circulation. Such meridional dipole pattern is primarily described by the meridionally propagating wavenumber-1 mode in the wavenumber-frequency analysis. Therefore, the spatial decomposition domain is chosen as 5°S-25°N.

3.3 Other supporting analysis methods

The intraseasonal component y_{iso} is defined as the sum of Fourier components with period longer than 10 days and shorter than 90 days. In order to extract y_{iso}, the sum of the annual mean and the first four harmonics (y_{ac}) are removed from each year's time series. The interannual variation of the seasonal mean, which is carried by y_{ac}, is removed. Upon performing such filtering at each grid point, standard deviations are used to represent the amplitude of the ISO. To further separate the stationary anomalies from the propagating anomalies, wavenumber-frequency analysis is performed.

In addition to the wavenumber-frequency analysis, which is applied only in one-dimension, extended EOF analysis (Weare and Nasstrom 1982) has also been applied in this study to reveal the 2-D propagation features.

Two-sample student's t-test is applied to test the significance of composite scenarios for ENSO warm and cold episodes. The null hypothesis for the two-sample t-test is that warm and cold ensembles have identical sample means. Test statistics are constructed following the convention (refer to Wilks 1995, chapter 5). Student's t-test is also used for testing the significance of correlation coefficients.

Chapter 4

Characteristics of the Summertime ISO

4.1 Distinct summertime characteristics

The MJO is most pronounced in the boreal winter (Madden 1986; Wang and Rui 1990). Yasunari (1979, 1980, 1981) first revealed intraseasonal convection and circulation anomalies propagating northward from the equator to the Himalayan region in the boreal summer, which links the active/break phase of the Indian summer monsoon with the MJO. Lau and Chan (1986) further revealed a northwestward propagation of the boreal summer ISO in the WNP. The evolution of the East Asian summer monsoon has a close relationship with the WNP ISO (Lau et al. 1988; Wang and Xu 1997).

The location of the ISO variability centers varies during the annual migration of the ITCZ (Wang and Rui 1990a). In the boreal winter, the ISO is confined to the southern and the equatorial Indian Ocean and the Pacific Ocean (Fig. 4.1b).

The MJO is the predominant mode. Pronounced eastward propagation prevails from the equatorial Indian Ocean to the western Pacific. Although the lag-correlation coefficients reveal northward and northwestward propagation in the Bay of Bengal and the WNP, respectively, the amplitude of the ISO in those regions is too weak to change the prevailing features of the MJO. In the boreal summer, the ISO centers move to the equatorial Indian Ocean, the Bay of Bengal and the WNP (Fig. 4.1a). Large intraseasonal anomalies are found at 10°N in both the Bay of Bengal and the WNP, where the intraseasonal anomalies propagate northward and northwestward, respectively. Meanwhile, the equatorial eastward propagation is evident only from the central to the eastern Indian Ocean.

Within the northern summer, the ISO exhibits pronounced subseasonal change. Early summer is dominated by the northward propagation in the Indian summer monsoon region (Fig. 4.2a). From August to October, the northwestward propagation of the ISO in the WNP becomes the most prevailing feature (Fig. 4.2b). Meanwhile, the ISO in the Indian summer monsoon region weakens. This phenomenon has been studied by Kemball-Cook and Wang (2001) by composite analysis. LinHo and Wang (2002) argued that the subseasonal change in the ISO is caused by evolution of the Asian-Pacific monsoon. In early summer, the heating center is located in the Indian summer monsoon sector, whereas in the late summer, the WNP plays a leading role.

The frequency of the MJO does not change significantly from the winter to the summer (Madden 1986). Figure 4.3 shows the wavenumber-frequency spectrum at

the equator in May-Oct and Nov-Apr. In both seasons, the dominant period is about 50 days, although the wintertime frequency peak possesses higher energy.

The westward propagating ISO has a broader spectrum at 15°N than the eastward propagating MJO (Fig. 4.4). In the summer, 20-25-day and 10-day oscillations are also evident. Higher-frequency variability is associated with a smaller spatial scale.

The meridional propagation and the higher frequencies are possibly resulted from interaction of the equatorial wave with the monsoon mean flow (Lau and Peng 1987; Wang and Xie 1996a,b). Although the MJO is weaker in the boreal summer, its basic characteristics are invariant with respect to season, because it is an intrinsic equatorial dynamic mode (Lau and Chan 1986) and Kelvin wave is not sensitive to change in the mean flow (Wang and Xie 1996 a,b).

Previous composite analyses have revealed that the MJO has a coherent dynamic structure in both circulation and convection (Rui and Wang 1990; Knutson and Weickmann 1987). At the upper/lower troposphere, two anticyclonic/cyclonic systems reside north and south of the equatorial convective anomaly, respectively. Easterlies between the two upper-level anticyclones and westerlies between the two lower-level cyclones are coupled with the equatorial convection. Yet these studies do not distinguish the seasonal variations in the coupled structure.

The horizontal and vertical structures of the MJO vary with season in a global perspective, which is revealed by the dominant multi-variable extended EOF (EEOF)

modes using CMAP and the zonal winds at 850, 200 hPa. Since the first two EEOF modes are closely related to each other, and they show similar progression except a phase shift, only the first EEOF mode is shown for brevity.

In the boreal winter (Fig. 4.5, Fig. 4.6), negative/positive CMAP anomalies consistently propagate eastward from pentad t-4 to pentad t+4. Both circulation and convection anomalies at pentad t+4 seem to be followed by those at pentad t-4, suggesting a repeating cycle with a period of 50 days. The convection field is represented by a dipole pattern with the Indian Ocean and the Pacific having an opposite sign in the CMAP anomalies (Zhu and Wang 1991). The amplitude of the CMAP anomaly reaches the maximum amplitude at pentad t0. Thereafter, the convective anomalies stalk and decay at 150°W.

The easterly/westerly anomalies of the 850 hPa wind coincide with the negative/positive CMAP anomalies at most of the phases. The wind anomalies to the east of 150°W are negligible at 850 hPa. The 200 hPa wind anomalies have a larger spatial scale (Fig. 4.6) They are not strictly confined to the region where the convective anomalies are found. There are two variability centers: one over the Indian Ocean and Africa, and the other in the west coast of South America. Positive/negative anomalies in the western Pacific are associated with a pair of easterly/westerly anomalies residing at the southwest and northwest of the convective center. Meanwhile, there are westerly/easterly anomalies ahead of the convective anomaly. It is a typical Gill-type response: Kelvin wave response is located ahead of the convective anomaly, and

Rossby wave response is lagged behind.

In the boreal summer (Fig. 4.7), the dominant EEOF mode suggests that the convection anomalies move northeastward from the Indian Ocean to the WNP. Besides, the spatial scale of the convective anomalies is smaller. Most of the anomalies are confined to 50°E-180°E. Some weak signals are found in the ITCZ in the eastern Pacific. The feature only exists in the summer.

The 850 hPa zonal wind anomalies have a longer wave length in the summer. Besides in the eastern hemisphere, large intraseasonal variability is also found in the eastern Pacific. In the eastern hemisphere, the 850hPa easterly/westerly wind anomalies centers are located to the southwest of the negative/positive convective anomalies during their northeastward migration. After the negative/positive convective anomalies move to the western Pacific at pentad t-4/t0, westerly/easterly 850 hPa wind anomalies prevail in the eastern Pacific, and continue to grow until the convective anomalies start decaying at pentad t-1 and t+3.

The 200 hPa zonal wind patterns (Fig. 4.8) also differ from those in the winter. Most variability is found in the eastern Pacific. Although the Asian-Pacific summer monsoon region has the most pronounced intraseasonal convective anomalies, the local 200 hPa zonal wind anomalies are much weaker in both amplitude and spatial size compared with those in the eastern Pacific. A pair of Rossby response located at both sides of the equator can not be found in the summer.

As a summary, the boreal summer ISO differs from the wintertime ISO in

the following aspects: The summertime ISO has large meridional components, which include the northward propagating mode in the Indian summer monsoon region and the northwestward propagating mode in the WNP. They coexist with the MJO. The summertime ISO in the off-equatorial region has smaller spatial scales and high-frequencies. The horizontal and vertical structure of MJO varies with season. Due to the pronounced seasonality, the summertime and wintertime ISOs should be separated in order to investigate their interannual variations.

4.2 The interannual variations

The overall intensity of the summertime ISO is measured by standard deviation of May-October intraseasonal anomalies. This intensity varies from year to year. Figure 4.9a displays the 23-year (1979-2001) mean ISO intensity in CMAP. The largest amplitude of the ISO is located along 15°N over the Philippine Sea, the South China Sea, the Bay of Bengal and the eastern Arabian Sea. Other active center is found in the South Indian Ocean at about 5°-10°S. The results derived from the 850 hPa wind are consistent in the tropical region (figure not shown). Besides the 850 hPa wind also shows large intraseasonal variability at higher latitudes.

The variability center of the summertime ISO is located away from the equatorial region where the most pronounced year-to-year variation in the summer mean state is found. Figure 4.9b shows the standard deviation of May-October mean CMAP that represents the interannual variation of the summer mean state. The most signifi-

cant interannual variation of seasonal mean state is located at the equatorial western-central Pacific which is induced by ENSO. The second maximum is located at 5°S, west of Sumatra. It is noted that the variation of the ISO favors the off-equatorial region while the interannual variations of the summer mean state favor the equatorial region.

The most pronounced interannual variation of the summertime ISO intensity is located in the WNP. Figure 4.10 shows the interannual standard deviations of the 23-year ISO intensity in CMAP and 44-year ISO intensities in 850 hPa zonal and meridional winds (also refer to as u850, v850). Although climatologically the Bay of Bengal is the most active center for the summertime ISO, its interannual variation is substantially weaker than in the WNP. The longitude domains of the year-to-year variability centers are similar in the three variables, but the latitudes slightly differ. The CMAP centers along 15°-20°N while the elongated band of u850 variability is centered at about 10°N. This latitudinal phase shift between convection and zonal wind is consistent with the positive correlation between an enhanced convection and associated enhanced westerly to the south and southwest of the convection shown by Wang and Fan (1999) who interpret this relation as resulting from the interaction between convective heating and Rossby wave response. The v850 ISO interannual variability center exhibits a northwestward tilt from about 160°E at the equator to the East China Sea. It indicates that the meridional wind anomalies associated with anomalous cyclone/anticyclone prevail along this tilted path.

The interannual variation in the ISO intensity is linked to ENSO. Linear correlation coefficients between the ISO intensity at each grid and the May-October seasonal mean Nino3.4 SST anomalies are presented in Fig. 4.11 . To detect decadal variability embedded in the 44-year ISO intensities in u850 and v850, correlation in the following two periods are calculated: 1958-2001 (Fig. 3b,c) and 1979-2001 (figure not shown). For both cases, positive correlations dominate in the WNP. The positive area tilts from southeast towards northwest. The axis of the maximum positive correlation coincides with the WNP monsoon trough. Significant negative correlations are seen in the western Bay of Bengal between 10°-20°N. The negative correlations, however, become insignificant for the latter 1979-2001 period. Significant positive correlations are also found in the WNP in CMAP rainfall data, with the maximums between the equator and 10°N (Fig. 4.11a). There is a small positive-correlation area in equatorial central Indian Ocean and a negative-correlation area in the eastern Arabian Sea at 10°N. The correlation coefficients in the rest of Indian monsoon region are insignificant. The ISO intensity shows the most significant correlation with Nino3.4 SST in the western and central Pacific.

Thus, both convection and lower tropospheric circulation show pronounced interannual variation in the ISO intensity in the WNP, which is closely linked with ENSO. But whether and how ENSO affects the ISO in the Indian monsoon region remain to be explored.

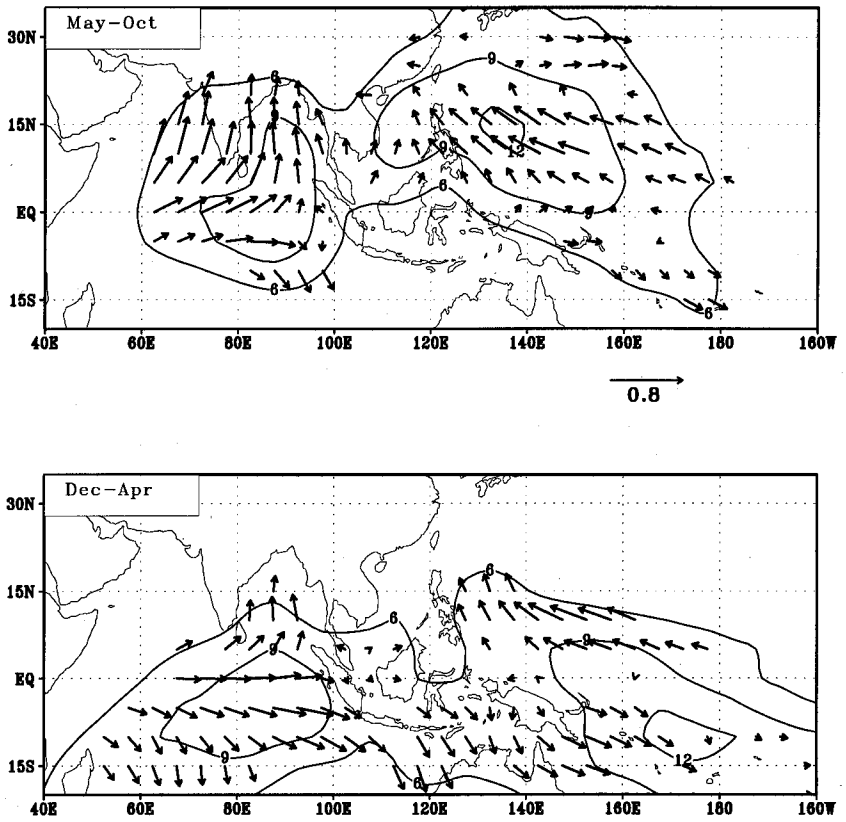

Figure 4.1: Standard deviation of 20-70 day CMAP (Xie and Arkin 1996) in (a) May-October and (b) November-December averaged for the period of 1979-2001. It denotes the intensity of the intraseasonal variability. Contour levels are 6, 9, 12 mm/day. The length of the vector is the maximum one-pentad lag correlation coefficient between a given grid and its surrounding grid points. The direction indicates the propagation tendency of the ISO. Only those vectors that are significant at the 95% confidence level (correlation coefficients of ± 0.14 (Lau and Chan 1986)) within the 6 mm/day contour are plotted.

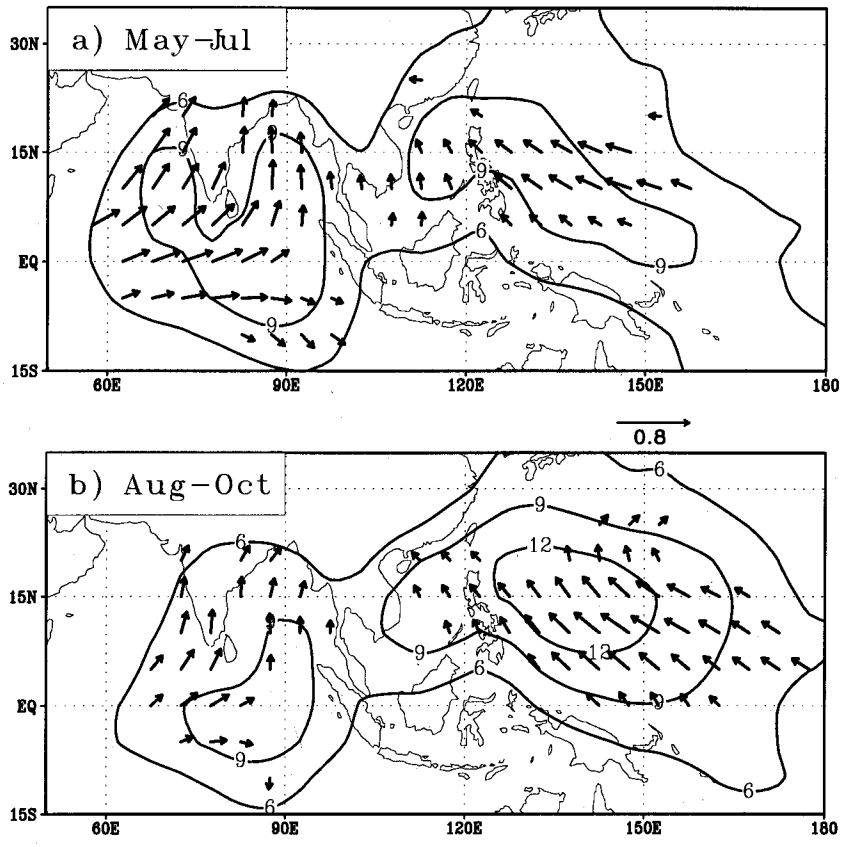

Figure 4.2: Same as Fig. 4.1 but for (a) May-Jul and (b) Aug-Oct.

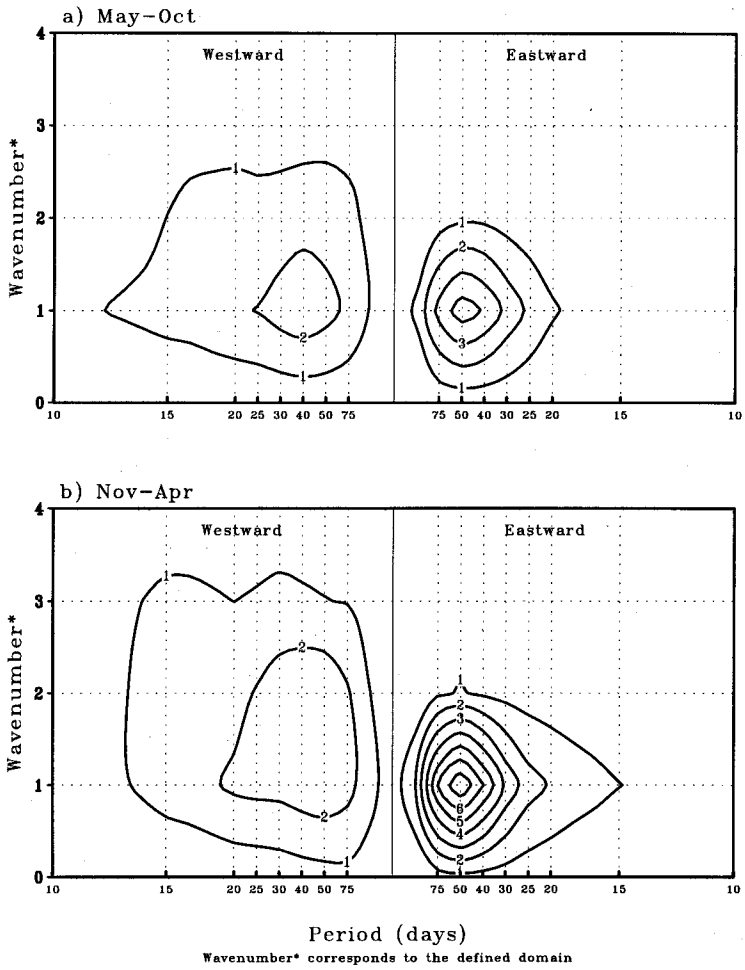

Figure 4.3: 1979-2001 averaged wavenumber-frequency spectrum for OLR at the equator in (a) May-Oct and (b) Nov-Apr. The longitude domain is 40°E-120°W.

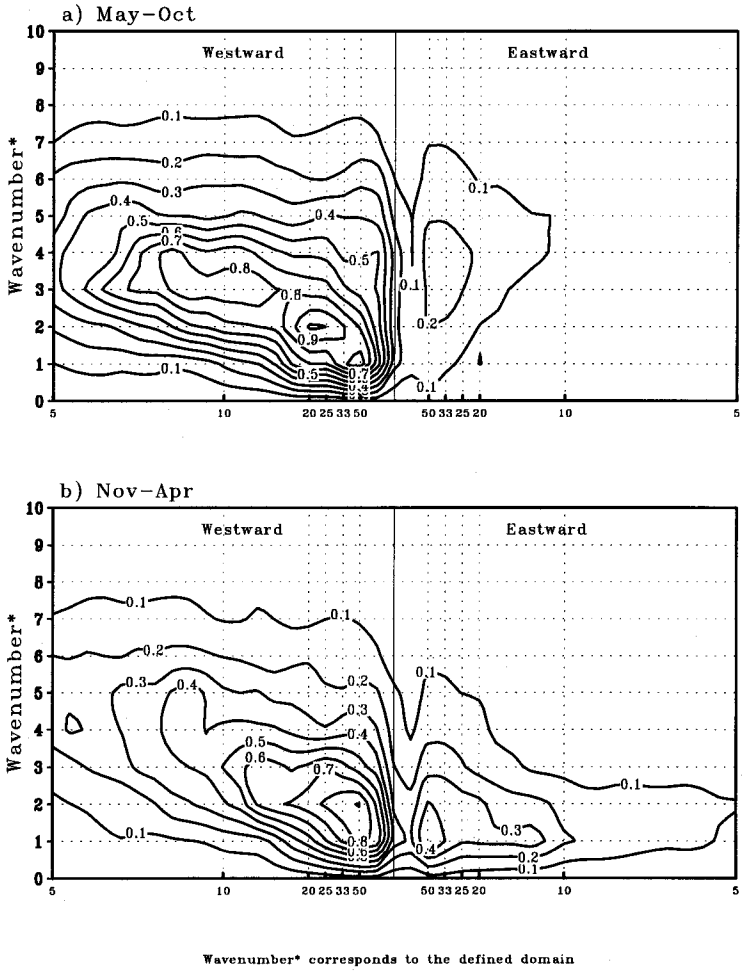

Figure 4.4: Same as Fig. 4.3 but for sepctrum at 15°N.

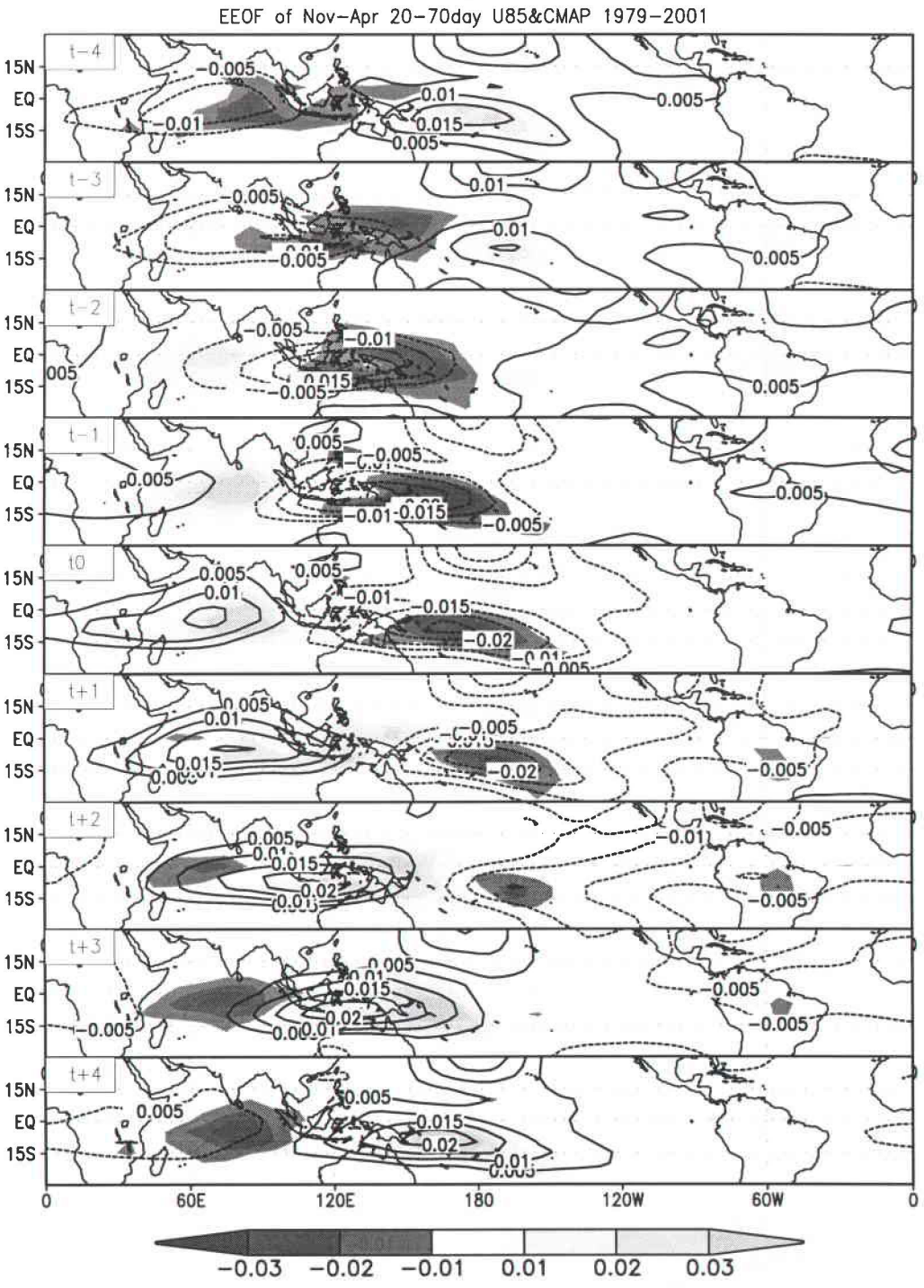

Figure 4.5: First EEOF mode of 20-70-day CMAP (shading) and 850 hPa zonal wind (contour) at from $t-4$ pentad to $t+4$ pentad in November-April, 1979-2001.

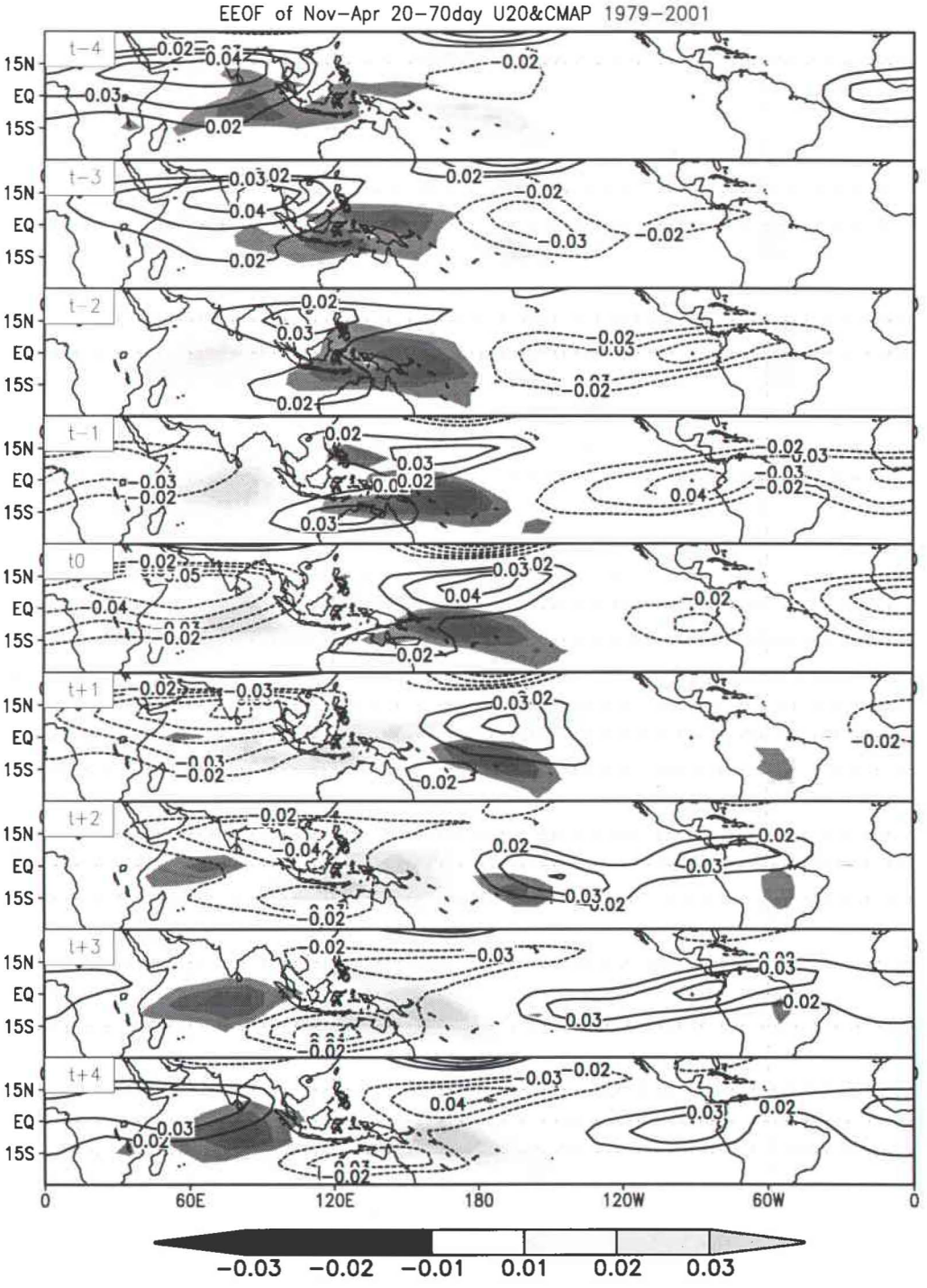

Figure 4.6: Same as Fig. 4.5 but for CMAP and 200 hPa zonal wind.

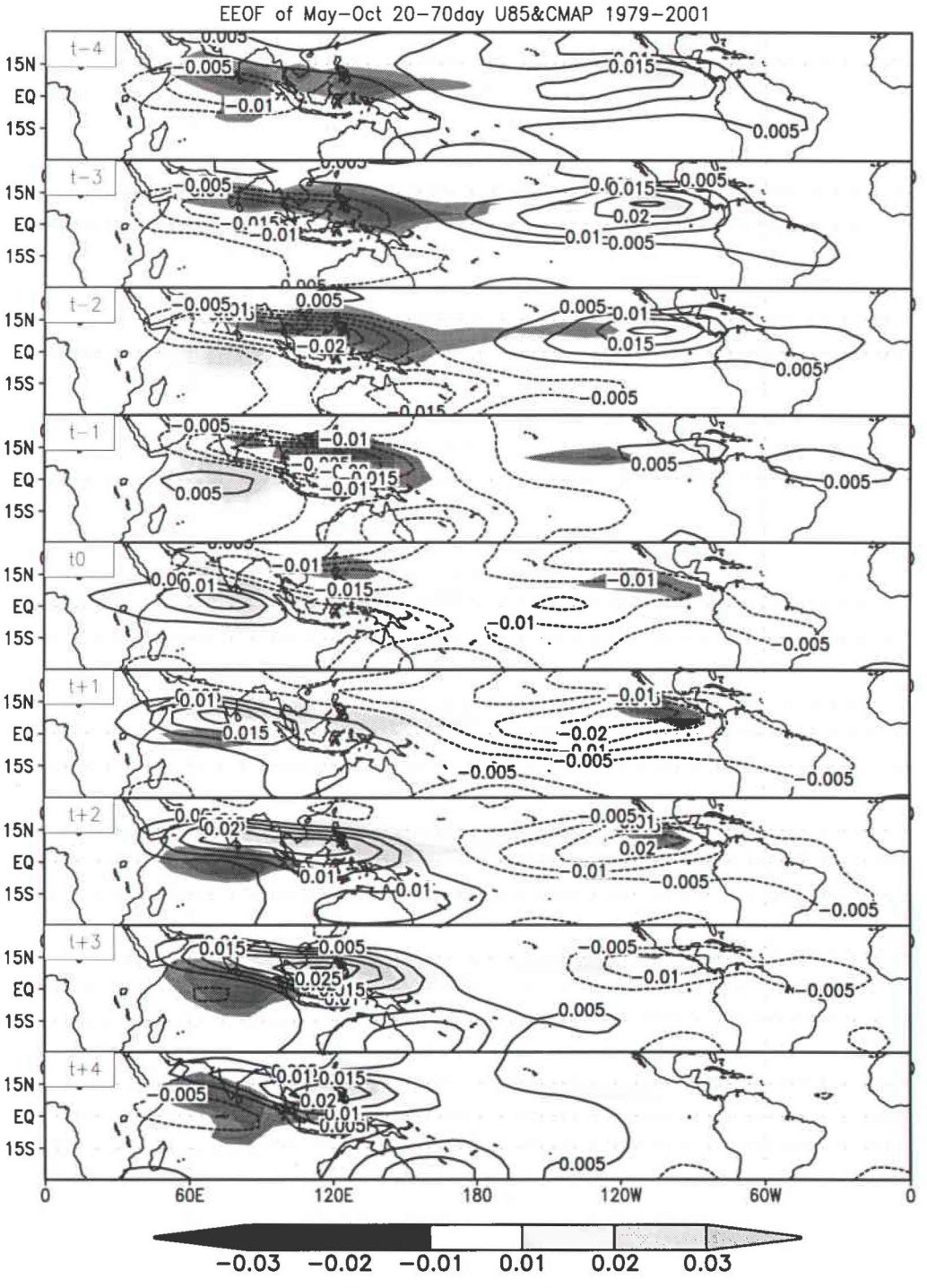

Figure 4.7: Same as Fig. 4.5 but for May-October.

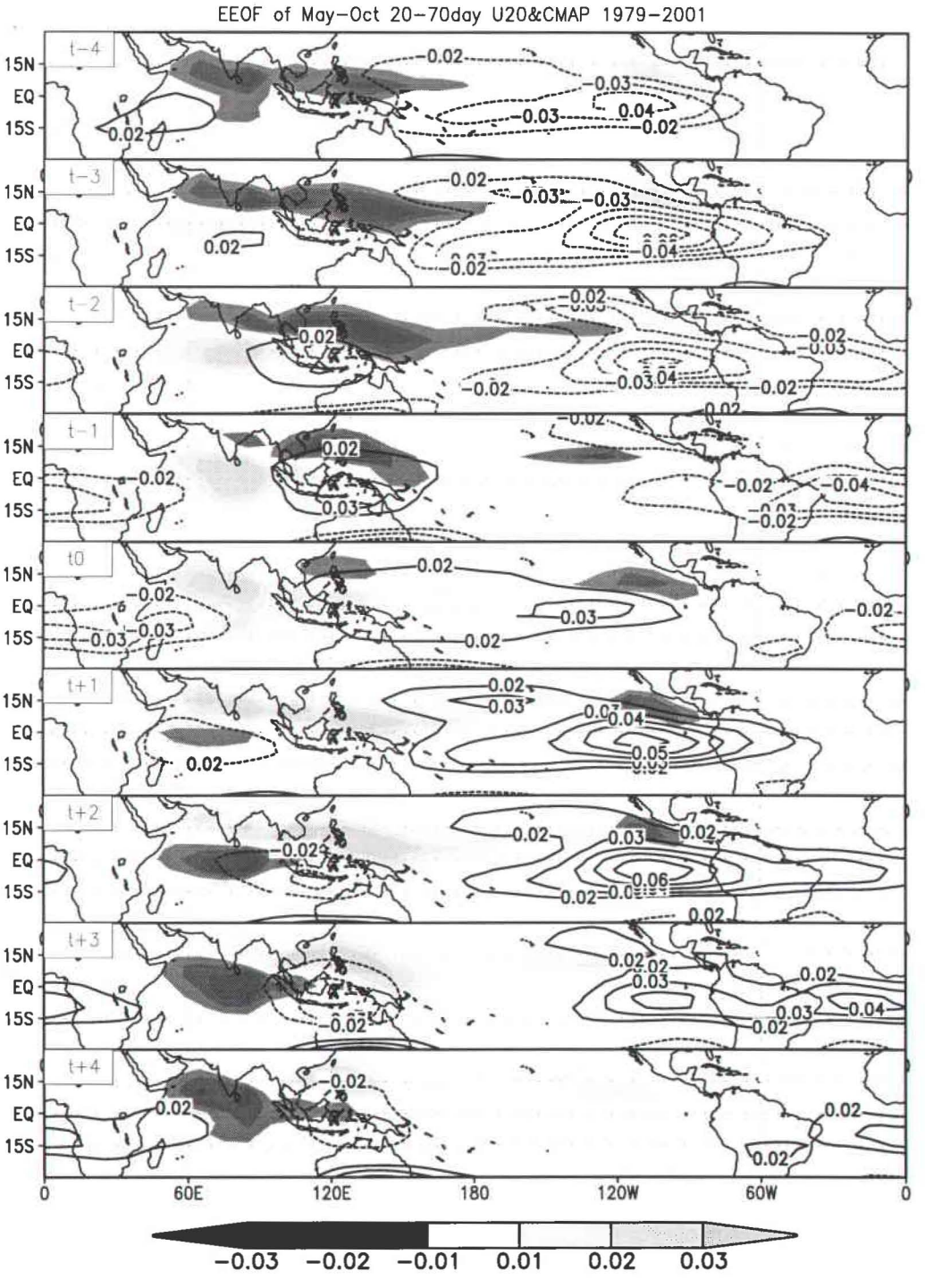

Figure 4.8: Same as Fig. 4.6 but for May-October.

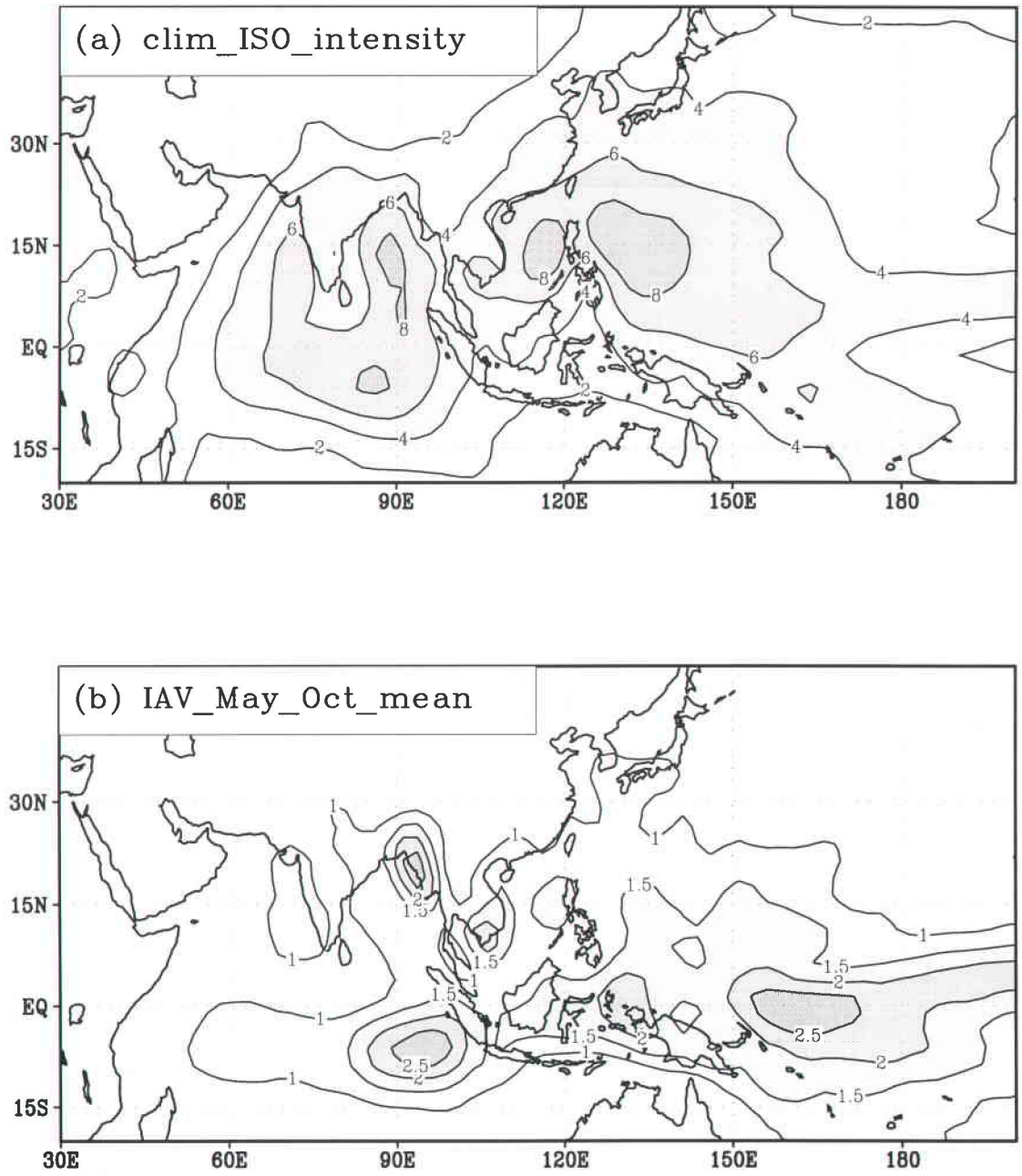

Figure 4.9: (a) 1979-2001 averaged boreal summer ISO intensity and (b) the 23-year standard deviation of May-Oct seasonal mean in CMAP. Both units are (mm/day).

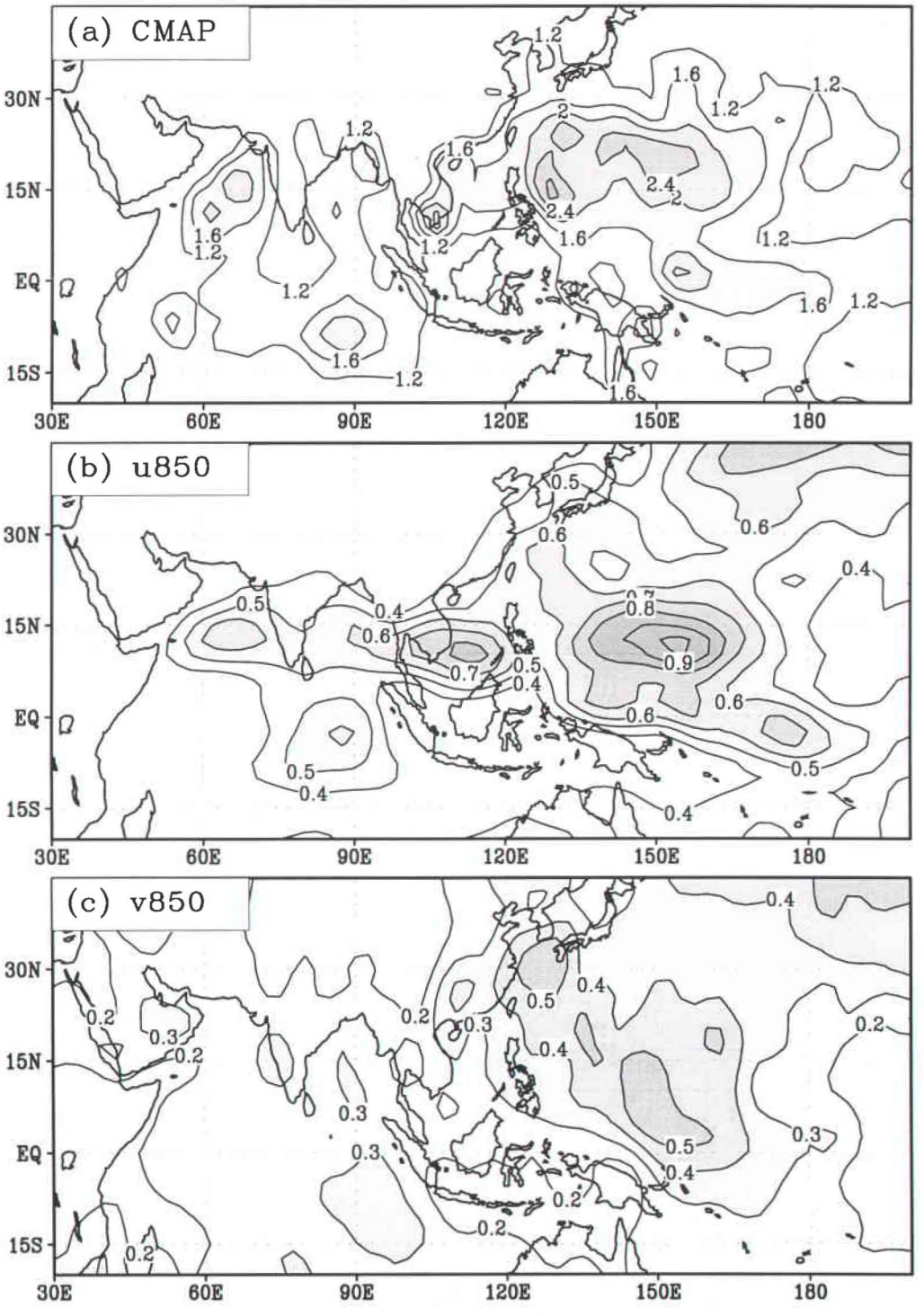

Figure 4.10: 1979-2001 interannual standard deviations of the boreal summer ISO intensities using (a) CMAP, (b) 850 hPa zonal wind and (c) 850 hPa meridional wind. The unit is mm/day, m/s and m/s for (a), (b) and (c), respectively.

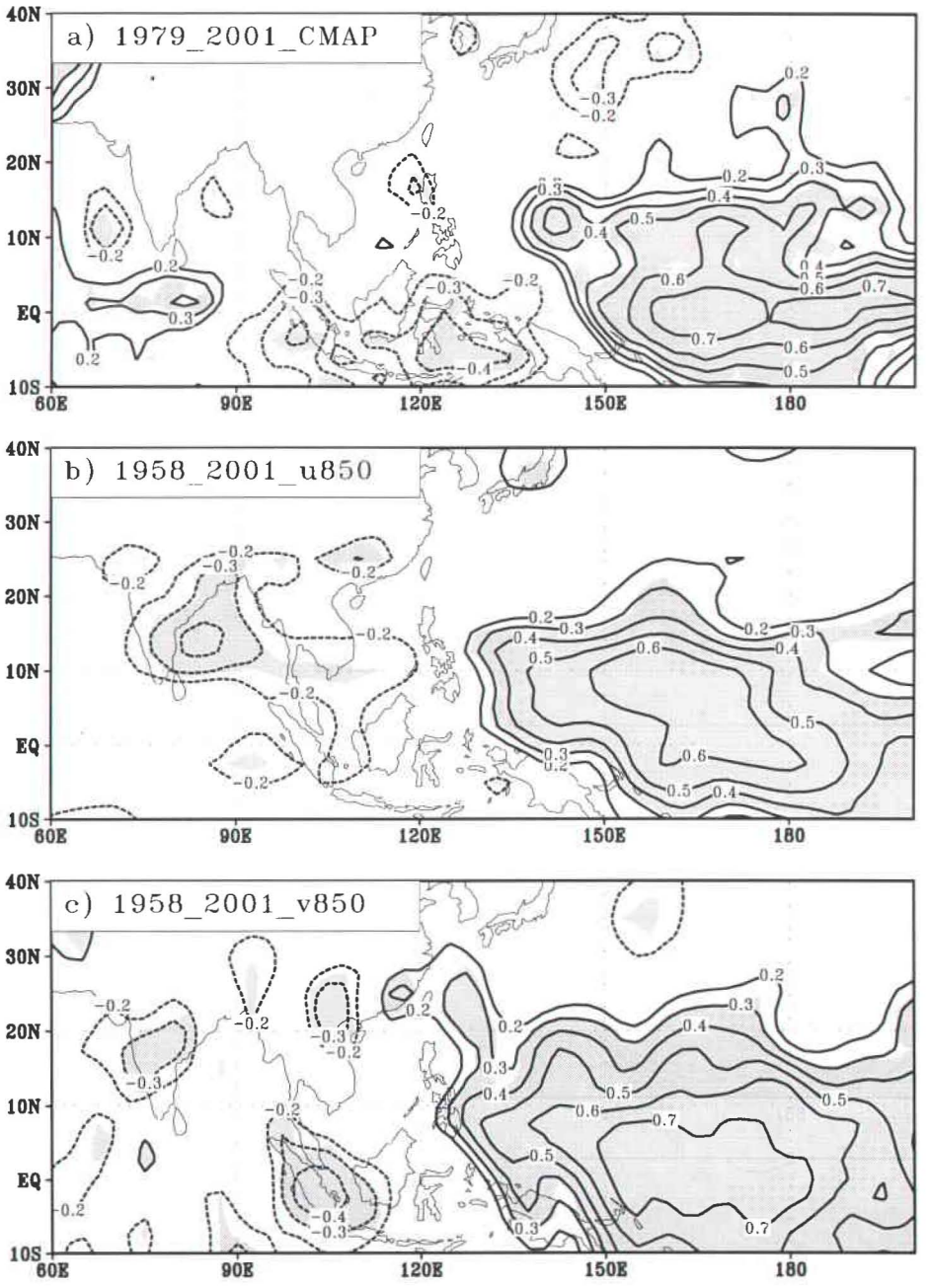

Figure 4.11: Linear correlation coefficients between May-Oct Niño3.4 SST anomaly and the summer ISO intensities in (a) CMAP during 1979-2001, (b) 850 hPa zonal and (c) meridional winds during 1958-2001. Shading indicates the 95% confidence level. Contours with values between -0.2 and 0.2 are omitted.

Chapter 5

The Madden-Julian Oscillation

5.1 Seasonal-dependence of the MJO's interannual variability

The previous chapter has shown that the MJO is more active in the boreal winter and spring. During the boreal summer, not only the amplitude of MJO weakens, the horizontal and vertical structures also change in a global perspective.

Significant seasonality also exists in the MJO's interannual variations. For example, Slingo et al. (1999) developed a continuous multi-year daily index to measure the MJO's interannual variations. Following their definition, the index is presented in Fig. 5.1. Besides large interannual variability, it contains pronounced seasonal variability as well. The amplitude of the seasonal variability is sometimes larger than the interannual variability, which gives rise to the question: Does the MJOs in the

boreal winter and summer have coherent interannual variations? This question has not been paid much attention in the previous studies.

To reveal the seasonal change of the MJO, wavenumber-frequency analysis is carried out in four seasons: January-March, April-June, July-September and October-December. The longitude domain of the analysis varies from winter to summer. It is specified according to the ISO intensity in the four seasons (Fig. 5.2). The domain spans from 50°E to 140°W in Jan-Mar and Oct-Dec, and from 50°E to 180°E in Apr-Jun and Jul-Sept.

The MJO is dominated by a wavenumber-1 component. Its spectrum density as a function of latitude is shown in Fig. 5.3. The MJO is most pronounced between the equator and 20°S in Jan-Mar. Meanwhile, there are two centers associated with the westward propagation. They are Rossby-wave responses located to the west of the convection center: the northern one at about 5°N and the southern one at about 10°S. The spectrum density weakens by half in Apr-Jun when the center of the MJO is located right on the equator. In Jul-Sept, the MJO continues to weaken. The variability center splits into two: One at the equator and the other one at about 10°N. Meanwhile, some 20-30-day westward propagating anomalies grow at 10°N. The westward propagating modes have higher spectrum density and higher wavenumbers (Figure not shown). In Oct-Dec, the MJO center retreats to the equator. But the intensity is weaker than in Apr-Jun.

In order to measure the strength of the MJO, a MJO index is defined as the

averaged spectrum density of the 20-70-day eastward propagating OLR anomalies between 10°S and 10°N. Figure. 5.3 has shown that the MJO centers at between 10°S and 10°N in Apr-Jun, Jul-Sept and Oct-Dec. In Jan-Mar, the eastward propagation center is located at 20°S-5°N. Because the results are similar if the domain is switched from 20°S-5°N to 10°S-10°N, an uniform latitude domain of 10°S and 10°N is used for the definition of the MJO index in the four seasons.

The MJO in the four seasons exhibits different interannual variations. The indices for the period of 1979-2001 are shown in Fig. 5.4. The 23-year correlation coefficients between the MJO indices in different seasons are listed in Table 5.1. Only the Jun-Sept and Oct-Dec indices show a significant correlation coefficient.

Table 5.1 Correlation coefficients between the MJO indices in Jan-Mar, Apr-Jun, Jul-Sept, and Oct-Dec. The 95% confidence level for n=23 is 0.44.

	Jan-Mar	Apr-Jun	Jul-Sept	Oct-Dec
Jan-Mar		0.28	-0.23	-0.18
Apr-Jun			-0.02	0.24
Jul-Sept				0.61

The MJO-ENSO relationship is seasonally dependent. The Nino3.4 SST index is compared with the MJO index in the four seasons in Fig. 5.4. The MJO has significant positive correlation with the Nino3.4 SST index in Apr-Jun and Oct-Dec, which are two transitional seasons. The MJO-ENSO relationship is not significant in Jul-Sept and Jan-Mar. The correlation coefficient is most insignificant in Jan-Mar.

The total variance at each grid point is contributed by both propagating (eastward and westward) and stationary anomalies. A large portion of the total variance

is associated with the MJO in Jan-Mar. Figure 5.5 shows the correlation coefficients between the MJO index and the total 20-70-day standard deviation during 1979-2001. Significant positive correlation coefficients are found from the Indian Ocean to the western Pacific in Jan-Mar. Yet the area with significant correlation coefficients decreases. In Jul-Sept, the MJO index is mainly significantly correlated with the total variance in the central Indian Ocean and the far western Pacific. By the time of Oct-Dec, the relationship between the total variance and the MJO index reaches the weakest. It implies that the standing anomalies contribute to a large portion of the total intraseasonal variability in Oct-Dec. Thus, the total variance at each grid point can not represent the overall intensity of the MJO.

The MJO in Apr-Jun and Oct-Dec has a significant linkage with ENSO, which is in a sharp contrast with the MJO in Jan-Mar and Jul-Sept. The linkage also breaks conclusions from the previous studies that the overall activity of the MJO is not related to ENSO. Those studies either only focused on the general winter season or failed to measure the wave propagation. It is interesting that a strong linkage between the MJO and ENSO occurs in the two transitional seasons when the MJO variability centers are located at the equator.

5.2 The interannual variations of the early-summer MJO

The previous studies have described that the ISO changes its behavior from the early summer to the late summer (Kemball-Cook and Wang 2001; LinHo and Wang 2001). In the early summer, the MJO and the northward propagating ISO in the Indian Ocean are the dominant ISO modes. In the late summer, the northwestward propagating ISO prevails in the WNP. Meanwhile, the equatorial eastward propagating MJO reaches the weakest phase during the entire year. The spatial domain of the traveling convective anomalies is usually confined to the central-eastern Indian Ocean. This section mainly focuses on the early summer MJO.

Following a similar analysis routine, wavenumber-frequency analyses were carried out at the longitudinal domain of 40°E-180° in the equatorial region using 1958-2001 500 hPa vertical velocity (hereafter referred to as ω_{500}) and 1979-2001 OLR. The MJO index is defined as the averaged spectrum density of 20-50-day wavenumber-1 anomalies at 40°E -180°E, 2.5°S-5°N for ω_{500} and 5°S-10°N for the OLR. These domains are the variability centers of the eastward propagating intraseasonal OLR and ω_{500} anomalies (figure not shown).

Both the OLR and the ω_{500} indices have a close connection with the Nino3.4 SST anomaly (Fig. 5.6). The correlation coefficients between the MJO indices (using OLR and ω_{500}) and the Nino3.4 SST during 1979-2001 are listed in Table 5.2. It

suggests that the MJO is enhanced in May-Jul at the developing stage of *El Niño* . The result is not sensitive to small adjustments in the domain. The correlation remains significant when the domain is enlarged to 40°E-220°E, 10°S-10°N for OLR. Based on the OLR index, the *Hovmöller* diagrams are compared between the strong MJO summers with the weak ones (Fig. 5.7). The strong MJO summers not only have more pronounced intraseasonal anomalies over both oceans, the eastward propagation is also better organized.

Table 5.2 Correlation coefficients between the May-Jul MJO indices using ω_{500}, OLR and the Nino3.4 SST anomaly during 1979-2001. All three correlation coefficients are significant at the 95% confidence level.

	ω_{500} MJO index	OLR MJO index	Nino3.4 SST
ω_{500} MJO index		0.73	0.77
OLR MJO index			0.72

5.2.1 Relationship with the seasonal mean state

Figure 5.8a shows the correlation between the MJO index and May-Jul mean precipitation. When there is a stronger MJO in May-Jul, the mean precipitation in the central-eastern Pacific is enhanced. The Maritime Continent has less rainfall. Meanwhile, the eastern African coast also receives more rainfall. This distribution is similar as the *El Niño* -induced rainfall anomaly. The total intraseasonal variance, which includes the propagating and standing anomalies (Fig. 5.8b) is enhanced in both the Indian Ocean and the western-central Pacific. Although the mean state in the Maritime Continent is suppressed, the intraseasonal activity does not decrease.

The enhanced May-Jul MJO is not correlated with the local SST in the Indian

Ocean. Correlation coefficients were calculated between the OLR MJO index and May-Jul mean SST from the NCEP/NCAR Reanalysis during 1979-2001 (Fig. 5.9). There are small areas of positive correlations in the North Arabian Sea and at 15°S east of Madagascar. No significant correlation is found in the equatorial Indian Ocean. Meanwhile, negative/(positive) correlation dominates the Maritime Continent/(the Pacific east of 160°E). These patterns are similar to the distribution of the ENSO-induced SST anomaly. The correlation further confirms that ENSO affects the May-Jul MJO. The Indian Ocean SST, however, does not directly influence the strength of the MJO.

5.2.2 Comparison with Slingo et al. (1999) index

The currently available MJO indices can generally be categorized into three groups. The most commonly used is the EOF-based index (Kessler 2001; Hendon et al. 1999). The interannual variations can be revealed from the temporal evolution of the dominant EOF mode. It has been criticized because it cannot detect changes associated with spatial pattern. It also cannot identify propagating waves; The second type is proposed by Slingo et al. (1999), defined as the intraseasonal (20-100-day) variance of the global mean using 200 hPa zonal wind between 10°S and 10°N. The third type is derived from wavenumber-frequency spectral analysis, including Salby and Hendon (1994), Hendon et al. (1999) and the present study.

The present method uses more advanced statistics to detect propagating waves

from standing waves than Salby and Hendon (1994) and Hendon et al. (1999). It also focuses on a regional domain in order to measure the MJO more precisely. The results are expected to better represent the strength of the MJO.

The Slingo et al. (1999) index shows pronounced interannual variations of the MJO. Sperber and Slingo (2002) applied this index on seasonal scale. It helped to reveal the vertical structure of the MJO. But the physical meaning of the index remains unexplained. This subsection aims at comparing the present MJO index with the Slingo et al. (1999) index. It's been repeatedly documented that the MJO has a global wavenumber-1 structure in circulation and wavenumber-2 structure in precipitation. But why can the global mean, which is the wavenumber-0 of the zonal wind, be used to describe the MJO activity? The concern is the easterly and westerly wavenumber-1 wind anomalies can cancel each other. In the previous chapter, the EEOF mode shows that the dominant wavenumber of the wind anomaly is between 0 and 1, because the upper-level wind response to the intraseasonal convective anomalies is asymmetric. That's probably the reason that the wavenumber-0 component can be used to measure the MJO.

Such approximation reduces the accuracy of the index. As a example, a comparison of the years of 1987 and 1998 reveals some problems of the Slingo et al. (1999) index. According to the index, the MJO activity is weaker in the summer of 1987 (Fig. 5.10) than in 1998 (Fig. 5.11). Yet the *Hovmöller* diagrams show well-organized intraseasonal anomalies propagating around the globe in the summer of 1987. As a

contrast, the eastward propagation is mostly confined to the western hemisphere in the summer of 1998.

The present wintertime MJO index is highly correlated with the Slingo et al. (1999) index (Fig. 5.12). The correlation coefficient is 0.77 (n=22 winters), significant at the 95% confidence level. Both indices show poor connection with ENSO. But large discrepancies are found in the boreal summer.

In the previous chapter, the 200 hPa wind anomalies associated with the MJO have been compared between the winter and summer. The wintertime anomalies have a spatial scale between wavenumber-1 and -0. The scale is dominated by wavenumber-1 in the summer. Therefore, the Slingo et al. (1999) index, which is based on the wavenumber-0 component cannot represent the summertime MJO.

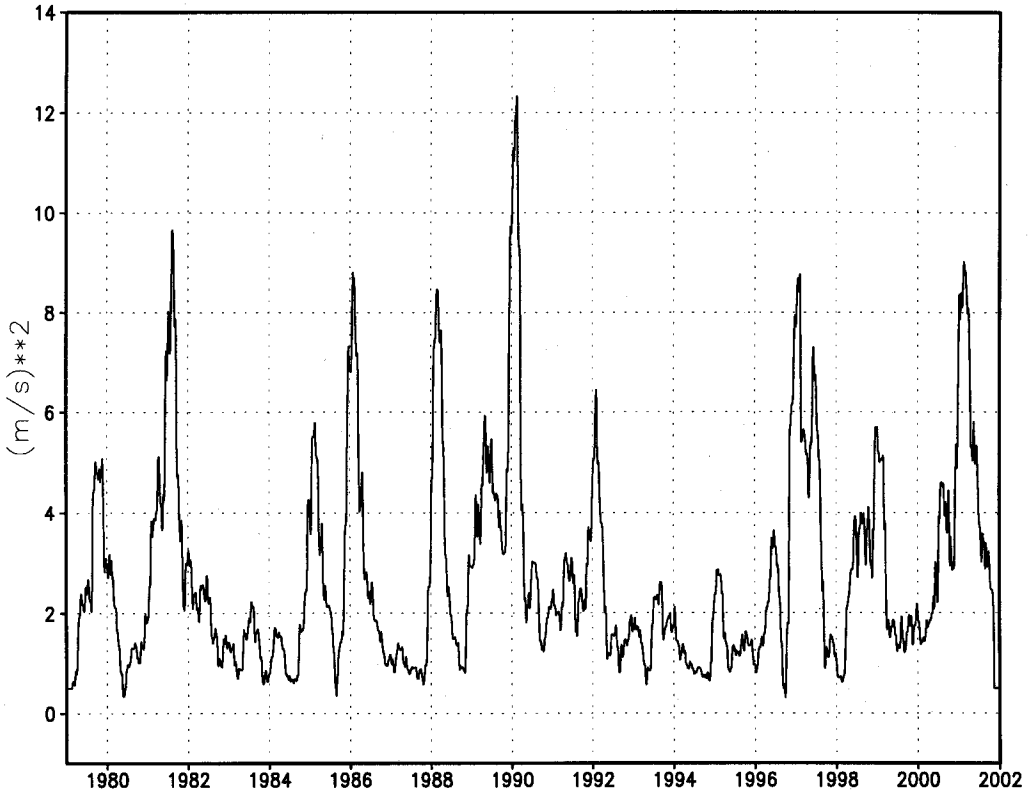

Figure 5.1: The Slingo et al. (1999) MJO index.

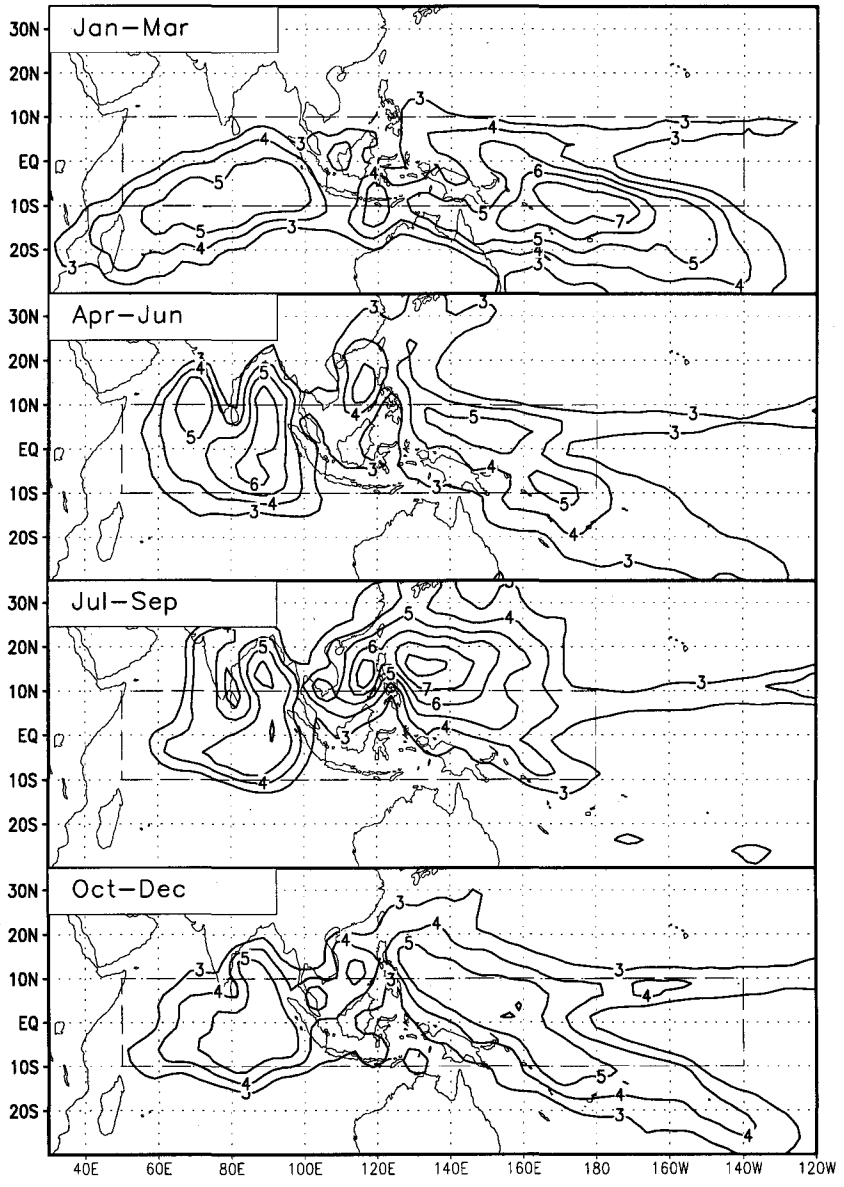

Figure 5.2: 1979-2001 averaged ISO intensity in Jan-Mar, Apr-Jun, Jul-Sept, and Oct-Dec. The ISO intensity is defined as the standard deviation of the 20-70-day CMAP anomalies. The unit is mm/day.

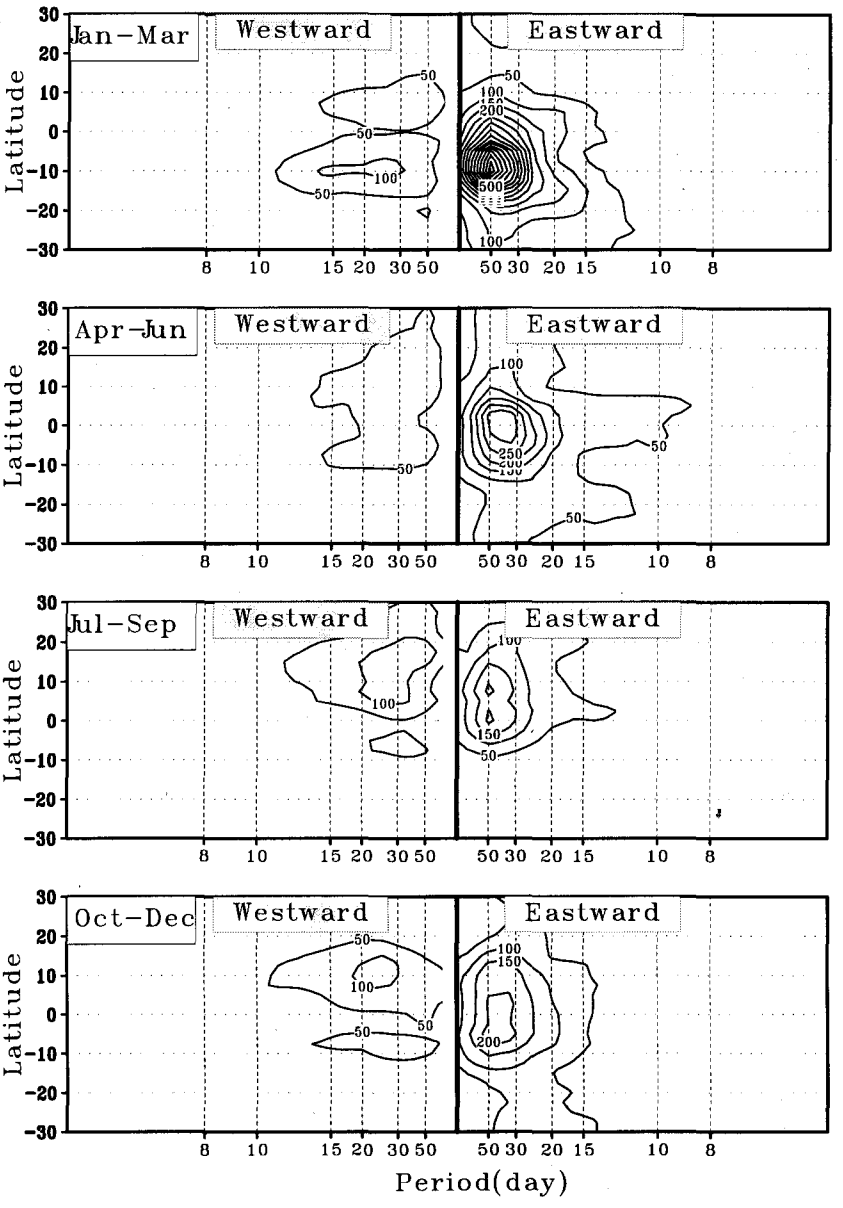

Figure 5.3: 1979-2001 mean spectra as a function of latitude and period for zonally propagating wavenumber-1 OLR anomalies in (a) Jan-Mar, (b) Apr-Jun, (c) Jul-Sept, and (d) Oct-Dec. The longitudinal domain is shown in Fig. 5.2.

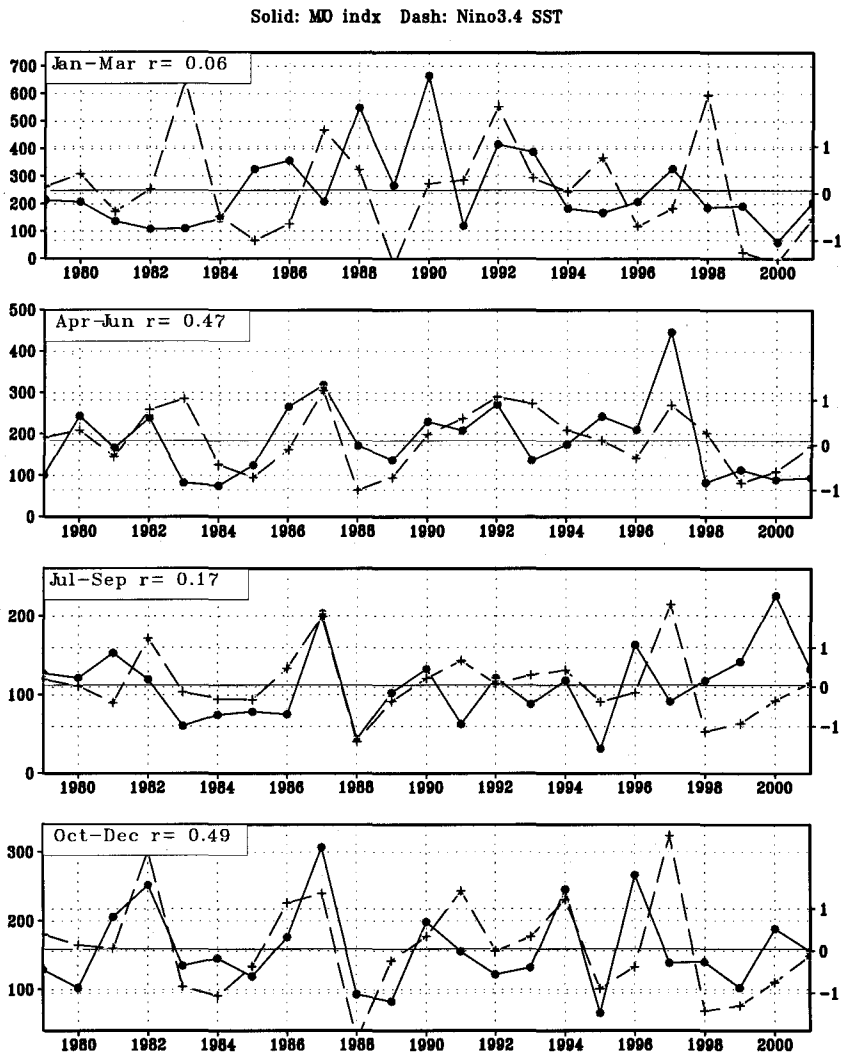

Figure 5.4: 1979-2001 MJO index in the four seasons. The index is defined as the mean spectrum density of the eastward propagating 20-70-day OLR anomalies.

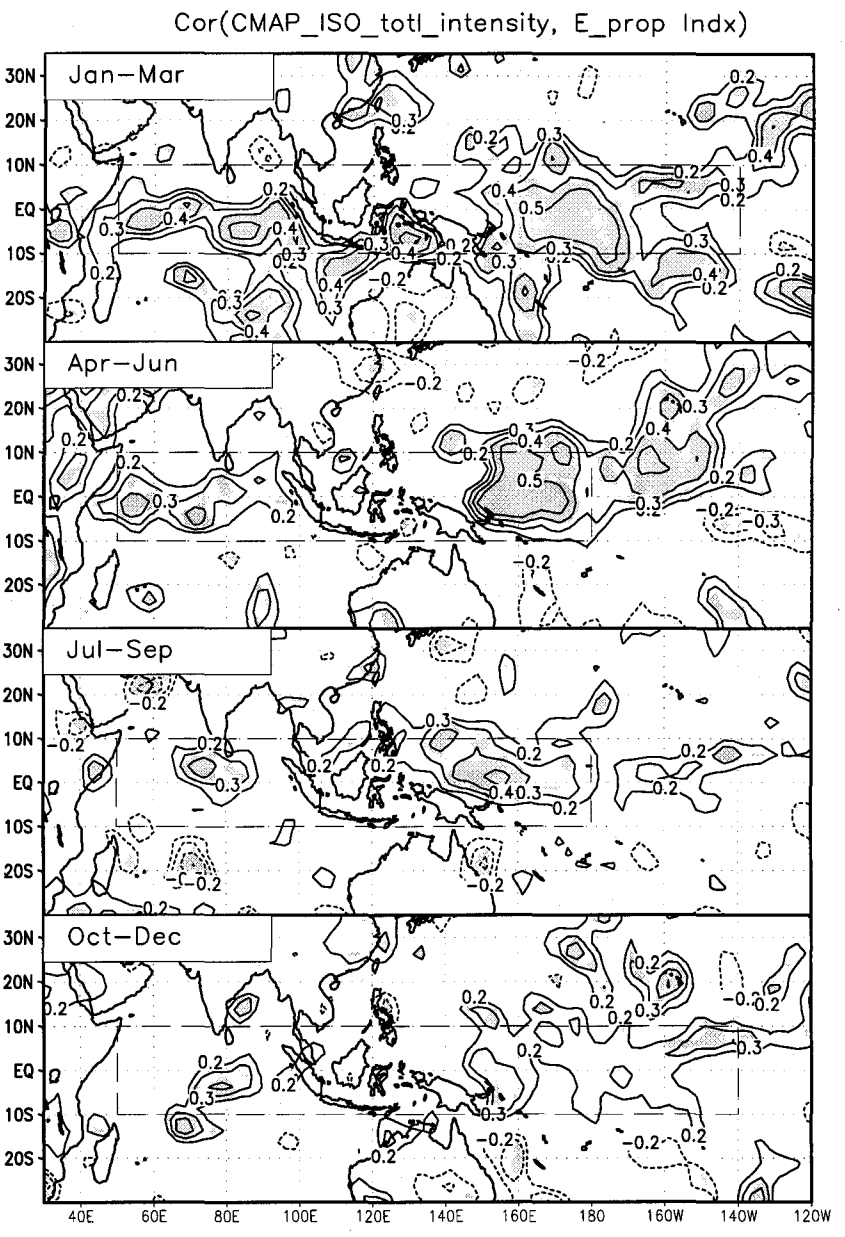

Figure 5.5: Correlation coefficients between the MJO index and the ISO intensity in Fig. 5.2.

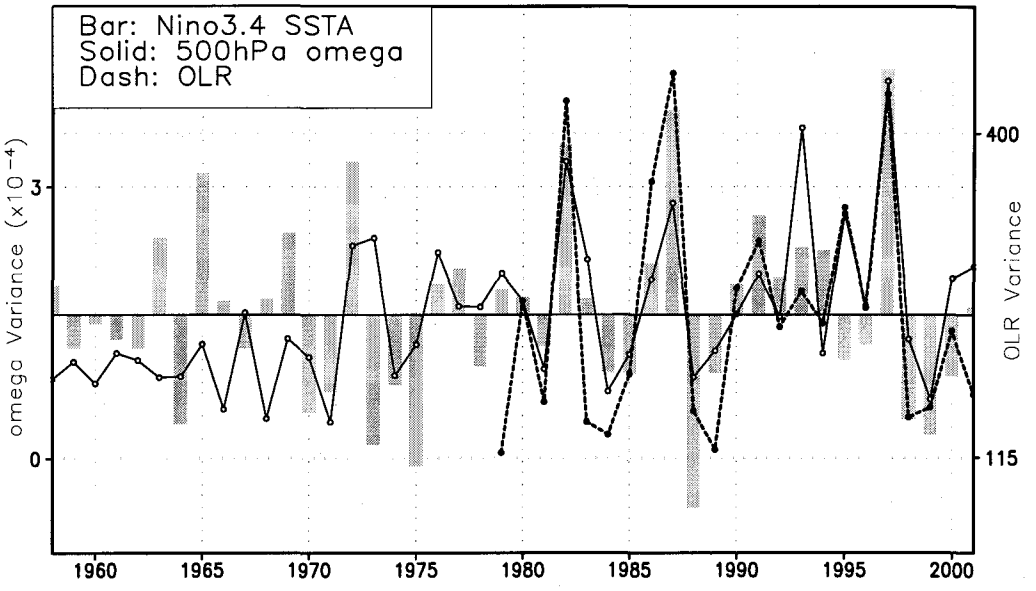

Figure 5.6: May-Jul MJO index in 500 hPa vertical velocity (solid) during 1958-2001, the OLR MJO index (dash) during 1979-2001 and May-Jul mean Niño3.4 SST anomaly (bar) during 1958-2001. The MJO index is defined as the mean spectrum density for 20-50-day eastward propagating wavenumber-1 (at 40°E-180°E) anomalies averaged at 2.5°S-5°N for the vertical velocity and at 5°S-10°N for OLR.

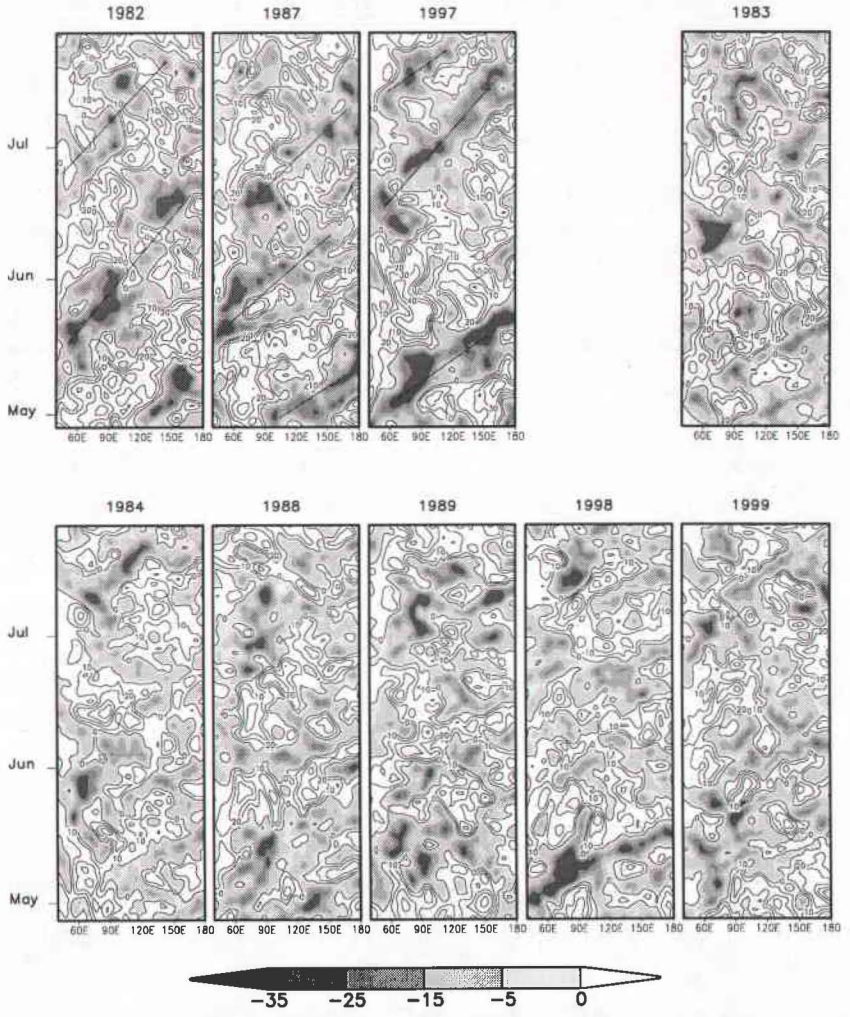

Figure 5.7: The *Hovmöller* diagrams of OLR anomalies averaged at 10°S-10°N in the years of stronger May-Jul MJO (1982, 1987, and 1997) and the weaker MJO (1983, 1984, 1988, 1989, 1998, 1999).

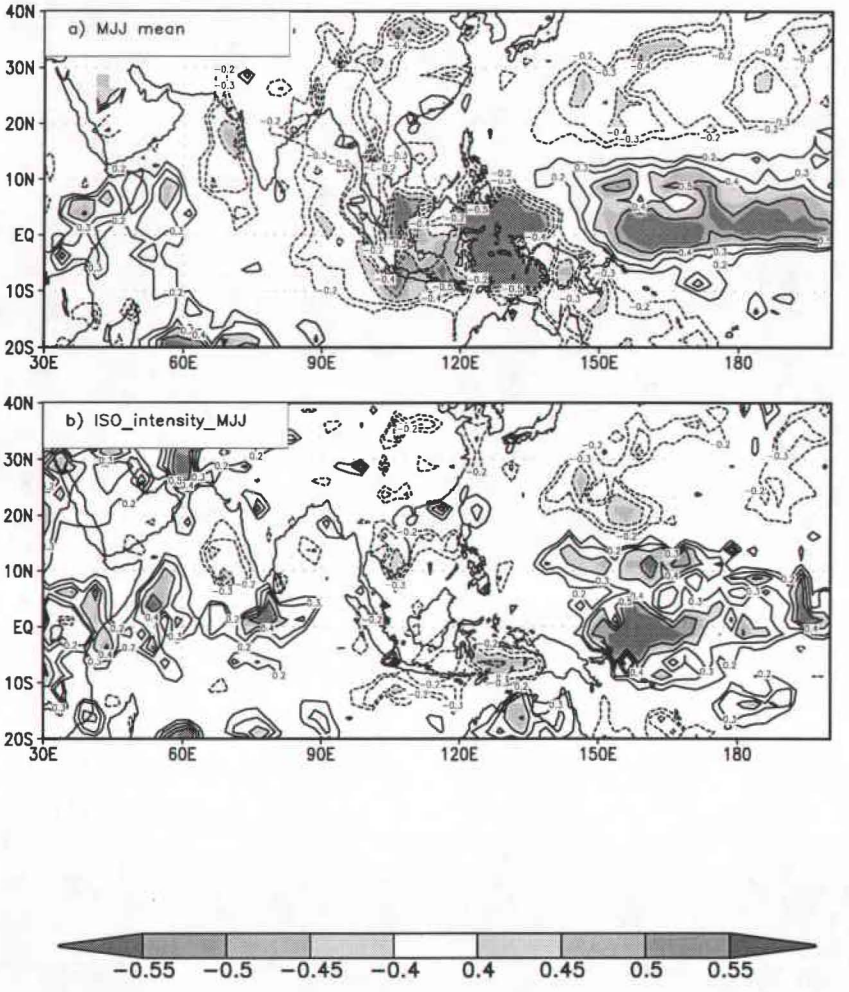

Figure 5.8: Correlation coefficients between the May-Jul MJO index and May-Jul mean CMAP rainfall (upper panel) and the total ISO intensity during May-Jul (lower panel).

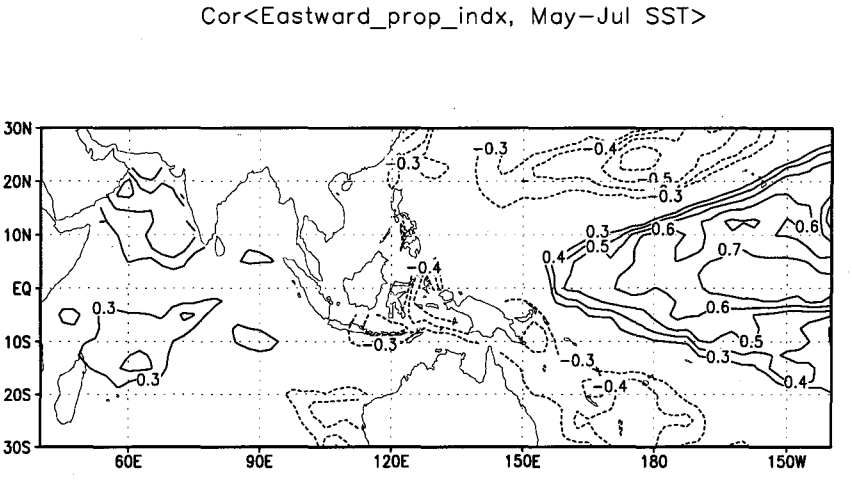

Figure 5.9: Correlation coefficients between the May-Jul MJO index (using OLR) and May-Jul mean SST during the period of 1979-2001.

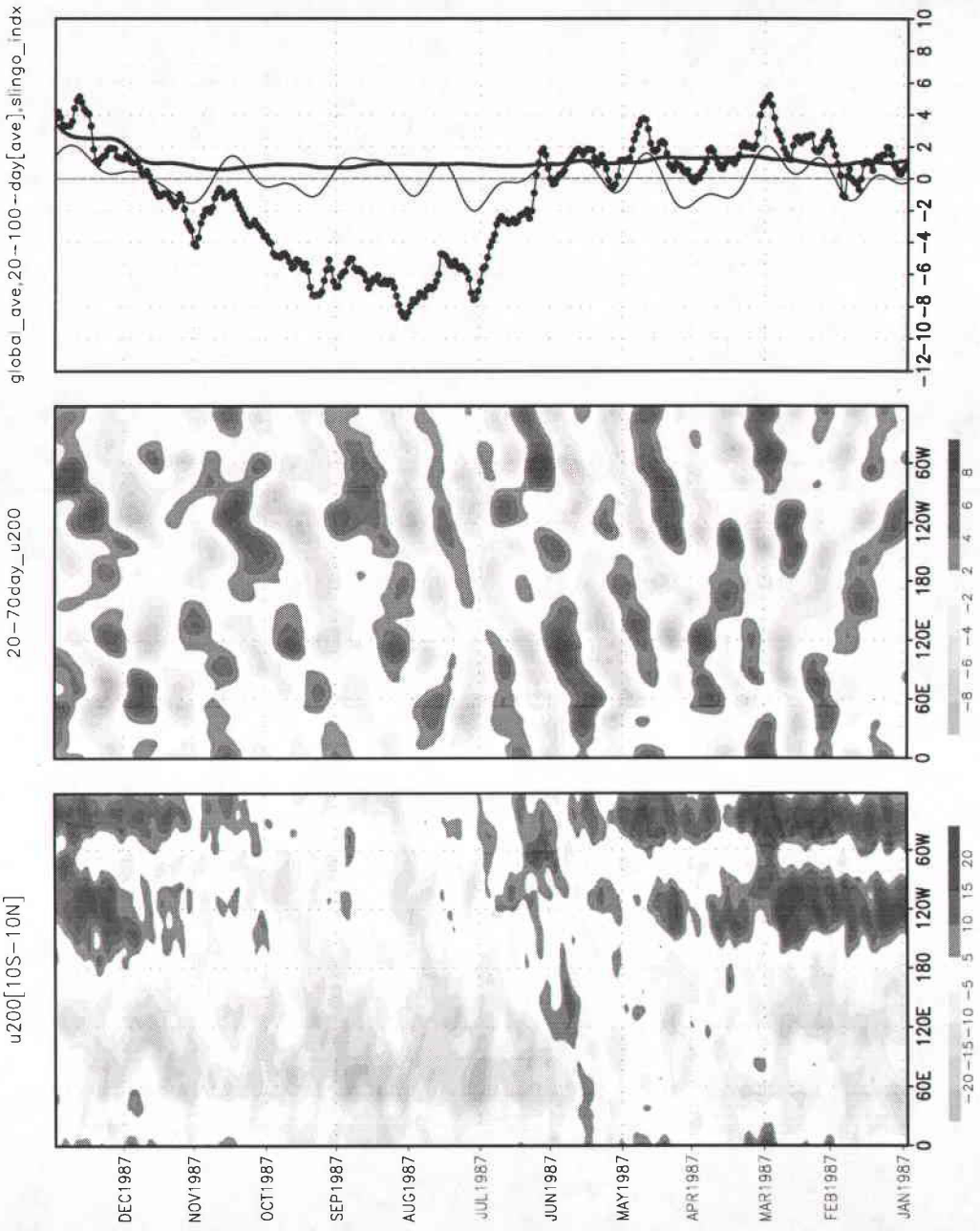

Figure 5.10: The upper panel is the global average (10°S-10°N) 200 hPa zonal wind, the 20-100-day intraseasonal component, and the Slingo et al. (1999) index in the year of 1987. The middle and lower panels are the *Hovmöller* diagrams of the zonal wind and its 20-100-day component.

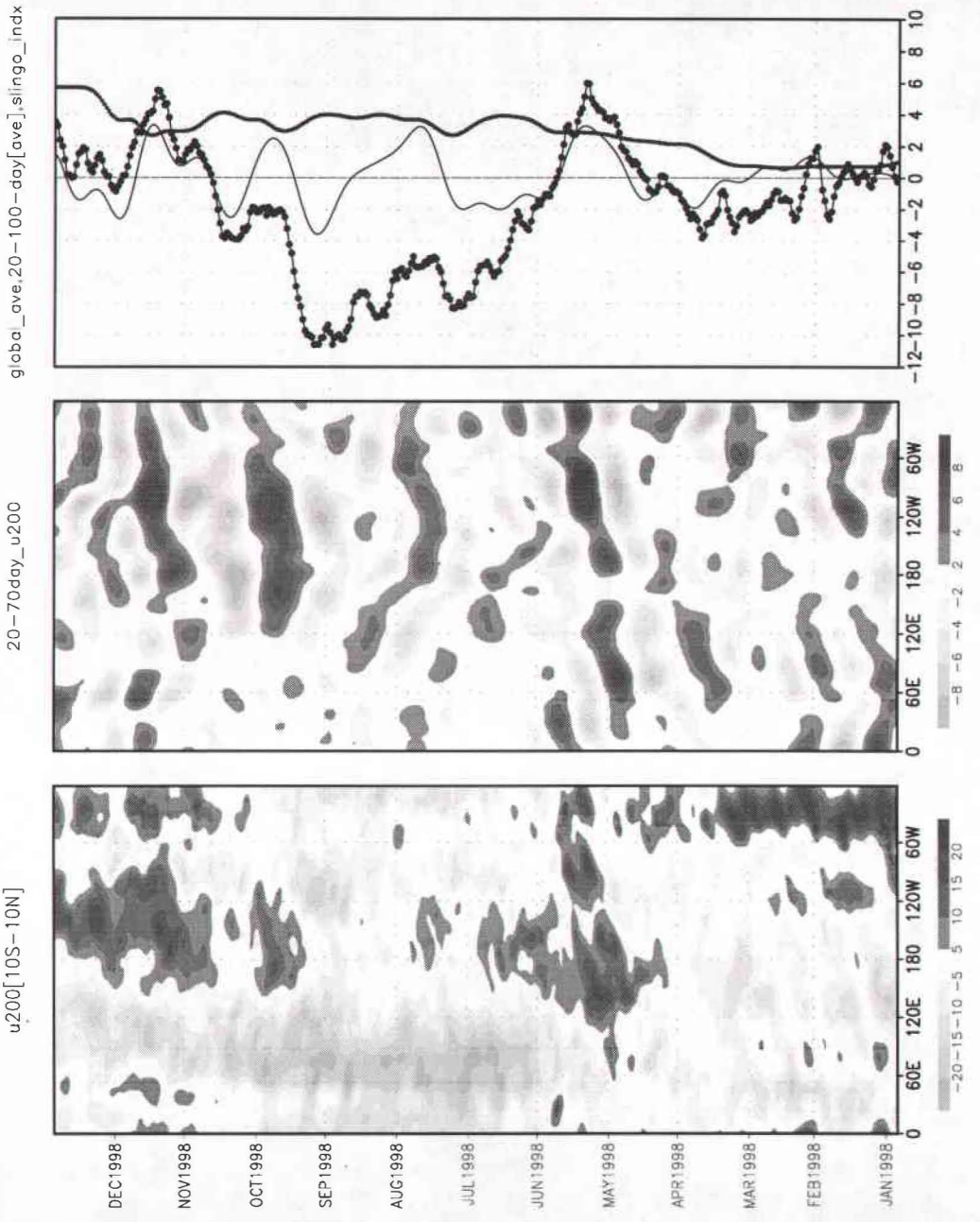

Figure 5.11: Same as Fig. 5.10 but for the year 1998.

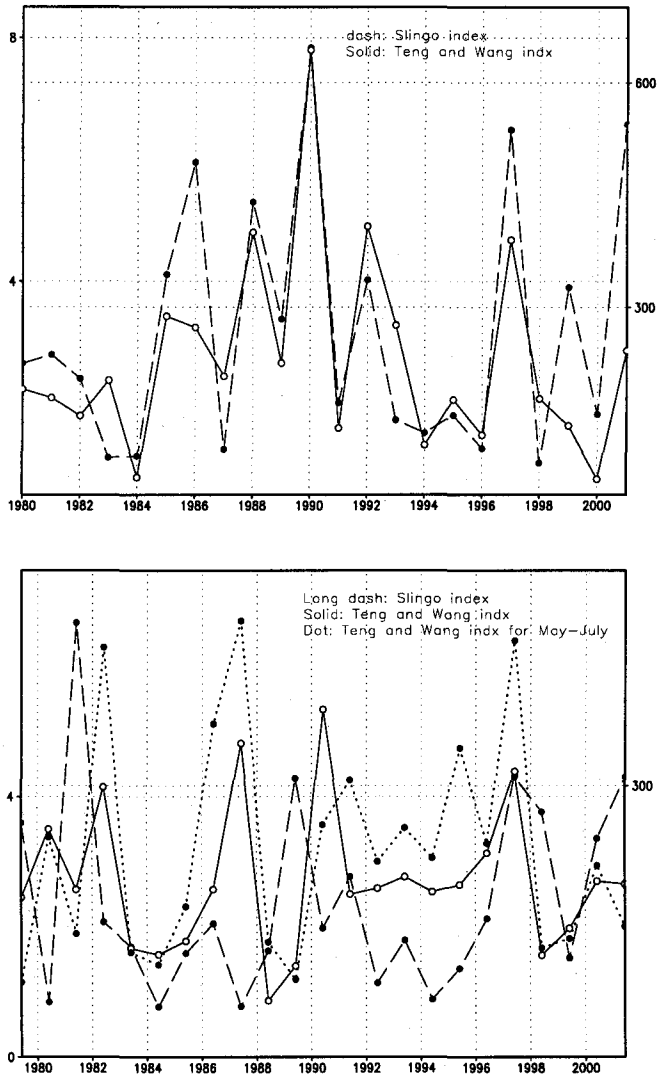

Figure 5.12: Comparison of the Slingo et al. (1999) index with the present MJO index in the boreal winer (upper panel) and summer (lower panel).

Chapter 6

How does ENSO affect the WNP ISO?

6.1 Westward propagating ISO index

The WNP ISO has a predominant northwestward propagation (Lau and Chan 1986). For convenience, here the ISO is investigated in longitudinal and meridional directions separately. This section mainly focuses on the westward propagating component. Because the westward propagation is more pronounced from July to October and it is confined to the longitude domain between 100°-180°E, they are selected as the spatial and temporal domain for wavenumber-frequency analysis.

The ISO intensity in 850 hPa meridional wind (v850) has the most pronounced correlation with ENSO. It is used to define the westward propagating ISO index. Total of 7 wavenumber-frequency spectrum diagrams are produced for each 2.5° latitude bin between 5°-20°N in 1958-2001. The westward propagation index was constructed by averaging the spectrum density associated with wavenumber 1-3 and 10-50-day

westward propagating v850 anomalies between 5°N and 20°N. The latitude domain was not expanded farther north, because the large variability center in the East China Sea may be associated with the mid-latitude intraseasonal oscillation.

The westward propagation index (Fig.6.1) has significant (at the 95level) positive correlation with Nino3.4 SST, with the 44-year correlation coefficient of 0.62. The index also suggests an interdecadal change in around mid- or late- 1970s with the earlier epoch (1958-1978) having weaker westward propagating ISO. It is uncertain whether the interdecadal change is caused by inhomogeneity of the data.

The westward propagating ISO exhibit multi-scales, therefore it is important to examine more wavenumbers. Because wavenumber 1-3 possesses most of the variance, their spectrum densities at different latitudes are correlated with Nino3.4 SST. Fig.6.2 shows the correlation coefficients with Nino3.4 SST for wavenumber-1, -2, and -3 v850 anomalies between 100°E-180°E, respectively. Significant correlations are found between ENSO and the wavenumber-1 and -2 westward propagating v850 anomalies between 5°N and 106oN and the wavenumber-3 anomalies between 5°S and 10°N. For wavenumber-1, -2 and -3 v850 anomalies, the significant periods are about 30 days, 20 days and 15 days. Besides, higher frequencies (period 8days) are also significantly correlated with ENSO warming at about 10°N.

6.2 Northward propagation

The northward migration of rainband in East Asia is directly linked with the meridional propagation of the WNP ISO. But due to lack of observations over the ocean in history, the WNP ISO has received much less attention compared with the ISO in the Indian monsoon region. This section will first compare the strength of the northward propagation at both sectors, followed by examining their interannual variations of the WNP ISO. The northward propagation of the ISO in the Indian summer monsoon region will be intensively investigated in the next chapter.

In order to examine the poleward propagating ISO, wavenumber-frequency analyses are carried out at the meridional direction. There are total of 70 spectra for each 2.5° longitudinal stripe between 40°E and 167.5°W. By choosing the spatial decomposition domain from 5°S to 25°N, the analysis yields variance density of the northward propagating intraseasonal anomalies. Only the wavenumber-1 anomaly at this domain is considered, because it possesses dominant variance. Tests were carried out to ensure the results are insensitive to choices of the domain (e.g. 0°-20°N). Figure 6.3a shows the 44-year averaged spectrum for u850. Three longitude bands of strong northward propagating ISO are identified at 70°-90°E, 110°-120°E, and 125°-140°E. The dominant period is about 30-50 days over the Indian Ocean and the Indian Peninsular. The spectrum broadens over the Philippine Sea. Higher frequency wave activities with oscillating period below 20 days are enhanced.

23-year averaged spectrum for OLR (figure not shown) shows similar feature,

except that it has a separate northward propagation center at 65°E-75°E in the Arabian Sea with a dominant period of 30-50 days. Unlike in the u850 spectrum all three northward propagation centers have similar strength, the OLR spectrum reveals that the Bay of Bengal has the largest variance associated with the 30-50-day northward propagating anomalies. The maximum contours in the averaged OLR spectrum at the Bay of Bengal, the Arabian Sea, the Philippine Sea and the South China Sea are 700, 600, 500, and 400 (W/m2)2, respectively. The year-to-year variability of the northward propagating ISO is measured by interannual standard deviation of the 44-year u850 spectrum (Fig.6.3b) and of the 23-year OLR spectrum (figure not shown). Considering the 30-50-day anomalies, the locations with large interannual variations roughly coincide with the climatological active centers. The notable feature is the pronounced interannual variations of the 20-30 day mode over the Philippine Sea. Besides, there is a small tongue sticking out from a 40-day period in the Philippine Sea to a 30-day period at the dateline, indicating a relatively large interannual variation. The standard deviation in the OLR spectrum (figure not shown) suggests that although the 30-50-day northward propagating ISO is weaker in the Philippine Sea than in the Indian Ocean, its interannual variability is more pronounced compared with those in the Indian Ocean. In addition, 15-20 day oscillation over the Arabian Sea and the Bay of Bengal also shows relatively large interannual variation on in the OLR spectrum.

To find the relationship between ENSO and the northward propagating ISO,

the linear correlation coefficients between the spectrum density and Nino3.4 SST are calculated (Fig.6.4 and Fig.6.5). Significant positive correlations with the u850 spectrum are found from 150°E to the dateline at 15-50 days, 9 days and 6 days (Fig.6.4). The positive correlations drop sharply and become insignificant when crossing the South China Sea. Slightly significant negative correlations are found in the Arabian Sea at 70°-80°E at an oscillating period of 15-20 days. The negative correlations in the Arabian Sea are much weaker than the positive correlations in the Pacific regarding to both the absolute values of the correlation coefficient and the spatial areas that possess a statistical significance. Correlation coefficients between the 23-year OLR spectrum and Nino3.4 SST are less significant (Fig.6.5). Positive correlation is restricted to 160°E-170°W with enhanced 30-day, bi-weekly, and 8-10 day oscillations in *El Niño* .

As a summary, the boreal summer ISO exhibits larger year-to-year amplitude change over the WNP than in the Indian monsoon region. The wavenumber-frequency spectrum suggests that the westward and northward propagation of the ISO in the WNP is significantly associated with ENSO condition. When the central-eastern Pacific warms up in the boreal summer, the ISO is enhanced in the WNP with stronger westward propagation and northward propagation components on the periods of 15-40 days and 8-10 days. *El Niño* can also significantly enhance the May-Jul MJO. The northward propagating ISO in the Indian monsoon region does not seem to be sensitive to ENSO.

6.3 Why is the western North Pacific ISO intimately linked to ENSO?

Chapter 4 has shown that the WNP has the largest interannual variation in the strength of the summertime ISO. It is unclear how ENSO can influence the ISO in the off-equatorial western Pacific and Southeast Asia, given the fact that the seasonal mean circulation is primarily affected by ENSO in the equatorial western Pacific.

Figure ?? shows linear correlation coefficients between the 44-year boreal summer ISO intensity and May-Oct seasonal mean, both using 850hPa zonal wind. Significant positive correlation prevails in the WNP from the equator to 20°N, whereas significant negative correlations are over the central Maritime Continent. In the Indian monsoon region, significant correlation is only found over the upper Ganges River valley. Compared with the ISO in the Indian monsoon region, the ISO in the WNP is more sensitive to change in summer's mean state.

Theoretical studies have demonstrated that the vertical shear of the zonal flows has a remarkable impact on Rossby wave and westward propagating mixed Rossby-gravity waves (Wang and Xie 1996; Xie and Wang 1996). Easterly vertical shears (easterly wind increases with height) can enhance Rossby wave in the lower troposphere, whereas westerly shear tends to trap Rossby waves in the upper troposphere. Furthermore, in the presence of moist convection, enhanced low-level perturbation increases boundary layer moisture convergence, which in turn interacts with convective

heating. Therefore, enhanced easterly shear favors amplification of moist equatorial Rossby waves.

Climatologically, the western Pacific is a transition area between easterly and westerly shears (Fig. 6.7a). Yet the western Pacific region has the most pronounced interannual variation associated with ENSO (Fig. 6.7b). Because the western Pacific has a weak vertical shear, it is easier for ENSO-induced circulation anomalies to reverse the sign of the vertical wind shear and cast dramatic impacts on Rossby wave response. When there is a basin-wide warming in the central-eastern Pacific, it induces westerly anomalies in the lower troposphere and easterly anomalies in the upper troposphere over the western Pacific, which results in pronounced vertical shear changes between *El Niño* and *La Niña* summers (Fig. 6.7b). The change in vertical shear (about half of the difference of Fig. 6.7b) in *El Niño* and *La Niña* summers is comparable to the climatological mean shear in the WNP. In West India and the equatorial eastern Indian Ocean, there is a weak decrease/increase of easterly shear in the *El Niño* /*La Niña* summers. But they are only a moderate fraction of the mean shears.

The dominant interannual modes of the summer ISO intensity in v850 (Fig. 6.8b) are related to summer mean vertical shear (Fig. 6.8a). The dominant Singular Vector Decomposition (SVD) mode between the mean vertical wind shear and v850 ISO intensity accounts for 84.6% of their total covariance, far ahead of the second mode (5.6%). The correlation coefficient between the temporal coefficients is 0.94. In

the first mode, the pattern of the mean vertical shear resembles the ENSO anomaly pattern in Fig. 6.7b . It contributes to 49.4% of its total variance. The SVD pattern for the ISO intensity mirrors that of the interannual ISO variability in the WNP. It explains 26.5% of the total variance. Both patterns resemble their individual dominant empirical orthogonal function (EOF) (figure not shown). From the 1st SVD mode, the reconstructed mean vertical shear and the v850 ISO intensity both contribute to more than 50% of its individual interannual variance in the WNP (Fig. 6.9).

The weak mean monsoon vertical wind shear and its strong interannual variation cause the ISO to have larger interannual variations in the WNP than in the Indian monsoon region. During El Nino, the enhanced mean easterly vertical shear over the WNP is responsible for the enhanced emanation of the moist equatorial Rossby waves. These waves have a periodicity of 8-10 days but their amplitude is modulated in 30-40 day time scale due to vigorous air-sea interaction (Kemball-Cook and Wang 2001). This leads to an enhanced ISO on time scale of 30-40 days and 8-10 days.

6.4 How does ENSO affect the phase of the WNP ISO?

One unique feature of the WNP ISO is its phase-locking to the annual cyle. Four climatological ISO (CISO) are identified from May to October (Wang and Xu 1997): prelude cycle, onset cycle, peak cycle and withdraw cycle. Each cycle contains a wet and a dry phase. The intraseasonal anomalies predominantly move northward and westward in early and late summer, respectively. It was speculated that the planetary-scale circulation change, or annual cycle, is responsible for both the timing and different propagation patterns of the four cycles. The four CISO cycles signify different phases of the Asian summer monsoon. Therefore, the extreme CISO phases are also called monsoon sigularities. ENSO can break down the sigularities and causes significant interannual variations.

This section mainly focuses on 120°-150°E, $10° - 20°$N to investigate how ENSO causes pronounced interannual variations in the WNP ISO. This oceanic area exhibits a strong monsoon character. Intense convection appears in July to September (Wang and LinHo 2001). It is during this season that active northwestward propagating ISO is evident (Kemball-Cook and Wang 2001). Lander (1994) found a large-scale vortex, called monsoon gyre, was often organized in the lower troposphere at appearance of several tropical cyclones in the WNP monsoon trough region. The latent heat that the monsoon gyre generates from late July to September is comparable to that

produced by the Indian monsoon at its earlier peak season. Together, they compose the most significant subseasonal variation of the Asian summer monsoon (LinHo and Wang 2001). After the tropical cyclones move off the tropical region, the monsoon gyre quickly disappear.

Domain averaged climatological 850 hPa vorticity and CMAP (Fig. 6.10a) show three consistent convective peaks at pentad42, 46 and 50-52. Late July (pentad42) is usually the onset for the monsoon gyre (Lander 1994). Concurrently, the subtropical ridge rapidly moves northward to Japan, and ends the Baiu season (Ueda et al. 1995). When the subtropcial high retreats and the convection zone moves back to the equator in October, this domain is sandwiched between strengthening trade wind to the north and the equatorial westerly to the south. Therefore, although the 850 hPa vorticity continues to grow, the monsoon gyre actually has vanished. The corresponding large-scale rainfall in the WNP has dramatically decreased. The monsoon gyre (or the confluence zone) is known as the "cradle" for typhoons (Lander 1994). Fig. 6.10b shows the total numbers of JTWC's named tropical depression, tropical storm and typhoon that have lived at least one day in this domain at each given pentad from 1958-1999. Three peaks are identified at around pentad40-42, pentad52, and pentad56-58. The first two peaks are coherent with the climatological 850 hPa vorticity and CMAP. Such coincidence has caused controversy whether the WNP ISO is nothing but a school of tropical cyclones. Observation on the monsoon gyre (Lander 1994) strongly supports that large-scale system triggers and regulates

the smaller scale convection (Holland 1990). It is interesting that pentad46 is a peak in CMAP and 850 hPa vorticity, but is a relatively peaceful spell in tropical cyclone activity. People should be cautious that the active episodes at pentad42, 46 and 52 in the climatology are not found in each year. For example, two normal distributions with different sample means will together produce a bi-modal climatology.

The conjecture is that ENSO can affect the WNP ISO in not only its intensity but also the timing of the active/break events. The central-eastern Pacific warming/cooling can induce a cyclonic/anti-cyclonic circulation anomaly in the lower troposphere in the WNP, and an anti-cyclonic/cyclonic anomaly in the upper troposphere as a Gill-type response. Correspondingly, easterly/westerly vertical shear prevails. With a easterly wind shear anomaly, the establishment of the monsoon gyre can be experdited. On the contrary, westerly shear anomaly slows down or even prohibits the process.

The early/late onset of the monsoon gyre may further influence the timing of the following 20-40-day events. To test it, the averaged 850 hPa vorticity are grouped into 21 warm summers and 21 cold summers (Fig. 6.11). The pentads that has a statistically significant difference in the two groups are highlighted. The following features are found: First, the monsoon gyre is significantly stronger in the warm summers than in the cold summers from July to September, except at pentad43-45; Second, the domain averaged 850 hPa vorticity exceeds zero at pentad34 in warm summers' composite, 2 pentads earlier than the cold summers; Third, in July-

September, the warm summers have two major peaks at pentad41 and pentad52, and a minor one at pentad46. The cold summers' composite peaks first at pentad43-45. After a break at pentad47, it keeps growing till mid-October; Fourth, two groups do not distinguish from each other from mid-October till late November. When ENSO extreme warm/cold events mature in the ensuing winter, anti-cyclonic/cyclonic circulation anomaly take the place of cyclonic/anti-cyclonic anomaly in the Philippine Sea. This phenomena is not significant here because ENSO extreme cases only account for a small portion of our sample.

In seek of more evidence from another independent data set, the histogram in Fig. 6.10b was grouped into warm and cold ensembles (Fig. 6.12). Earlier it was found that the WNP ISO is stronger in the warm summers. This is also reflected by the large intraseasonal variations in the numbers of tropical depression and tropical storm in the warm summers, and a rather uniform temporal distribuation in the cold summers. It is easy to recognize that pentad 45-48 has weak tropical cyclone activity in the warm summers, located between two histogram peaks at pentad41 and 52. Active/break periods are not discernible in July-September in the cold summers. The numbers for both ensembles are comparable in October. In November, the numbers in the cold summers exceed those in the warm summers.

In order to examine whether ENSO warm events tunes pentad40-45-50 to active-break-active episode of the ISO, domain averaged 850 hPa vorticity for the extreme ENSO cases are plotted (Fig. 6.14). 4 out of the 7 *El Niño* summers (63,

65, 82, 87) agree with the above assertion. Two recent *El Niño* summers (91, 97) have an ISO active episode at pentad45, thus total of three active episodes exists in July-September. A vorticity peak is found at pentad43-47 in the cold summers in 64, 70, 73, 75, 98. But overall, the value of the vorticity is much smaller than in the warm summers. It barely exceeds zero in July-September 1988 and 1998, which excludes the existence of monsoon gyre. Lander (1994) also mentioned that the monsoon gyre (with a more strict definition) appeared almost once in two or three years in his 10-year's record.

To further test the phase shift of the WNP ISO, a 2-D picture is presented in Fig.6.15. Composites are made using a 4-pentad mean minus a surrounding 12-pentad mean with the center located at pentad40, 45, and 50 respectively. Positive (negative) anomaly represents a 20-day convective active (break) episode with a 60-day period. The anomalies in the *El Niño* summers are distributed zonally, with the equator-10°N, 10° – 20°N and 20° – 30°N out of phase. Positive and negative phases alternate at the three pentads. The temporal and spatial wave-like patterns suggest a meridional propagation of the 60-day ISO. Similar Rossby wave pattern has been presented by Nitta (1987). The north-south dipole structure at Japan and the subtropical WNP near 20° was termed as the Pacific-Japan (PJ) pattern. He also proposed that Rossby waves are generated near the Philippines and propagate to Japan, and thereafter to North America through teleconnection. In the *La Niña* summers, the south-north wave path tilts to southwest-northeast, with large anomalies in South China Sea

and the subtropical Pacific south, and southeast of Japan. Positive-negative-positive anomalies prevail in the Philippine Sea at pentad40-45-50 in the *El Niño* summer. The WNP is not an active center in the *La Niña* summer. Negative-positive-negative anomalies are observed at the South China Sea and the East China Sea at pentad40-45-50.

6.5 Roles of atmosphere-ocean interaction

Warm SST is a critical condition for deep convection. Besides ENSO, the local SST has been an important aspect in understanding the ISO's interannual variations. For example, Nitta (1987) found the ISO was stronger when the local SST was warmer. The aforementioned observation shows that the WNP ISO is stronger during *El Niño* developing summer, when WNP SST is usually cooler. Why didn't the cooler SST suppress the ISO?

To address the question, long record of SST with a fine temporal resolution is demanded. The NCEP pentad mean skin temperature from 1982-1999 is employed here. Data in this period is interpolated from weekly Reynolds SST, and shows consistent quality. Domain average at 120° – 160°E, 10° – 20°N in 1982-1999 are calculated in two groups based on Jun-Oct Nino3,4 SST $>$ / $<$ 0. The pentads that display significant difference between two groups are highlighted with dots (Fig. 6.16, upper panel). In the warm summers, SST decreases at two steps: pentad35-45 and pentad45-55, in contrast to the cold summers that SST oscillates. Cold summer SST

rises at pentad35-41, drops to a minimum at pentad45, then rises again till pentad50. Significant distinction between the two groups start to appear in September. It is after the peak phase of the convection. Meanwhile, stronger 850 hPa vorticity (Figure not shown) and weaker shortwave radition (Fig. 6.16 lower panel)are found during Jul-Sept of the *El Niño* summers. They suggest the cooler WNP SST is resulted from stronger intraseasonal convection in the *El Niño* summers.

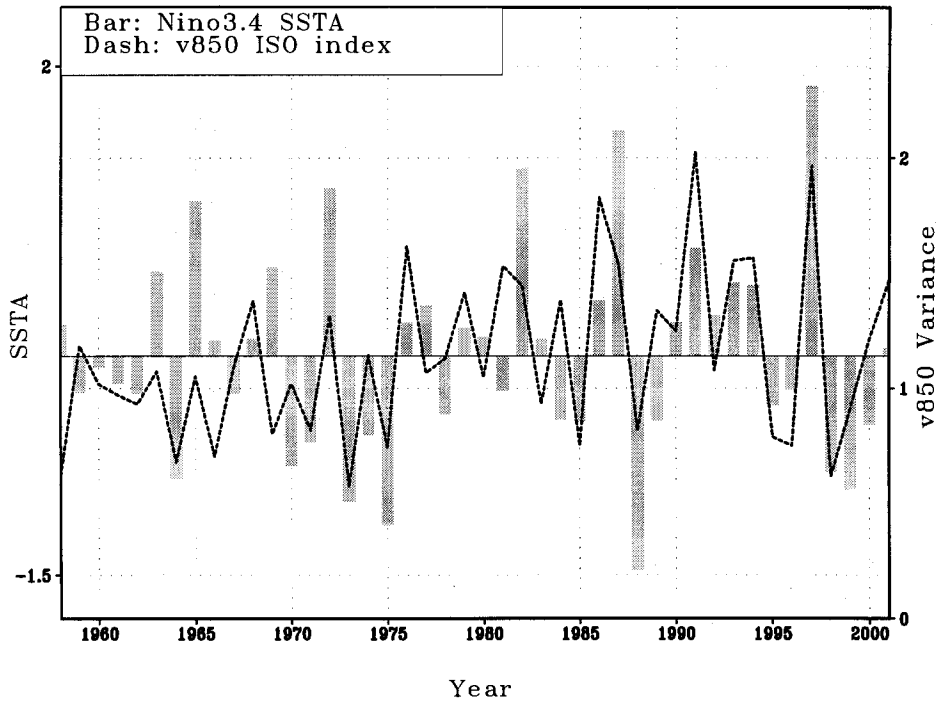

Figure 6.1: 1958-2001 July-October mean Niño3.4 SST anomaly (bar) and mean spectrum density of 10-50-day wavenumber1-3 (at 100°E-180°E) westward propagating 850 hPa meridional wind anomaly (dash) averaged at 5°N-20°N. Wavenumber 1 corresponds to wavelength of 80 deg of longitude.

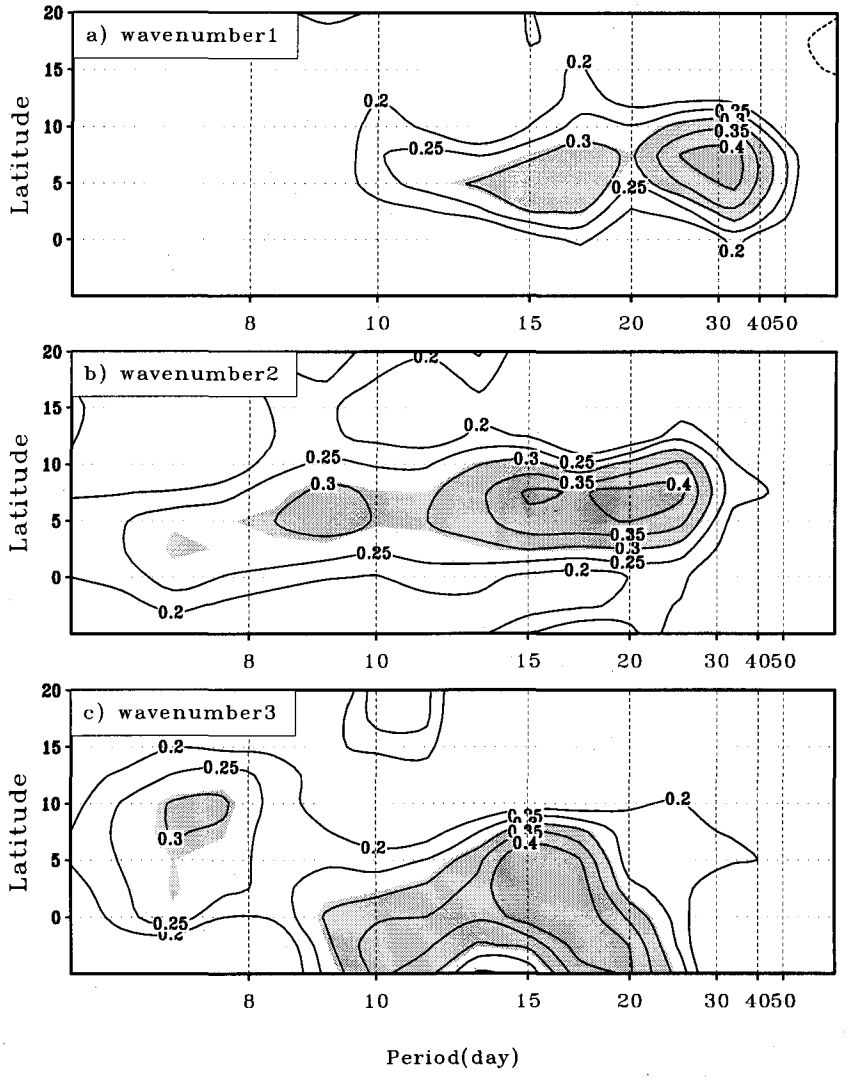

Figure 6.2: Correlation coefficients between 1958-2001 Niño3.4 SST anomaly and spectrum density of the westward propagating intraseasonal anomalies of v_{850} as a function of latitude and period. (a)-(c) are for wavenumber-1, wavenumber-2, wavenumber-3 westward propagating anomalies within 100°E-180°E, respectively. Shading indicates the 95% confidence level. Contours with values between -0.2 and 0.2 are omitted.

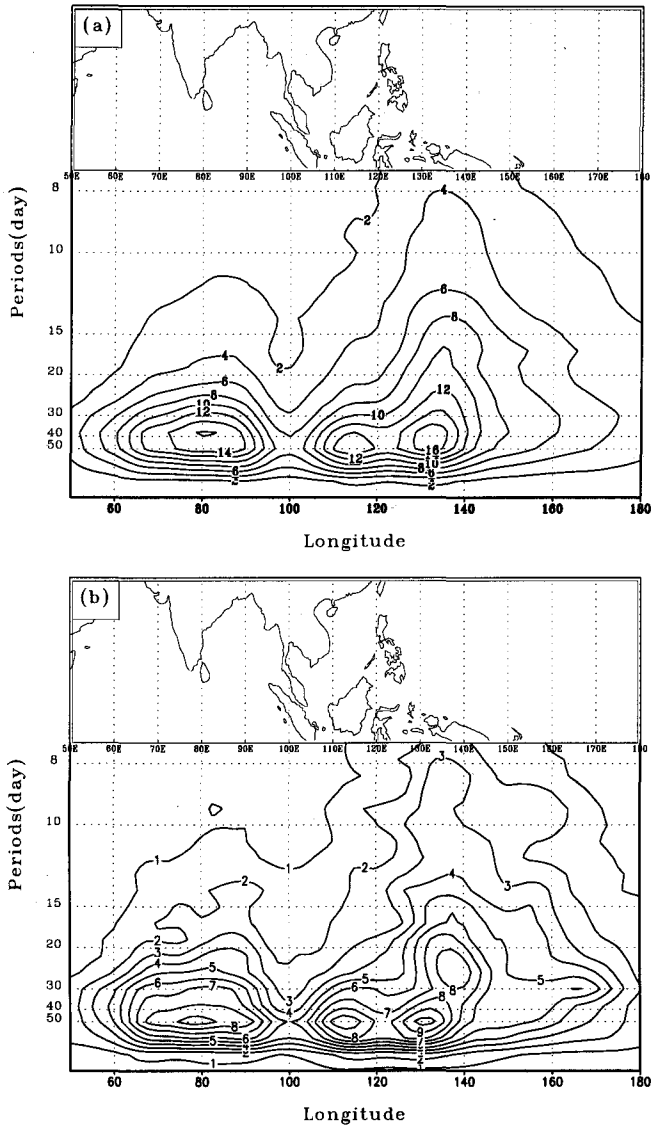

Figure 6.3: (a) Mean and (b) standard deviation of 1958-2001 spectra as a function of longitude and period for wavenumber-1 northward propagating 850 hPa zonal wind anomalies in May-October. The reference map shows the meridional spatial decomposition domain (5°S-25°N) and longitudinal domain of interest.

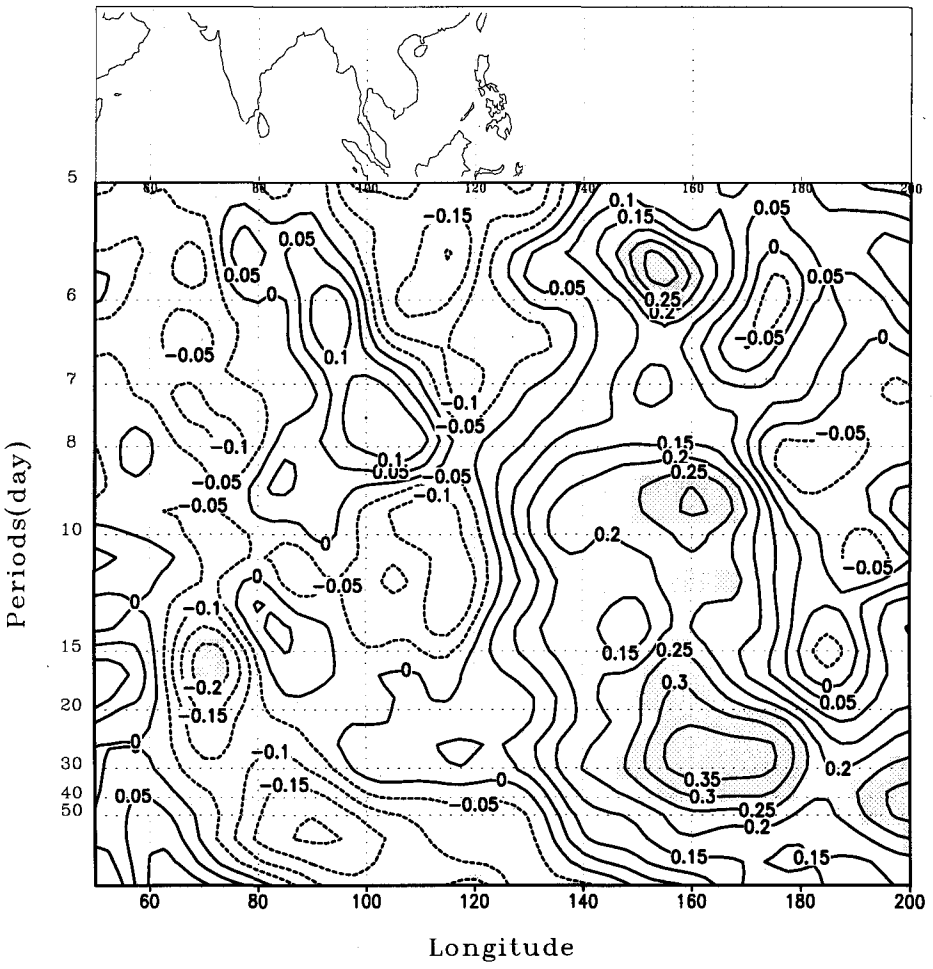

Figure 6.4: Linear correlation coefficients of the spectrum density for the wavenumber-1 northward propagating u_{850} anomalies with reference to Niño3.4 SST anomaly in the period of 1958-2001. Shading indicates the 95% confidence level. 9-point smoothing has been applied on the coefficients.

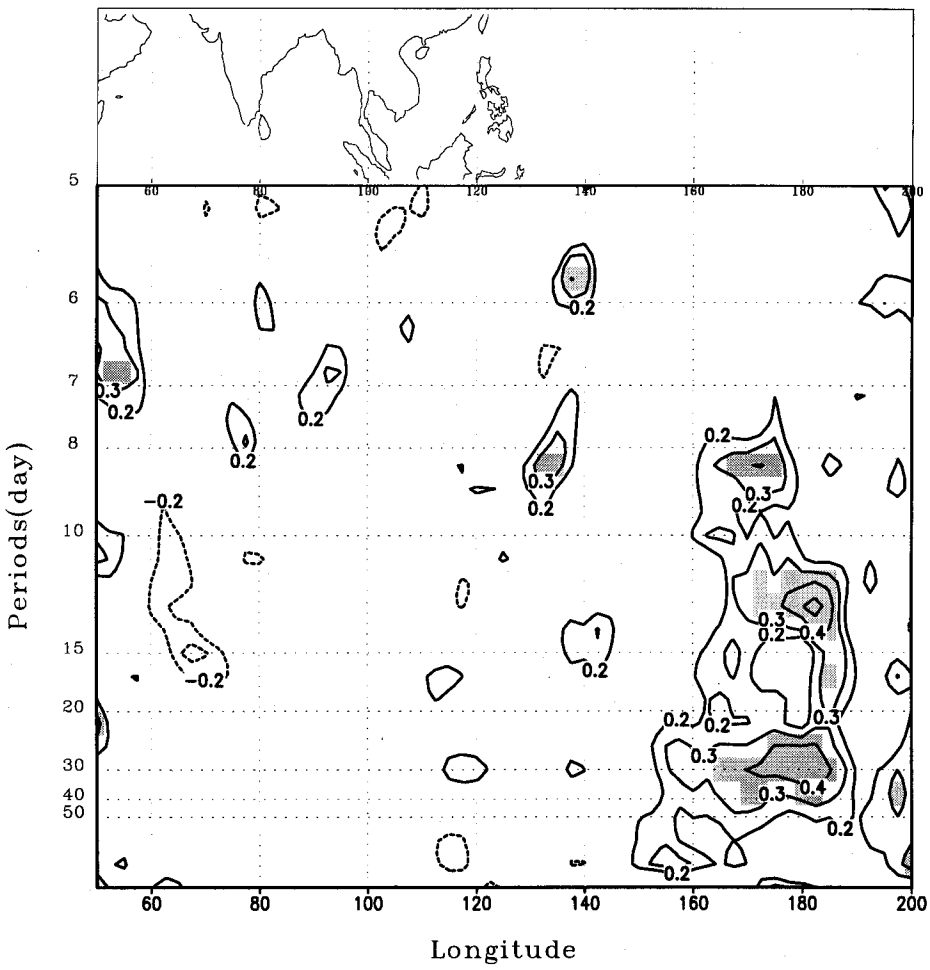

Figure 6.5: Same as Fig.10 but for correlation with OLR spectrum during 1979-2001. Contours with values between -0.2 and 0.2 are omitted.

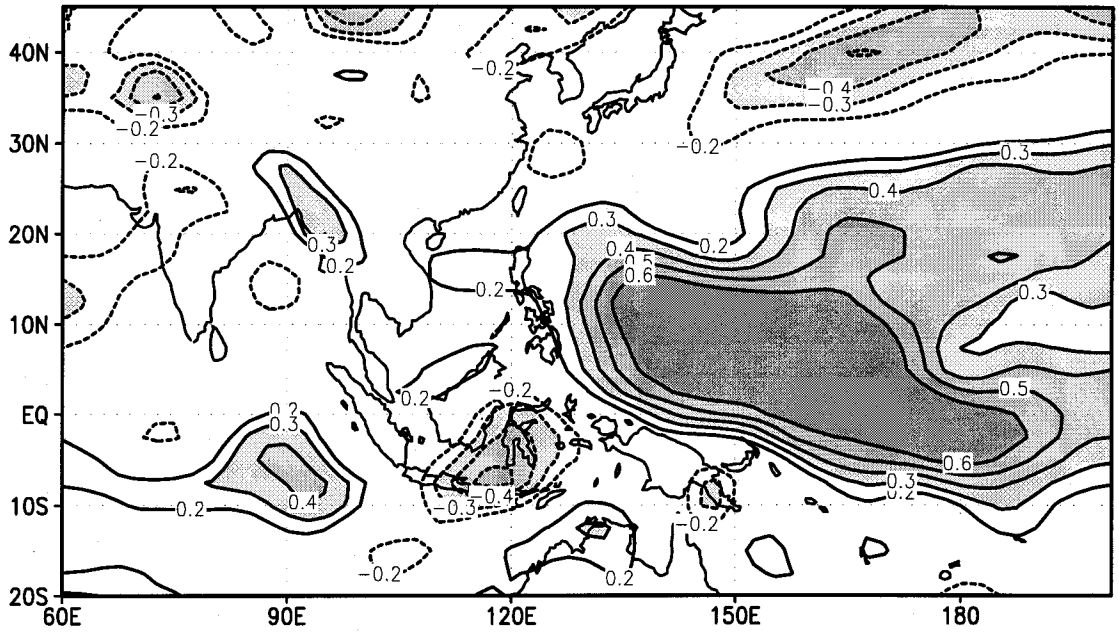

Figure 6.6: Correlation coefficients between the boreal summer ISO intensity and May-Oct seasonal mean both using 850 hPa zonal wind in the period of 1958-2001. Shading indicates the 95% confidence level. Contours with values between -0.2 and 0.2 are omitted.

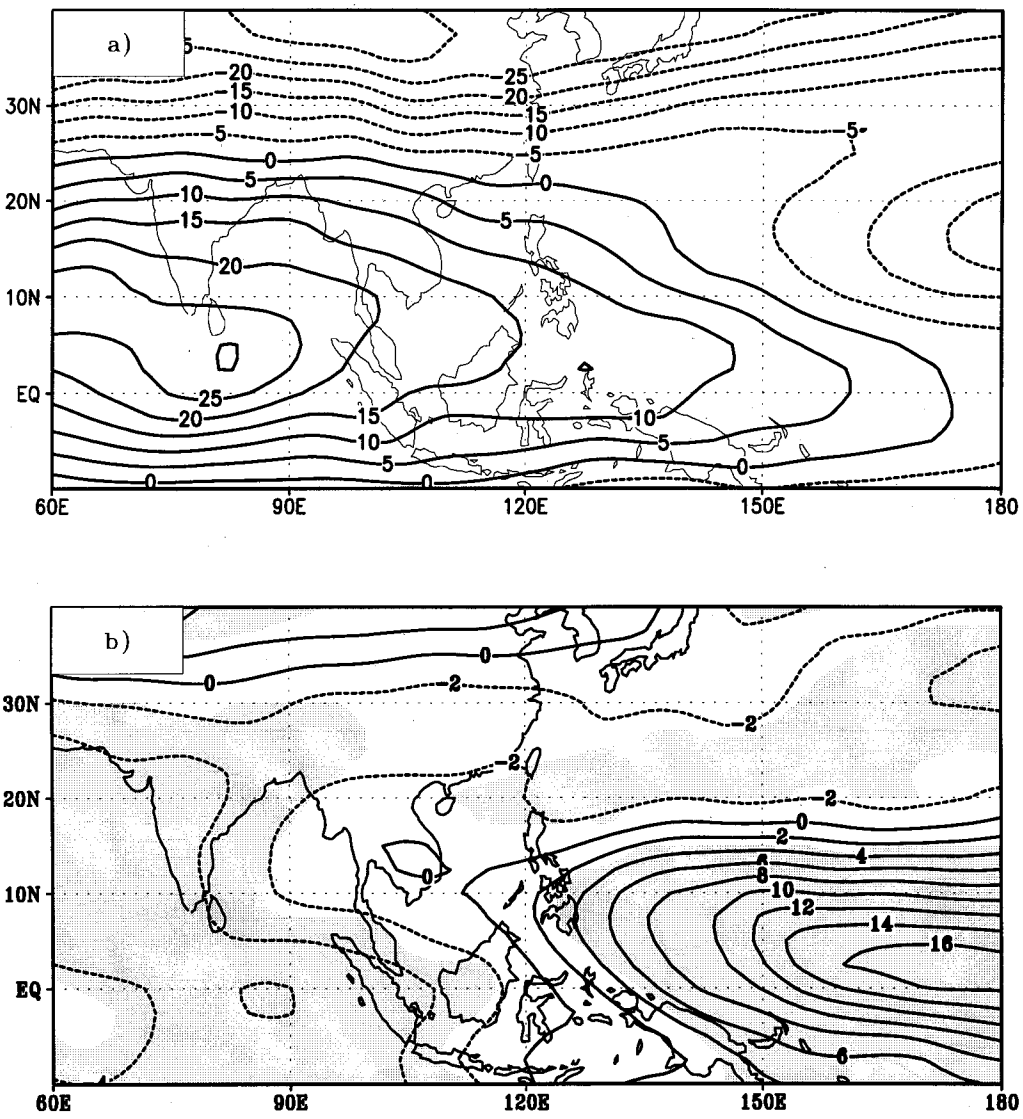

Figure 6.7: (a) 1958-2001 May-October averaged $u_{850} - u_{200}$ shear; (b) May-October $u_{850} - u_{200}$ shear difference between 7 strong El Niño summers (63, 65, 72, 82, 87, 91, 97) and 7 strong La Niña summers (64, 70, 73, 75, 88, 98, 99). Shading indicates two-sample t-test's 95% confidence level.

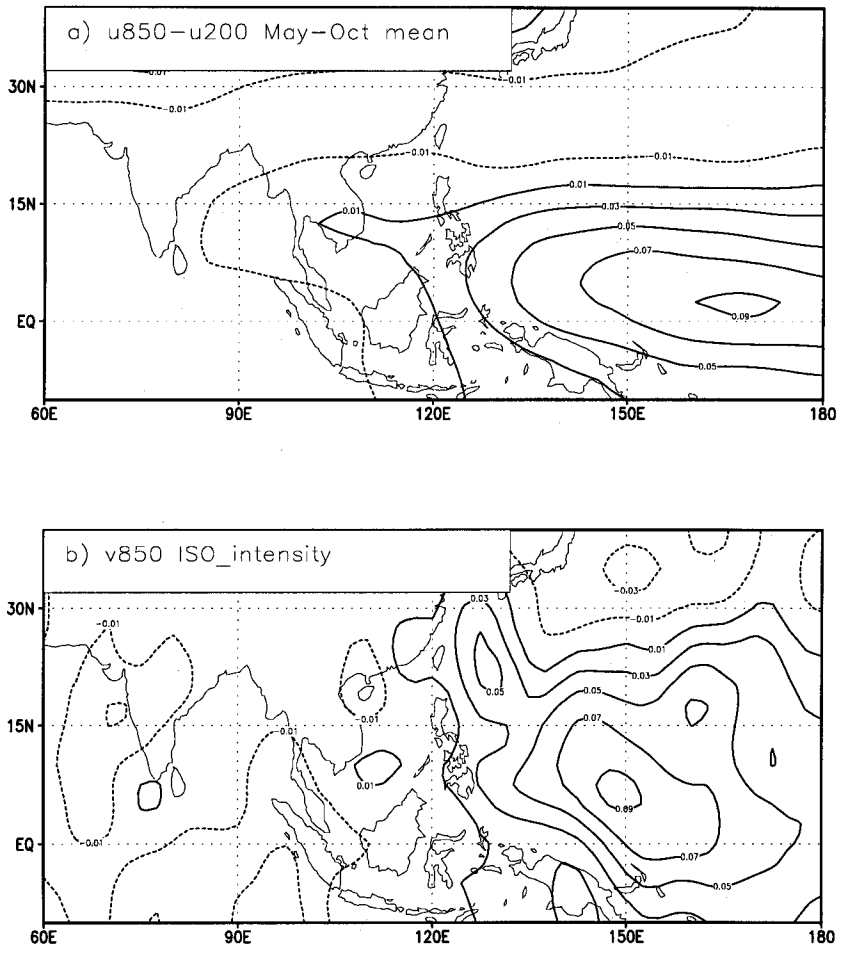

Figure 6.8: The dominant SVD mode between Jul-Oct mean $u_{850} - u_{200}$ vertical wind shear and the v_{850} boreal summer ISO intensity in Jul-Oct 1979-2001. They account for 84.6% of the total covariance, compared with 5.6% from the second dominant mode. The dominant mode of the vertical shear (a) contributes to 49.4% of its total variance. The dominant mode of the boreal summer ISO intensity (b) contributes to 26.5% of its total variance. Correlation between the two temporal coefficients of the first SVD mode is 0.94.

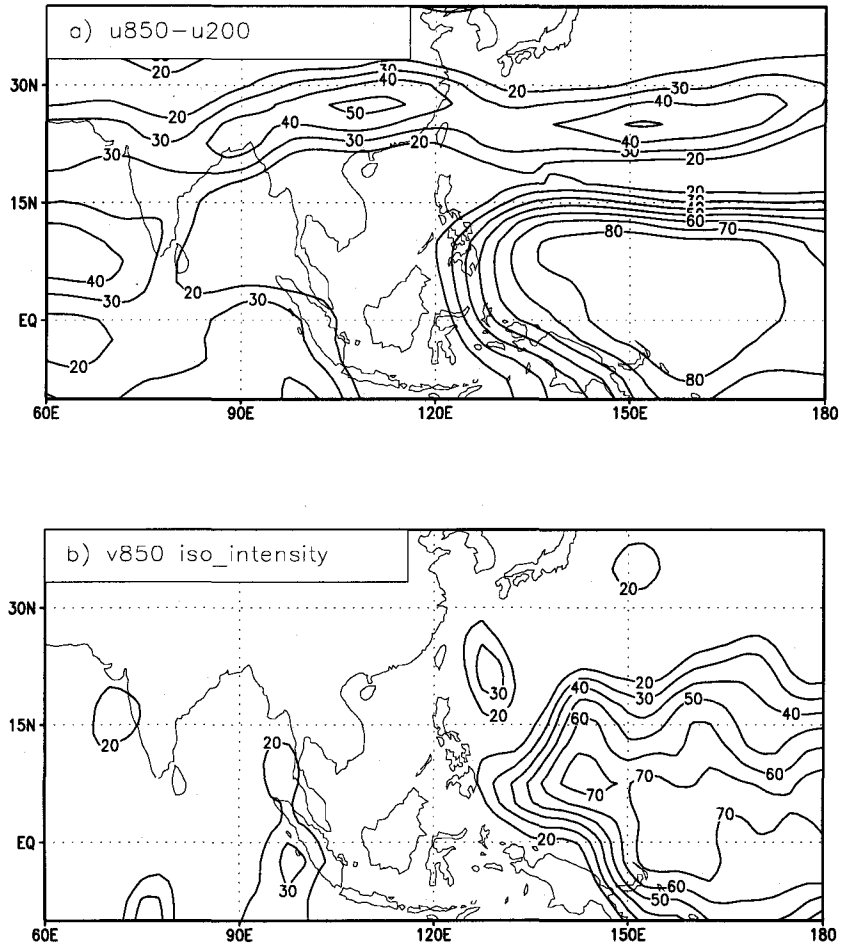

Figure 6.9: Fractional variance that the first SVD mode (Fig.6.8) contributes to the interannual variance of a) the mean $u_{850}-u_{200}$ and b) the boreal summer ISO intensity using v_{850} at each individual grid point in Jul-Oct from 1979 to 2001. The values are in percentage. Contours with values below 20 are omitted.

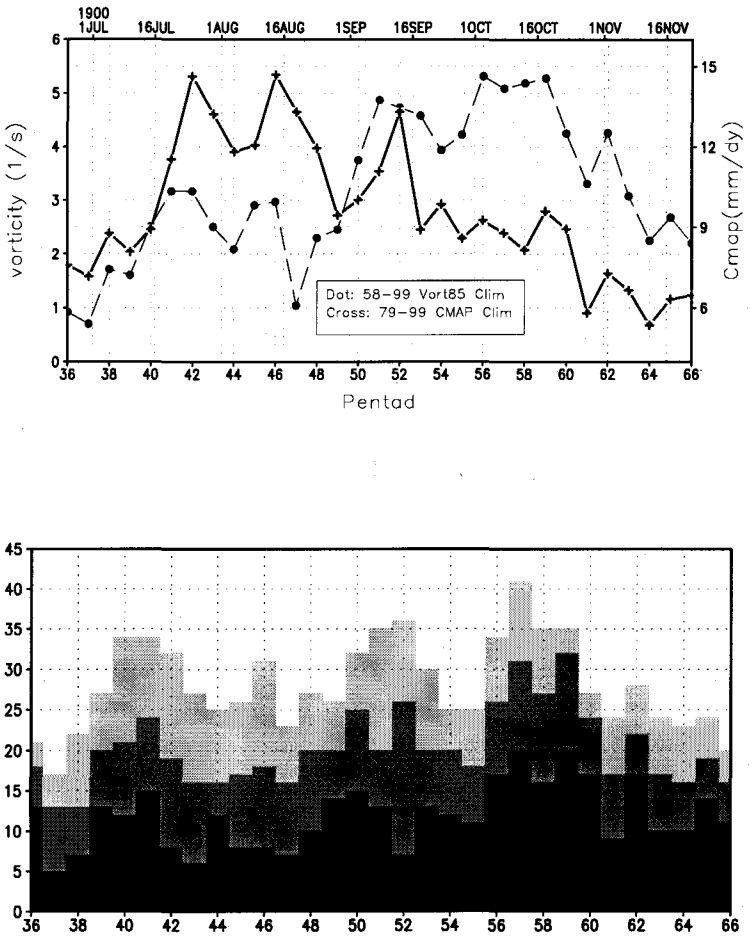

Figure 6.10: Domain ($120° - 150°$E, $10° - 20°$N) average of 1958-1999's climatological NCEP 850 hPa vorticity and 1979-1999's climatological CMAP (upper panel) and total numbers of tropical depression, tropical storm, and typhoon at this domain in 1958-1999.

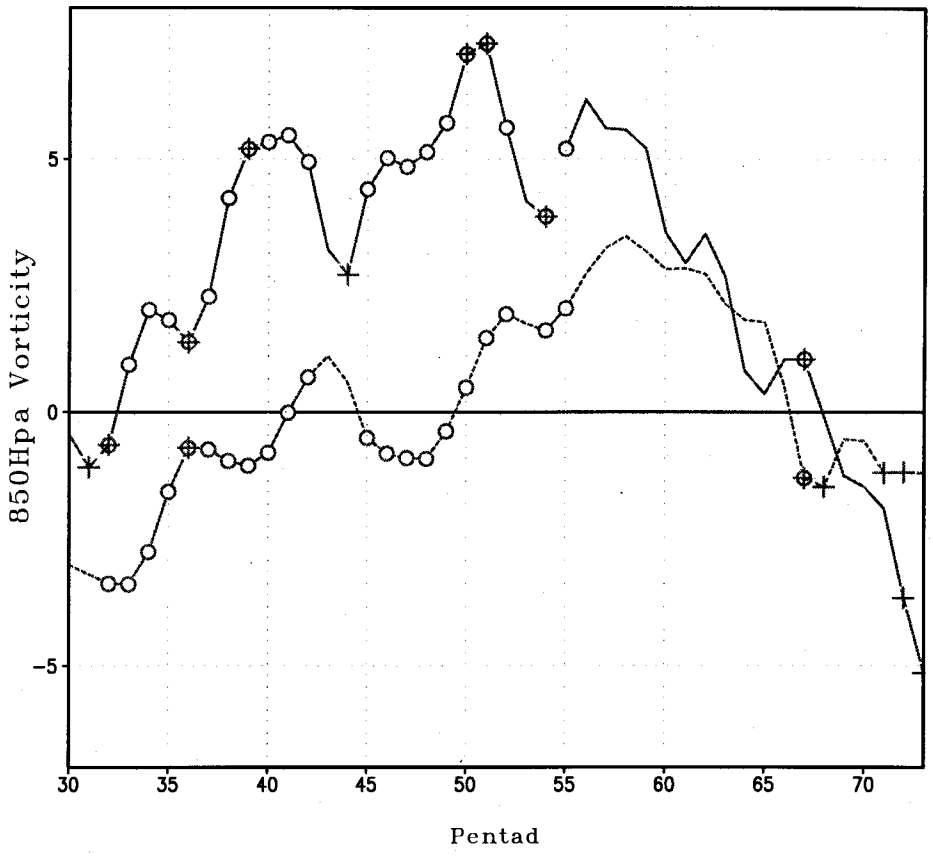

Figure 6.11: Composites for 850 hPa relative vorticity in 21 warm (solid line) and 21 cold (dash line) summers from 1958 to 1999. Warm/cold summers are defined as that with June-October averaged Nino3,4 SST anomaly above/below zero. Dots denote two-sample t-test's 95% significant level.

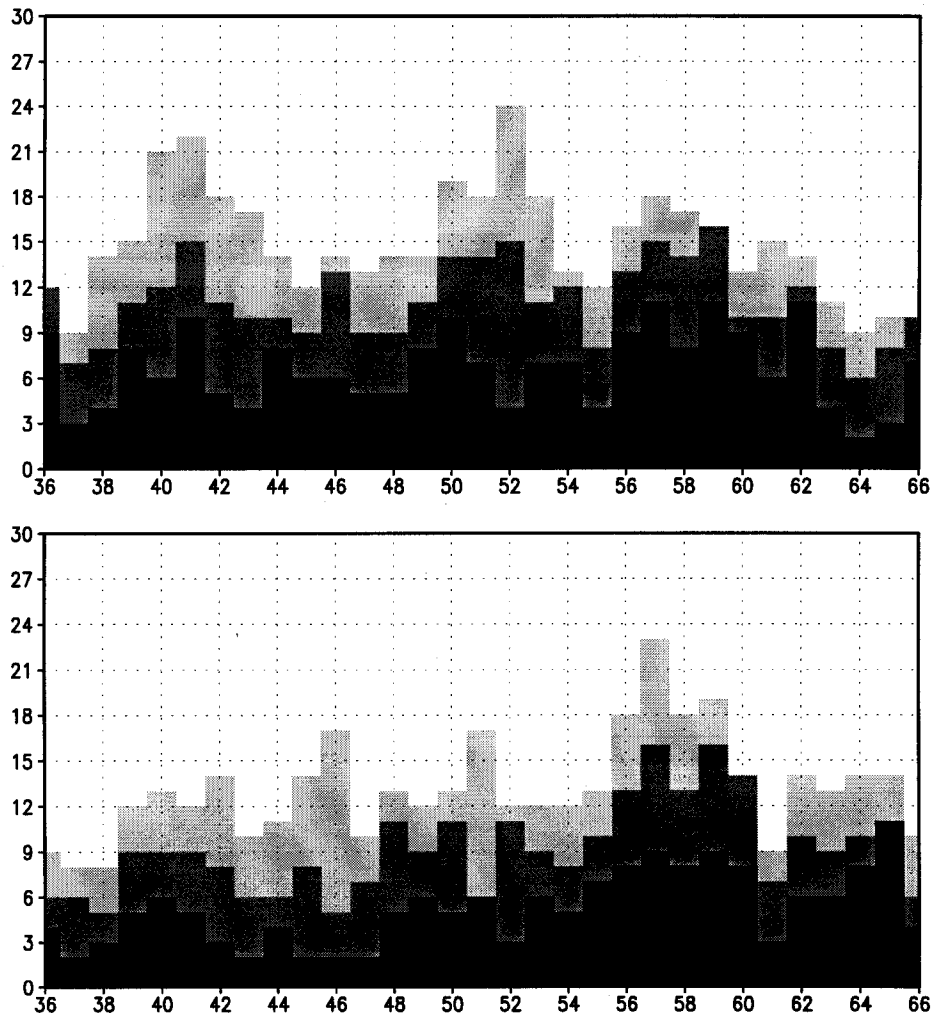

Figure 6.12: Total numbers of tropical depression, tropical storm, and typhoon that have stayed at least 5 days in the domain of 120° – 150°E, 10° – 20°N, in 21 warm summers (upper panel) and 21 cold summers (lower panel). The definitions of warm and cold summers are same as Fig.6.11

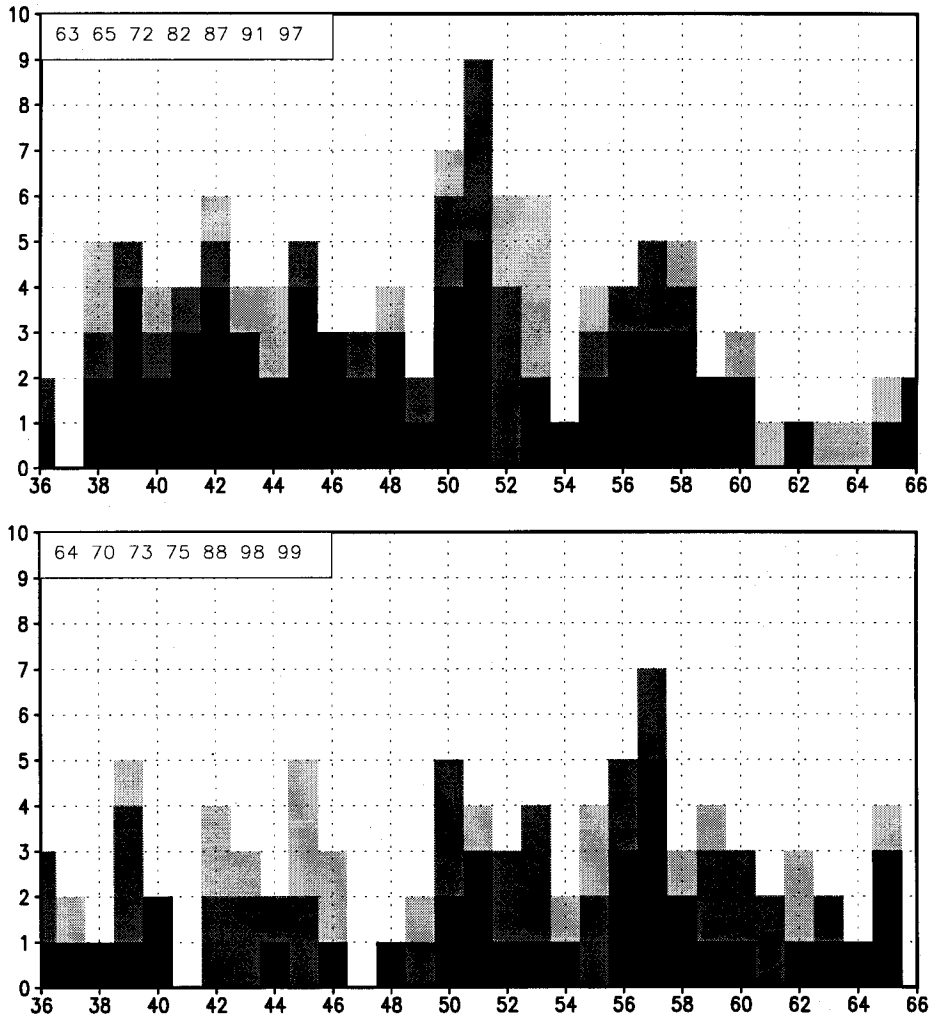

Figure 6.13: Same as Fig.6.12 but for 7 El Nino summers and 7 La Nina summer.

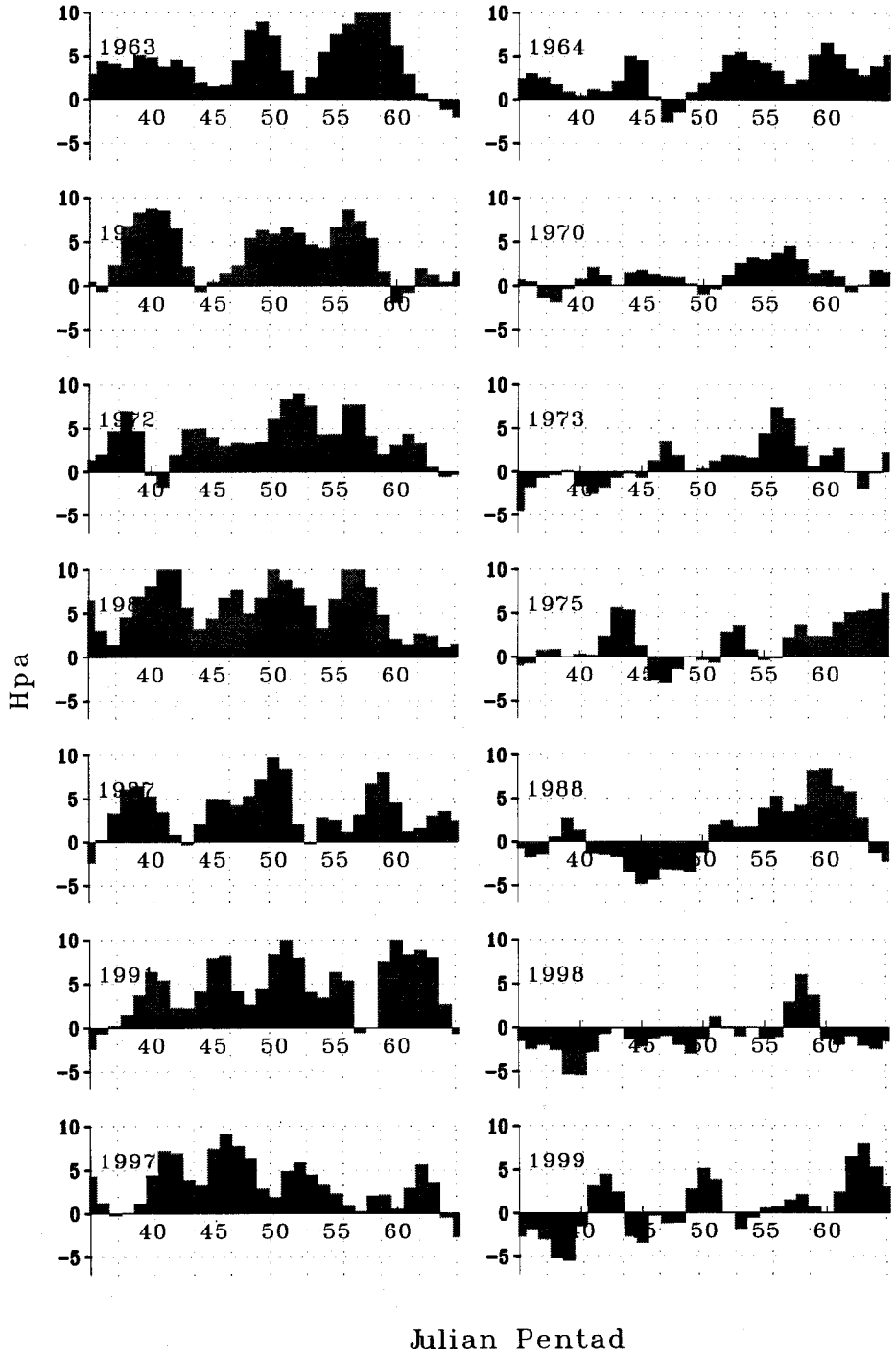

Figure 6.14: Domain averaged 850 hPa vorticity at 120° – 150°E, 10° – 20°N for 7 El Nino summers and La Nina summers.

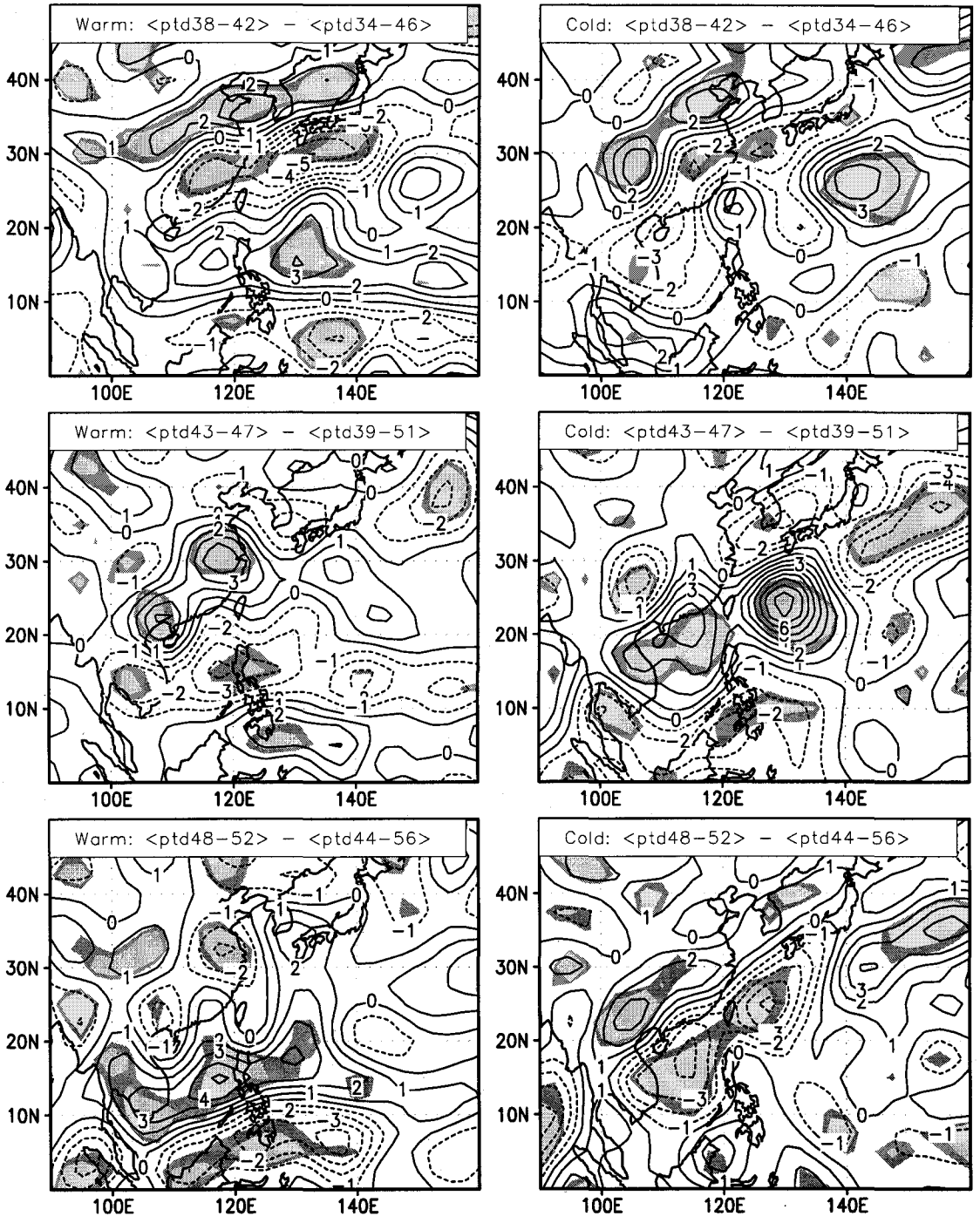

Figure 6.15: Composite of 850 hPa vorticity in three selected period, in 7 El Nino summers and 7 La Nina summers. Shading indicates T-test's 95% and 90% significance levels.

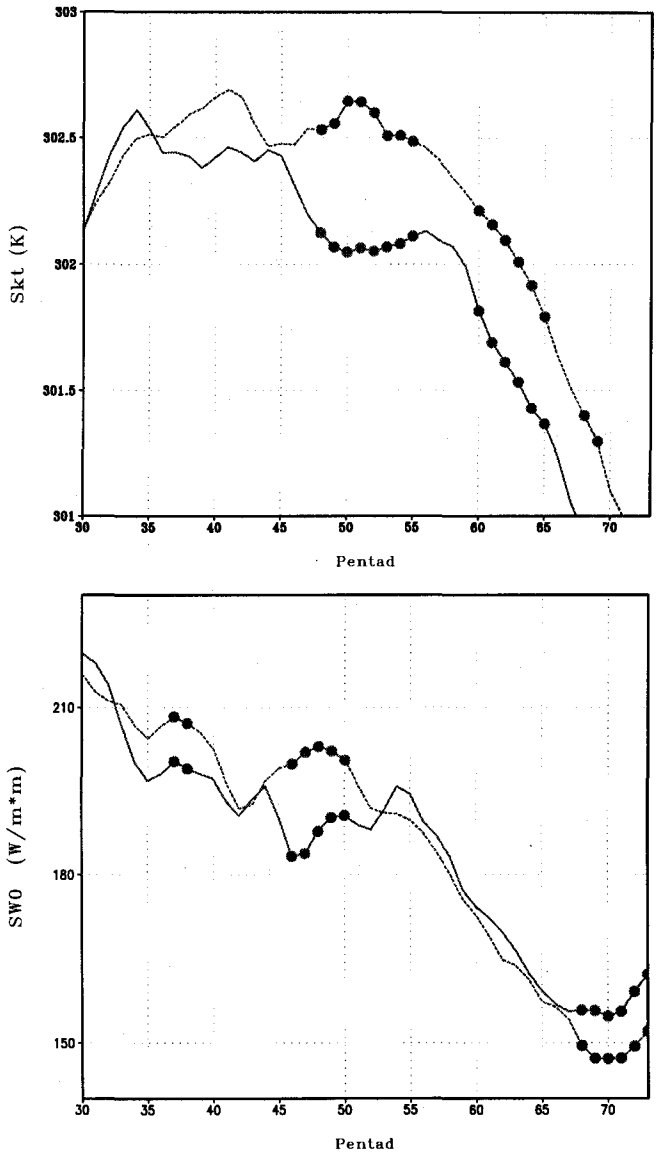

Figure 6.16: Composite of domain (120° – 150°E, 10° – 20°N) averaged NCEP skin temperature (upper panel) and surface total shortwave radiation (lower level) in 9 warm summers (82, 86, 87, 90, 91, 92, 93, 94, 97, with June-October Nino3,4 SST anomaly above zero) and 9 cold summers (83, 84, 85, 88, 89, 95, 96, 98, 99) from 1982-1999. Solid and dash lines represent the composites in warm and cold summers respectively. Dots denotes two-sample t-test's 95% significant level.

Chapter 7

Intraseasonal and Interannual Variations of the Indian Summer Monsoon

Previously, it has been shown that the interannual variations of the ISO in the Indian monsoon region are less pronounced compared with those in the WNP. Yet the ISO in the Indian monsoon region has more profound social and economical impacts. Therefore, its interannual variations are intensively investigated in this chapter.

7.1 Satellite-observed northward propagating ISO

The northward propagating ISO in the Indian summer monsoon region seems to be induced by Rossby wave emanation from the composite of OLR and the NCEP Reanalysis data (Kemball-Cook and Wang 2001). The strongest events occur in May-June associated with the Indian summer monsoon onset (their Fig.4): the intrasea-

sonal convective anomalies were initiated in the equatorial western Indian Ocean. After four days, they moved to 60°E-80°E. In another four days, the convection center moved to 80°E-100°E with the leading edge of the convection reaching the western coast of Sumatra. The envelope of the convection, which previously was symmetric about the equator tilted in a northwest-southeast direction: convection expanded from the equator northwestward to both the east and the west of the Indian Peninsular at about 10°N; Under anti-cyclonic circulation anomalies at 850 hPa, the region of 80°E-100°E,0°-10°S was also covered by negative OLR. Thereafter, the rainband moved northeastward. The tilted structure became more evident. It stretched from New Guinea all the way to the Arabian Sea. The Aug-Oct cases are weaker but they bear similar structure.

These observed features were explained by the equatorial wave theories (Matsuno 1966; Gill 1980; Wang and Xie 1996; Xie and Wang 1996). Due to the strong easterly-shear mean flow in the northern hemisphere, the Rossby response in the Indian summer monsoon region is much stronger than in the southern hemisphere. Therefore, the Rossby response in the southern hemisphere decays while those in the northern hemisphere are reinforced (Wang and Xie 1996; Xie and Wang 1996).

On the other hand, Wang and Rui (1990) has noticed that some northward propagation events, in which the convection follows a northward rather than northwestward path. The composite of the AGCM simulation (Jiang et al. 2003) also indicates a straight northward propagation from the equatorial Indian Ocean to the

northern Bay of Bengal. These cases cannot be explained by the northwestward Rossby wave emanation. Consequently, they caused a debate on the mechanism of the northward propagating ISO (Jiang et al. 2003; Drbohlav and Wang 2003).

The recent high-resolution TMI and QuikSCAT datasets provide an unprecedented clear picture with new details of the ISO's life cycle in the Indian summer monsoon region. In this section, the TMI SST, rainfall and QuikSCAT wind will be examined from 2000 to 2002. The NCEP Reanalysis data is also supplemented and compared with.

In order to identify the ISO events, the 20-50-day TMI rainfall is averaged at 75°E-100°E, 5°S-5°N in May-September (Fig. 7.1). Four cycles are found in each summer. The averaged period is about 33 days, with a standard deviation of 7 days. Because the period of each case varies, the composting strategy of using $t_0 + / - ndays$ (Kemball-Cook and Wang 2001; Jiang et al. 2003) is not used here. Instead, the composite was produced according to the phase at $-\pi$, $-3\pi/4$, $-\pi/2$, $-\pi/4$, 0, $\pi/4$, $\pi/2$, and $3\pi/4$ in the life cycle. Phase 0 and $\pi/2$ correspond to the initial stage and the peak phase of the ISO in the central-eastern Indian Ocean, respectively. The statistical significance of the composite fields was assessed by the student's t test similar as Wang and Xu (1997).

The spatio-temporal evolution of the rainfall anomaly from phase 0 to $3\pi/4$ is identical with that from phase $-\pi$ to $-\pi/4$, except that the positive and negative anomalies switch sign (Fig. 7.2). At phase $-\pi/4$, the positive rainfall anomalies first

appear at 60° – 70°E at the equator. Meanwhile, negative anomalies dominate the equatorial East Indian Ocean (EEIO). The negative anomalies tilt northwestward to 15°N west of the Indian Peninsular, and southwestward to 90°E, 10°N. Associated with the rainfall anomalies, there is easterly wind in the equatorial Indian Ocean and westerly in the northern Bay of Bengal.

At phase 0, the positive rainfall anomalies grow and move eastward to 70° – 85°E. The convective center is located between the equator and 5°S. The negative anomalies in the eastern Indian Ocean have weakened, and those in the Bay of Bengal have strengthened. Associated with the weakened subsidence in the eastern Indian Ocean, the easterly wind anomalies also decay in the EEIO.

At phase $\pi/4$, the positive anomalies take over the whole central-eastern Indian Ocean at 70° – 100°E, 5°S-5°N. The previous southeast-to-northwest oriented negative anomalies become zonally distributed at 15°N. The southern hemisphere negative anomalies have disappeared. The equatorial easterly winds have completely diminished. They are replaced by westerlies between 5°N and the equator. Associated with the subsidence at 15°N - 20°N, there are northeasterlies at these latitudes.

At phase $\pi/2$, the positive anomalies reach its peak phase in the central-eastern Indian Ocean. The negative anomalies west of the peninsular have disappeared, and those in the Bay of Bengal have also decayed. Both the equatorial westerlies and the northeasterlies in the off-equatorial region grow stronger.

At phase $3\pi/4$, the orientation of the positive anomalies in the EEIO is parallel

with the coastline of Sumatra. Positive anomalies also reach the western tip of the peninsular. Meanwhile, negative anomalies appear at $60° - 70°$E at the equator.

The northward propagation of the convection mostly occur from phase $\pi/2$ to phase $-\pi/2$. The major action takes place at from $\pi/2$ to $3\pi/4$. When the equatorial convection reaches the peak phase at $\pi/2$, it induces strong cyclonic circulation to its northwest. Meanwhile, the subsidence in the northern Bay of Bengal further enhances easterlies in the off-equatorial region. Due to the asymmetric summer mean flow, the anti-cyclonic circulation anomalies in the southern hemisphere are weaker. They can be found only between 80°E and 100°. A zonally-oriented trough is located at the southern Also due to the lifting of the mountains in the west coast of the peninsular, convection first occurs at the west coastal region of the peninsular at phase $3\pi/4$. In the southern hemisphere, convection persist to the west of the Sumatra coast. The overall convection band tilts in a southeast-northwest direction. From there, the convection to the west of the peninsular slowly decays, and that in the Bay of Bengal moves northeastward. The rainfall anomaly pattern at phase $3\pi/4$ strongly supports that the northward propagation of the ISO starts from Rossby wave emanation for equatorial convection.

The southeast-northwestward tilted rainband at phase $3\pi/4$ does not exist in the NCEP/NCAR precipitation. Similar as the above TMI rainfall index, the averaged precipitation rate is calculated using the Reanalysis data at the same domain. It reveals similar ISO cycles as the TMI rainfall. Thus, the same compositing scheme

can be applied on the NCEP/NCAR Reanalysis. The maps are displayed in Fig. 7.3. Displacement of the wet/dry anomalies generally agrees with the TMI rainfall composite, but the amplitudes are much weaker. Another salient difference is the complete missing of the tilted rainband structure. At phase $\pi/2$, the intraseasonal convection reaches the peak phase at 80°E-90°E. Thereafter, it moves northeastward to higher latitudes. Lack of intraseasonal variability in the EEIO is also indicated.

The surface wind composite from the NCEP/NCAR Reanalysis is similar with the QuikSCAT's at all the phases (Figure not shown). It implies the existence of system error in the model-produced precipitation rate in the Reanalysis. The AGCM simulation by Jiang et al. (2003) also lacks the tilted rainband structure, which gives rise to the question: Why the AGCMs tend to under-represent the Rossby wave emanation process? It is possibly one of the reasons for the lack of intraseasonal variability in the GCMs.

Difference in the summer mean rainfall (Fig.2.2) provides a clue. Besides that the Reanalysis overall underestimates the mean rainfall, it completely misses the the convection center located to the west of Sumatra coast. This convection center within 5 degree along the coastline can not be found in CMAP neither (figure not shown). The TMI mean rainfall shows that the southern convergence zone at 5°S is attached to the Sumatra coastal rainband, Both the CMAP and the Reanalysis have an isolated southern convection zone. The AGCM simulation (Jiang et al. 2003) can not reproduce both the southern convergence zone and the Sumatra coastal

rainband neither. Failures in the models and the CMAP are possibly caused by that their relatively low resolution, which can not capture the meso-scale convection along the coastline. Also, the model may not be able to simulate the orographic lifting of the mountains in West Sumatra. How the meso-scale convection can influence the large-scale convection/circulation also requires further numerical and theoretical understandings.

Fig. 7.4 shows the vertical structure of the ISO during the northward propagation. At phase $\pi/4$ (Fig. 7.4a), the p-velocity is more asymmetric about the equator than the rainfall. The center of the upward motion is located at 700-200 hPa between the equator and 10°S. Subsidence prevails the entire troposphere poleward of 10°N.

At phase $\pi/2$ (Fig. 7.4b), the vertical motion center splits to two patches. The southern hemisphere one lowers to 850-500 hPa and starts to decay. The northern center rises to 500-200 hPa and continues to grow. Meanwhile, the rainfall is enhanced and keeps symmetric about the equator.

By phase $3\pi/4$ (Fig. 7.4c), the upward-motion center between 10°N and 10°S has been completely separated into two: one at 10°S, and the other at 5°N. The subsidence in the northern hemisphere continues to decay. Rainfall at south of 5°N is weakened, but there is no significant asymmetry about the equator.

From phase $-\pi$ to $-\pi/2$, the upward-motion center grows and reaches 10°N, 15°N and 17°N, respectively. As it moves northward, its vertical structure becomes more barotropic. The latitudinal distribution of rainfall turns from symmetric about

the equator to a seesaw pattern: wet/dry condition coincides with the upward/downward motion.

The bifurcation from (a) to (c) reflects a Rossby wave response to tropical heating (Matsuno 1966). Once the large-scale intraseasonal convection arrives at the Sumatra coast, the orographic lifting enhances rainfall at the coastline, which further induces the off-equatorial circulation anomalies. As a result, the rainband at the equator eventually splits into two, with the northern one grows and the southern one decays (Wang and Xie 1996; Xie and Wang 1996).

During the northward propagation, divergence and specific humidity anomalies generally are in phase with the vertical motion: convective anomaly corresponds to lower-tropospheric convergence and positive specific humidity and upper-tropospheric divergence. The composite of Jiang et al. (2003) shows positive vorticity and specific humidity anomalies located to the north of the convective anomaly. They speculated that those anomalies can lead the convection move northward. Drbohlav and Wang (2003) proposed that there are upper-level divergence and lower-level convergence ahead of the convection center. The lower-level convergence further drives the convection to move northward. The phase relationships can not be confirmed here.

Kemball-Cook and Wang (2001) proposed that air-sea interaction plays an important role in the ISO's northward propagation. The subsidence to the north of the convection increases shortwave radiation, which further warms up the ocean surface. Consequently, low-level convergence and moist static energy are built up,

which destabilize the atmosphere and lead the equatorial convection to propagate northward. The air-sea interaction hypothesis is supported by the large intraseasonal SST variability (above 1°C) found by JASMINE (Joint Air-Sea Monsoon Interaction Experiment; Webster et al. 2002) and the TMI observation (Vecchi and Harrision 2001). Following the hypothesis, stronger northward propagating ISO was produced by coupling the GCM with an intermediate ocean model (Fu et al. 2003).

The TMI SST was composited at the same eight phases (Fig. 7.5). The 20-50-day SST variability center is located at 70°E-100°E, 5°S-5°N. The SST reached the maximum amplitude (about 0.3°C) at phase $-\pi/4$, 0, and the minimum at phase $-3\pi/4$ and $-\pi$. At all of the four phases, the SST anomaly center is sandwiched between the centers of the positive and negative precipitation anomalies. When the equatorial convection/subsidence is the strongest, the SST anomalies are very weak. The SST anomalies lag the emanation of Rossby wave and occurrence of the tilted rainband by about $\pi/4$. This result thus challenges the previous hypothesis that the poleward warmer SST leads the convection to move northward.

As a summary, the above satellite observations present high-resolution pictures of the northward propagating ISO in the Indian summer monsoon region. The northward propagation takes place in two steps: The first step ($\pi/2$-$3\pi/4$) is Rossby wave emanation process. As the eastward propagating ISO reaches the western boundary of the Maritime Continent, Rossby waves are emanated from the Kelvin-Rossby wave package, possibly due to the decrease of moist static energy in the Maritime Conti-

nent (Wang and Xie 1997). Consequently, the rainband, which was symmetric about the equator, tilts from the western coast of Sumatra to the western coast of Karala. The process takes about 4-8 days. Thereafter, the tilted rainband persistently moves northeastward to the inner land ($3\pi/4$- $-\pi/4$). This step is slower than the first step, taking about 20 days. The first step can be simply explained by the equatorial wave dynamics (Wang and Xie 1997). Most dynamics are involved in the second step, such as air-ocean-land interaction, interaction between the equatorial waves and the monsoon.

7.2 Interannual variations of the northward propagating ISO

7.2.1 The northward propagating ISO index

In the previous chapter, wavenumber-frequency analysis has been applied in the meridional direction to measure the intensity of the northward propagating ISO. Although the interannual variations of the northward propagating ISOs in both the WNP and the Indian summer monsoon region have similar amplitudes, the latter has a much weaker linkage with ENSO. In order to pursue the physical mechanism, an index to quantify the ISO intensity in each summer season is designed.

The 850 hPa zonal wind is chosen for the wavenumber-frequency analysis because the wind is more zonally homogenous in the Indian summer monsoon region

than other variables such as vorticity, vertical velocity or the precipitation rate. More importantly, the wind has a longer record than the OLR, and better quality than the precipitation rate of the Reanalysis.

The above satellite pictures reveal that the ISO does not follow a straight northward route. The rainband first tilts northwest-southeastward, then moves northeastward to the inner land. Although the tilted rainband structure is not obvious in the Reanalysis precipitation, the 850 hPa zonal wind anomaly of the Reanalysis does not propagate straight northward. Fig. 7.6 shows the composite for the ISO life cycle using the 850 hPa wind. There is a northwestward-tilted structure at phase $-\pi$ and 0. Overall, the wind anomalies propagate northeastward at the latitude domain of 10°S-25°N.

The northward propagating ISO index (NPII) is therefore defined as the spectrum density of 20-50-day northward propagating 850 hPa zonal wind averaged at 70°E-95°E. The latitude domain for the spatial decomposition is chosen as 10°S-25°N. The index for the period of 1948-2001 is shown in Fig. 7.7. Before the late 1960s, there are two cycles with a period of approximate 8 years. Thereafter, a 2-3-year periodicity dominates. This jump is probably caused by the improvement of the data quality in the early 1970s.

NPII can well represent the strength of the northward propagating ISO in the Indian summer monsoon region. As an example, *Hovmöller* diagrams were produced for eight years with the strongest northward propagating ISO (Fig. 7.8) and weakest

ones (Fig. 7.9). The two groups show sharp contrast: not only the amplitude is stronger, the northward propagation is better organized in all eight strong ISO years. Lack of connection between the equator and the higher latitudes is a common feature in the weak years. Besides, some southward-propagation events are also found in the weak years. Annamalai and Wang (2003) have also noticed that the weak ISO years are characterized by lower-tropospheric cyclonic vorticity locked at about 20°N, with few steady northward propagation from the equator.

Combined with the above composite satellite pictures, it is speculated that the weak ISO years are caused by lack of the step-1 processes. In Chapter 4, the interannual variations of the ISO total intensity have been displayed using CMAP, u_{850} and v_{850}. For all the three variables, the variability centers are located at 10°N-15°N. The interannual variability of the ISO is small north of 20°N. There is also a variability center located in the southern hemisphere between 5°S and 15°S. The northern and southern variability centers seem to correspond to the northern and southern variability centers of the Rossby wave response, respectively.

7.2.2 Sensitivity test

To ensure that the interannual variations revealed by NPII do not change dramatically with variables or small adjustment in the latitude domain, a series of sensitivity tests were carried out.

At the domain used for the definition of NPII, two indices were calculated

using OLR and the vertical p-velocity in the period of 1979-2001. The two indices both have significant correlation with NPII, with a correlation coefficient of 0.9 and 0.7, respectively.

The latitude domain has also been changed to 0°-22.5°N, 10°S-22.5°N, 10°S-25°N, respectively. The indices do not show significant changes with these modifications.

7.3 Mechanism for the interannual variations of the ISO: the mean state

Change in the summer mean state (circulation, convection and the boundary-layer condition) has been speculated to cause the interannual variations of the northward propagating ISO. In the following, the hypothesis is examined.

Composite difference in CMAP and winds at 850 hPa, 200 hPa levels are shown in Fig. 7.10 between 10 relatively strong and 13 relatively weak ISO years from 1979 to 2001. The criterion to separate the strong years from the weak ones is that NPII is above the long-term average. Only the recent 23 years are examined here because they have better data quality. Possible decadal change in the mean state can also be excluded.

The seasonal mean rainfall is significantly enhanced in the EEIO in the years with stronger northward propagating ISO. The positive anomaly region tilts north-

westward to southwest of the Indian Peninsular. This pattern is similar as the tilted-rainband structure at the step 1 of the northward propagation. Meanwhile, negative anomalies are found in the central Northeast India and the southwestern Indian Ocean.

At the 850 hPa level, there are cyclonic circulation anomalies to the northwest of the convection center in the EEIO. The equatorial westerly anomalies converge over EEIO just west of Sumatra. Easterly anomalies prevail at 15°N-20°N from IndoChina to the eastern Arabian Sea. The southern Indian Peninsular is located at a zonally-oriented trough, while the northern India is under a ridge. The 200 hPa wind anomalies are dominated by southly outflows from both the EEIO and the Maritime Continent.

The wind anomalies at both levels are linear responses to the anomalous heating in the EEIO. To test it, a numerical experiment was conducted with an anomalous moist baroclinic model (LBM) (Watanabe and Jin 2003), which is a linearized GCM. The horizontal resolution is 2.8° (T42 version), and 20 layers are chosen for the vertical. The May-Oct mean of the NCEP/NCAR Reanalysis is employed as the basic state. A stationary heating is prescribed at the ocean surface in the EEIO with the maximum amplitude of $2°C/day$. An e-folding timescale of 1 day is used for the horizontal diffusion. Linear drag which mimics Reyleigh friction and Newtonian damping is set to a scale of 1 day in the lower three levels, and 5, 15 , 30 days as the level increases.

Figure 7.11 shows the wind responses to the prescribed heating at 850 and 200 hPa in day 5. An anomalous cyclone is generated to the northwest of the heating at 850 hPa level. In the upper level, southly outflow is evident. Both the strength and the spatial pattern of the anomalies are similar with the observed composite, except that the 850 hPa trough is located slightly (about 5 deg) to the south of the observation.

Chapter 4 has shown that the EEIO has the largest interannual variations in May-October mean precipitation in the Indian summer monsoon region. Although tremendous attentions have been focused on the interannual variability of the Indian summer rainfall, the amplitude of its interannual variability is much smaller than in the EEIO.

The interannual variations of the ISO intensity are closely linked with the mean precipitation in the EEIO. The first SVD mode of the ISO intensity in the Indian summer monsoon region catches the interannual variability centers at 15°N and 10°S (Fig. 7.12). At a larger spatial domain, the interannual summer mean precipitation is still dominated by the variability in the EEIO. These two modes have a closely-related interannual variations. The correlation coefficient in the 23 years is 0.81. The percentage of the interannual variance that can be explained by the first SVD mode is shown in Fig. 7.13. Large percentage can be found in the EEIO, associated with the interannual variations in the seasonal mean precipitation. For the interannual ISO intensity, the percentage is lower. About 30% interannual ISO intensity in the

eastern Arabian Sea and 50% of that in southeastern Indian Ocean between 0° and 10°S can be explained by interannual change in the mean precipitation.

By using *Hovmöller* diagrams and POP analysis, Annamalai and Wang (2003) have separated the years with stationary ISO from those with an oscillating ISO. They also found the important role that the mean convection in the EEIO plays in the ISO's interannual variations. Besides, they emphasized the SST anomalies in the Indian Ocean, as well as ENSO conditions. The following subsections are devoted to clarify the relationship between the ISO and ENSO, the Indian Ocean dipole mode (IOD) as well as the mean vertical shear.

7.3.1 ENSO

NPII shows a negative correlation with the Nino3.4 SST anomaly. The 54-year correlation coefficient is -0.28, significant at the 95% confidence level. The scatter plot (Fig. 7.14b) also suggests a clear inverse relationship in most of the years except the years of 1988, 1950, 1970, 1984 and 1979.

Following the definition of NPII, the indices were calculated at other pressure levels. An inverse relationship can also be found at 700 and 925 hPa levels. Figure 7.14a,c show the scatter plots using the indices at 700 and 925 hPa. Their correlation coefficients with Nino3.4 SST are both -0.23, which is below the 95% confidence level. The relationship with the Nino3.4 SST become unclear at further higher levels.

ENSO modulates the northward propagating ISO in the Indian summer mon-

soon mainly through its influence on the mean circulation and precipitation in the EEIO. Figure 7.15 shows the composite difference between *La Niña* and *El Niño* summers, which have May-Sept Nino3.4 smaller and larger than 0, respectively. Both CMAP and 850 hPa circulation patterns resemble those displayed in Fig. 7.10. Besides, the amplitudes of the wind and CMAP are stronger east of 120°E in the ENSO composite maps. At the 200 hPa level, the amplitude of the ENSO composite is stronger than the in Fig. 7.10. Instead of southly, *La Niña* produces southwesterly anomalies in the EEIO.

7.3.2 Indian Ocean SST

Indonesian rainfall (including the surrounding ocean) is tightly coupled with ENSO, as well as the local SST (Hendon 2003). Besides ENSO, the interannual variability of the Indian Ocean SST may also contribute to EEIO mean precipitation and the ISO intensity.

Whether the interannual variability of the Indian Ocean SST is an independent mode from ENSO has gone through an intense debate. Webster et al (1999) and Saji et al. (1999) suggested a Indian Ocean dipole mode (IOD) which can be excited in the absence of remote forcing by ENSO. The strongest evidence for an independent IOD so far is that the IOD index (Saji et al. 1999) shows weak correlation with ENSO. But the construction of the index and correlation procedure that Saji et al. (1999) used are criticized (Allan et al. 2001) as the following: First, the EOF1 and EOF2

of the SST anomalies, although are orthogonal at zero lag, they show significant lag-correlations of about 9-10 months. Thus, EOF1 and EOF2 are not independent to each other; Second, the two nodes of the IOD are not significantly anti-correlated in time, thus it is inappropriate to define an IOD; Third, the correlation between the IOD index and Nino3 index becomes significant if focus on September-November mean values.

Stronger ISO in the Indian summer monsoon region is also linked with warmer SST in the Maritime Continent. Figure 7.16a shows the contrast in May-Sept SST between the stronger and weaker ISO years. SST is about 0.3°C-0.5°C warmer in the Maritime Continent. In the Indian Ocean, SST is 0.2°C warmer west of Sumatra coast, and 0.1°C-0.2°C cooler in the western and central Indian Ocean. But the contrast is not significant in most of the areas.

The lack of significant contrast in the EEIO SST between the strong and weak ISO years is probably due to the decoupling between SST and convection in some years. Figure 7.16b shows May-Sept CMAP and SST averaged at the domain of 90°E-105°E, 10°S-5°S, as marked in Fig. 7.16a. The two interannual variations are tightly related after 1989. But between 1983 and 1988, there exist some opposite-phase relationships. The correlation coefficient between SST and CMAP is 0.63 during 1979-2001. The CMAP is also inversely related to ENSO. Its correlation coefficient with the Nino3.4 SST is -0.50, significant at the 95% level. But the relationship between SST and Nino3.4 SST is not significant. The correlation coefficient is -0.22,

suggesting mechanisms other than ENSO in modulating the EEIO SST (Annamalai et al. 2003).

Stronger ISO season prefers warmer EEIO SST. The dominant SVD mode (Fig. 7.17) reveals the optimistic anomalous seasonal mean SST pattern for a stronger ISO summer. The indian Ocean is characterized by warm SST in the EEIO.

7.3.3 Mean vertical shear

The intermediate model (Wang and Xie 1996) suggests that easterly vertical shear ($u_{200} - u_{850}$) favors Rossby wave in the lower troposphere, while westerly shear favors Rossby wave in the upper troposphere. Based on the theory, the interannual variation of the ISO in the WNP is explained by ENSO-induced easterly shear. In the Indian summer monsoon region, the summer mean vertical shear is always easterly, and the interannual variations are too weak to change the sign of the mean shear. Consequently, the interannual variations of the ISO are much weaker compared with those in the WNP.

Jiang et al. (2003) used a simple 2.5-layer model and found the prevailing easterly shear over the Indian summer monsoon region generates barotropic vorticity to the north of convection and causes the northward propagation of the convection. The analytical solution of the model shows that the growth rate and phase speed of the northward propagating ISO mode are proportional to the squared vertical shear and the vertical shear, respectively. Based on their results, the interannual variations

in the mean shear still can cast a significant impact on the ISO, even if they are not strong enough to change the sign of the mean shear.

Before examining whether the mean vertical shear plays an important role in the interannual variation of the northward propagating ISO, its own interannual variations are first examined. Fig. 7.18b shows the 54-year standard deviation of $u_{850} - u_{200}$ vertical shear during 1948-2001. Compared with the long-term mean (Fig. 7.18a), the interannual variations of the vertical shear are very small between the equator and 20°N in the Indian Ocean. They only account for less than 10% of the mean vertical shear. The largest interannual variation of the shear is located in the western Indian Ocean between 10°S and 10°N. The interannual variations in the Bay of Bengal are the smallest in the entire Indian summer monsoon region. Because easterly and westerly shears have distinct different impacts on Rossby wave intensity and propagation, specific attentions are put on the regions that the climatological shear changes sign, which are the two narrow zones located at 10°S and 25°N (marked by shading in Fig. 7.18b).

Following similar compositing method, Fig. 7.19 shows the difference in the mean vertical wind shear between the strong ISO years and weak ones. There is no significant contrast between the two groups in the Indian summer monsoon region, suggesting that change in the mean shear is not an important factor in causing the interannual variations of the ISO in the Indian summer monsoon region.

7.4 Relationship with the Indian summer monsoon intensity

Although it is a wide consensus that active/break phase of the Indian summer monsoon (ISM) is directly caused by the passage of the ISO (Yasunari 1979, 1980), whether and how the strength of ISM is related to the ISO remains controversial. As has been reviewed earlier, the complexity partly arises from lack of quantitatively measurement of the ISO and understanding of its dynamics. On the other hand, finding an appropriate ISM index itself has been a contentious issue.

The All Indian Summer Rainfall index (AIRI) has long been used as a measure of the ISM, which is the seasonal averaged rainfall of all Indian meteorological subdivisions (Parthasarathy et al. 1992; Parthasarathy et al. 1995). To reflect large-scale circulation change associated with the ISM, Webster and Yang (1992) proposed a dynamic index (WYI) using the vertical shear of zonal wind between 850 hPa and 200 hPa at the equator-20°N, 40°E-110°E. Noticed that AIRI and WYI were poorly correlated, Goswami et al. (1999) developed a Monsoon Hadley Circulation Index (MHI) using the meridional wind shear between 850 hPa and 200 hPa ($v_{850} - v_{200}$) averaged at 10°N-30°N, 70°E-110°E. In order to better associate the monsoon convection with the circulation, Wang and Fan (1999) defined a convection index (averaged OLR at 10°N-25°N, 70°E-100°E) and a circulation index (westerly shear $u_{850} - u_{200}$ at 5°N-20°N, 40°E-80°E) to describe the interannual variations of the ISM as a convection-and-

circulation coupled system. Wang et al. (2001) improved the circulation index by using the difference of u_{850} averaged at two boxes: 5°N-15°N, 40°E-80°E and 20°N-30°N, 70°E-90°E. The Wang et al. (2001) index (WI) has a clearer physical meaning, which is the lower-tropospheric vorticity anomalies associated with the convection in the ISM region.

In this section, two parallel data sets are employed to quantify the interannual variations of the ISM. The first one is the Indian rain gauge records at 29 subdivisions in the period of 1948-2001. The second is the monsoon circulation index (Wang et al. 2001) With the newly defined ISO index, the ISO-ISM linkage is examined.

7.4.1 Indian rainfall

The correlation coefficients between rainfall at the 29 subdivisions and the ISO intensity during 1948-2001 is shown in Table 7.1. Only three subdivisions have their seasonal mean rainfall significantly correlated with the intensity of the northward propagating ISO. When the ISO is stronger, the southern tip of the peninsular receives more rainfall. Meanwhile to the north of Bangladesh (division 1), there is less rainfall.

To check whether there is a decadal change in the 1970's, the whole period is separated into two: 1979-2001 (Table 7.2) and 1948-1978 (Table 7.3). During the later epoch, the mean rainfall-ISO relationship agrees with the composite (Fig. 7.10): Subdivision 5, 14, 15 at between 20°N and 25°N have negative correlation with the ISO intensity. The southeastern tip of the peninsular (subdivision 24, 25)

have positive correlation with the ISO. In the early epoch, only subdivision28 shows significant positive correlation with the ISO.

ENSO has more pronounced direct impact on India seasonal mean rainfall. Table 7.4-6 show the correlation coefficients between Nino3.4 SST and the 29 subdivision rainfall in seasonal mean and individual month between May and September. Most subdivisions have negative correlation coefficients. The inverse relationship is more robust in the earlier epoch. After 1979, ENSO no longer seems to directly influence the mean rainfall in central India (subdivision 12, 13, 14, 15).

7.4.2 Monsoon circulation

On the interannual time scale, WI is highly correlated with AIRI with a correlation coefficient of 0.75 for 53 years (Fig. 7.21a). Yet both indices have insignificant correlation with the above-defined northward propagating ISO index.

The Wang et al. (2001) index can also describe the ISO, if the monthly or seasonal mean u_{850} is replaced by daily or pentad mean data. The time series contains the temporal evolution of the large-scale ISM cyclonic/anticyclonic circulation at intraseasonal, annual, and interannual time scales. The May-Sept standard deviation of the 20-50-day WI (WI_{iso}) measures the intraseasonal variability of the ISM in eash summer. WI_{iso} is highly correlated with the above-defined northward propagating ISO index (Fig. 7.21b).

7.5 Conclusion

In the Indian summer monsoon region, the life cycle of the northward-propagating ISO was revealed by QuikSCAT and TRMM satellite data. The composite scenario suggests that the intraseasonal convective anomalies are first generated in the equatorial Indian Ocean between 60°E-70°E, associated with the lower-level convergence and upper-level divergence at the monsoon break phase. The anomalies then propagate eastward and intensify at 70°E-100°E about 10 days later. Thereafter, the northward propagation takes place in two steps: At the first step, Rossby waves are emanated from the equatorial convection and propagate northwestward to 15°N, 70°-90°E in less than 10 days. There also forms a Rossby-wave response center in the southern hemisphere. During the second step, the southeast-northwestward titled rainband moves northeastward to the inner-land region and decay. The second step takes about 20 days.

In order to measure the seasonal activity of the northward-propagating ISO, an index was constructed from 1948 to 2001 based on the 20-50-day wavenumber-one northward propagating u850 anomalies averaged at 65°E-90°E. The weak-ISO years are characterized by isolated intraseasonal convection at the equator and 20°N, whereas the two regions are connected by the Rossby-wave-emanation process in the strong ISO years.

The seasonal activity of the northward-propagating ISO is found significantly influenced by the mean convection in the equatorial eastern Indian Ocean (EEIO),

which is the source of Rossby-wave emanation. ENSO modifies the northward-propagating ISO mainly by changing the mean convection in the EEIO. The ISO is significantly weaker in *El Niño* developing May-Sept, and stronger in the *La Niña* summer.

The seasonal activity of the northward-propagating ISO is not related to the overall performance of the Indian summer monsoon. Averaged rainfall at the 29 Indian subdivisions were examined from 1948 to 2001. During 1979-2001, two divisions in the southern Peninsular has positive correlation with the ISO intensity, and 4 divisions in the west central India and central Northeast India have negative correlation with the ISO intensity. This confirms the ISO-mean rainfall relationship revealed by CMAP rainfall. But neither the All Indian rainfall or the monsoon circulation index (Wang et al. 2001) has significant correlation with the seasonal activity of the northward propagating ISO.

Table 7.1 Correlation between the ISO index and May-Sept rainfall at 29 India subdivisions during 1948-2001.

Div	May-Sept	May	Jun	Jul	Aug	Sept
1	-0.26	0.00	-0.31	-0.08	-0.23	0.00
2	0.00	0.00	-0.11	0.04	-0.04	0.12
3	-0.14	0.07	-0.19	0.00	-0.28	0.03
4	0.01	0.07	-0.12	-0.01	-0.02	0.10
5	-0.13	0.11	0.05	-0.17	-0.08	-0.13
6	-0.06	-0.01	-0.05	-0.10	0.10	-0.07
7	-0.15	-0.01	0.00	0.03	-0.31	-0.11
8	-0.13	0.00	0.08	-0.05	-0.10	-0.22
9	-0.08	0.06	0.13	-0.05	-0.11	-0.06
10	-0.06	0.00	0.27	-0.15	0.06	-0.17
11	-0.01	-0.01	0.40	-0.08	-0.01	-0.08
12	0.20	0.04	0.42	-0.02	0.10	-0.01
13	0.14	0.25	0.00	0.12	0.09	0.00
14	-0.11	0.20	-0.20	0.16	-0.18	-0.05
15	-0.13	-0.10	0.04	-0.06	-0.15	-0.12
16	-0.07	0.02	-0.09	-0.05	-0.02	0.00
17	0.08	0.02	0.17	-0.02	0.13	-0.08
18	-0.18	0.00	-0.03	-0.05	-0.17	-0.09
19	0.01	-0.02	0.03	-0.08	-0.13	0.16
20	0.07	-0.08	-0.03	0.10	-0.07	0.18
21	0.00	0.04	0.00	-0.16	0.04	0.09
22	0.14	-0.03	0.37	-0.08	0.03	0.10
23	-0.01	0.00	0.19	-0.18	0.04	0.01
24	0.24	0.05	0.34	0.18	-0.08	0.08
25	0.42	-0.04	0.45	0.08	0.03	0.42
26	0.00	-0.01	0.12	0.02	-0.15	0.01
27	0.02	-0.06	0.25	-0.13	-0.19	0.19
28	0.40	-0.04	0.23	0.00	0.27	0.38
29	0.08	-0.06	0.09	-0.04	0.00	0.24

Table 7.2 Same as Table 1 but for the period of 1979-2001.

Div	May-Sept	May	Jun	Jul	Aug	Sept
1	-0.30	0.04	-0.40	-0.10	-0.22	-0.13
2	0.01	-0.02	-0.17	0.04	0.00	0.20
3	-0.10	0.09	-0.27	0.01	-0.17	-0.03
4	-0.10	0.10	-0.27	-0.14	-0.13	0.15
5	-0.47	0.10	-0.09	-0.31	-0.26	-0.42
6	-0.28	-0.09	-0.28	-0.18	0.00	-0.03
7	-0.16	-0.13	0.01	-0.01	-0.25	-0.07
8	-0.31	-0.20	0.04	-0.23	-0.09	-0.32
9	-0.06	-0.07	0.12	-0.22	0.03	0.00
10	-0.14	-0.08	0.41	-0.35	0.02	-0.10
11	-0.25	-0.18	0.61	-0.34	-0.16	-0.14
12	0.12	-0.01	0.48	-0.13	0.02	-0.06
13	0.09	0.10	-0.13	0.29	0.00	-0.04
14	-0.51	0.18	-0.42	0.16	-0.45	-0.22
15	-0.54	-0.26	-0.14	-0.24	-0.40	-0.35
16	-0.32	-0.02	-0.20	-0.14	-0.19	-0.18
17	0.00	0.00	0.16	-0.11	0.16	-0.36
18	-0.38	-0.03	-0.19	-0.05	-0.35	-0.17
19	-0.01	-0.12	-0.02	-0.02	-0.15	0.14
20	0.07	-0.18	-0.11	0.21	-0.05	0.14
21	-0.20	-0.02	-0.12	-0.28	-0.06	-0.05
22	0.26	0.03	0.46	-0.02	0.13	0.05
23	-0.04	0.00	0.21	-0.19	0.00	-0.02
24	0.43	0.09	0.57	0.10	0.13	0.09
25	0.53	-0.05	0.57	-0.11	0.31	0.53
26	-0.34	-0.10	0.06	-0.07	-0.45	0.00
27	0.02	0.00	0.05	-0.43	-0.07	0.32
28	0.27	-0.11	0.05	-0.27	0.40	0.47
29	-0.11	-0.14	0.02	-0.23	-0.04	0.16

Table 7.3 Same as Table 1 but for the period of 1948-1978.

Div	May-Sept	May	Jun	Jul	Aug	Sept
1	-0.21	-0.03	-0.20	-0.06	-0.26	0.11
2	-0.01	0.05	-0.09	0.04	-0.10	0.02
3	-0.23	0.04	-0.07	-0.01	-0.45	0.14
4	0.16	0.01	0.03	0.12	0.12	0.05
5	0.34	0.14	0.25	0.02	0.22	0.18
6	0.18	0.07	0.31	0.00	0.25	-0.11
7	-0.16	0.14	0.00	0.10	-0.41	-0.17
8	0.07	0.23	0.13	0.18	-0.10	-0.12
9	-0.09	0.29	0.15	0.12	-0.30	-0.12
10	0.05	0.16	0.09	0.09	0.12	-0.25
11	0.26	0.22	0.11	0.44	0.15	-0.03
12	0.29	0.17	0.30	0.08	0.19	0.04
13	0.23	0.47	0.15	0.01	0.23	0.04
14	0.30	0.22	0.02	0.20	0.14	0.14
15	0.34	0.05	0.29	0.15	0.22	0.18
16	0.20	0.09	0.09	0.01	0.17	0.18
17	0.18	0.20	0.20	0.04	0.08	0.21
18	0.00	0.05	0.10	-0.03	-0.03	-0.01
19	0.04	0.06	0.11	-0.13	-0.11	0.18
20	0.08	0.06	0.06	-0.03	-0.10	0.23
21	0.26	0.14	0.11	-0.05	0.17	0.28
22	-0.01	-0.15	0.24	-0.17	-0.09	0.17
23	0.04	-0.01	0.17	-0.16	0.08	0.07
24	-0.05	0.03	-0.09	0.32	-0.38	0.07
25	0.26	-0.01	0.19	0.31	-0.20	0.32
26	0.21	0.08	0.18	0.13	0.12	0.03
27	0.05	-0.13	0.53	0.07	-0.32	0.05
28	0.58	0.02	0.49	0.32	0.10	0.36
29	0.25	0.00	0.16	0.11	0.02	0.35

Table 7.4 Same as Table 1 but for correlation with Nino3.4 SST.

Div	May-Sept	May	Jun	Jul	Aug	Sept
1	-0.07	-0.09	0.09	-0.03	-0.20	0.18
2	-0.17	-0.08	-0.03	-0.14	-0.22	0.30
3	-0.15	-0.13	-0.14	-0.13	0.04	-0.05
4	-0.14	-0.12	-0.14	0.10	0.17	-0.28
5	0.01	-0.02	-0.12	0.21	0.16	-0.22
6	-0.07	0.03	-0.10	0.03	0.14	-0.12
7	-0.10	-0.10	-0.22	-0.06	0.15	0.00
8	-0.36	0.19	-0.35	-0.21	-0.23	0.00
9	-0.32	0.32	-0.33	-0.23	-0.16	-0.15
10	-0.35	0.26	-0.10	-0.26	-0.06	-0.40
11	-0.54	0.30	-0.16	-0.26	-0.15	-0.50
12	-0.21	0.22	0.02	-0.21	-0.11	-0.33
13	-0.35	0.11	-0.03	-0.30	-0.01	-0.50
14	-0.28	0.00	-0.16	-0.16	0.07	-0.43
15	-0.11	0.20	-0.15	-0.02	0.00	-0.20
16	-0.23	-0.01	0.18	-0.23	-0.04	-0.51
17	-0.25	-0.12	0.09	-0.24	-0.17	-0.29
18	-0.23	-0.13	-0.10	-0.10	0.00	-0.46
19	-0.34	0.00	0.07	-0.16	0.06	-0.47
20	-0.44	0.01	-0.13	-0.17	-0.17	-0.39
21	-0.31	0.00	-0.21	-0.24	-0.05	-0.36
22	-0.33	0.04	-0.08	-0.22	-0.18	-0.15
23	-0.41	0.13	-0.12	-0.21	-0.25	-0.31
24	-0.29	-0.10	0.25	-0.41	-0.21	-0.02
25	-0.32	0.02	0.19	-0.32	-0.23	-0.01
26	-0.35	-0.17	-0.27	-0.01	-0.03	-0.49
27	-0.34	0.00	0.07	-0.15	-0.15	-0.26
28	-0.32	0.02	0.33	-0.30	-0.35	-0.10
29	-0.19	-0.08	-0.01	0.15	-0.10	-0.36

Table 7.5 Same as Table 2 but for correlation with Nino3.4 SST.

Div	May-Sept	May	Jun	Jul	Aug	Sept
1	-0.14	-0.34	0.27	-0.23	-0.45	0.29
2	-0.21	-0.23	0.07	-0.15	-0.41	0.49
3	-0.06	-0.21	0.18	-0.16	-0.16	-0.04
4	-0.10	-0.34	-0.37	0.24	0.33	-0.15
5	0.05	-0.12	-0.20	0.27	0.44	-0.32
6	0.03	-0.03	-0.12	-0.02	0.39	-0.12
7	-0.08	-0.31	-0.17	-0.11	0.06	-0.07
8	-0.29	0.20	-0.29	-0.25	-0.31	0.05
9	-0.41	0.43	-0.35	-0.32	-0.26	-0.26
10	-0.41	0.32	-0.22	-0.46	-0.03	-0.49
11	-0.45	0.40	-0.19	-0.37	0.15	-0.56
12	0.07	0.26	0.02	-0.16	0.08	-0.14
13	-0.04	0.24	0.07	-0.30	0.25	-0.36
14	0.03	-0.13	-0.04	0.07	0.26	-0.33
15	0.13	0.25	-0.14	0.25	0.25	-0.19
16	0.02	-0.02	0.36	-0.36	0.19	-0.30
17	-0.25	-0.26	0.13	-0.34	-0.12	-0.03
18	-0.07	-0.19	-0.11	-0.20	0.24	-0.36
19	-0.24	0.08	0.19	-0.38	0.17	-0.40
20	-0.47	0.07	-0.17	-0.27	-0.29	-0.37
21	-0.27	-0.10	-0.19	-0.25	0.02	-0.31
22	-0.36	-0.03	-0.07	-0.39	-0.26	0.08
23	-0.43	0.10	-0.21	-0.35	-0.19	-0.20
24	-0.31	-0.11	0.16	-0.45	-0.35	0.18
25	-0.46	0.11	0.13	-0.45	-0.46	-0.19
26	-0.05	-0.14	-0.41	0.19	0.35	-0.48
27	-0.23	0.12	0.21	-0.13	-0.08	-0.26
28	-0.30	0.15	0.53	-0.46	-0.34	-0.18
29	0.00	-0.15	0.01	0.21	0.25	-0.30

Table 7.6 Same as Table 3 but for correlation with Nino3.4 SST.

Div	May-Sept	May	Jun	Jul	Aug	Sept
1	0.09	0.40	-0.01	0.11	0.04	-0.06
2	-0.08	0.03	0.09	-0.14	0.02	0.03
3	-0.38	0.00	-0.48	-0.10	0.30	-0.17
4	-0.30	-0.16	0.02	-0.06	0.02	-0.38
5	-0.07	-0.06	-0.15	0.15	-0.22	-0.07
6	-0.17	-0.08	-0.22	0.11	-0.07	-0.04
7	-0.25	-0.13	-0.33	-0.08	0.28	0.05
8	-0.49	0.05	-0.53	-0.17	-0.13	-0.15
9	-0.17	0.02	-0.39	-0.14	-0.04	0.00
10	-0.25	-0.02	-0.19	-0.05	-0.06	-0.30
11	-0.61	0.09	-0.21	-0.11	-0.40	-0.45
12	-0.54	-0.20	-0.02	-0.30	-0.25	-0.43
13	-0.57	-0.19	-0.22	-0.29	-0.28	-0.56
14	-0.50	0.06	-0.35	-0.31	-0.12	-0.46
15	-0.32	0.10	-0.24	-0.28	-0.29	-0.19
16	-0.46	-0.12	-0.20	-0.12	-0.26	-0.61
17	-0.24	0.08	-0.07	-0.17	-0.23	-0.46
18	-0.33	-0.03	-0.10	0.04	-0.18	-0.56
19	-0.42	0.07	-0.19	0.03	-0.04	-0.60
20	-0.41	-0.01	-0.12	-0.01	-0.07	-0.48
21	-0.35	0.09	-0.33	-0.22	-0.13	-0.34
22	-0.34	0.09	-0.08	-0.02	-0.12	-0.41
23	-0.34	0.19	-0.05	-0.03	-0.31	-0.33
24	-0.27	-0.02	0.45	-0.35	-0.06	-0.20
25	-0.11	0.04	0.29	-0.21	-0.05	0.04
26	-0.55	-0.07	-0.30	-0.14	-0.37	-0.46
27	-0.39	0.00	-0.18	-0.12	-0.20	-0.25
28	-0.33	0.15	0.01	-0.13	-0.39	-0.14
29	-0.28	0.14	-0.11	0.20	-0.39	-0.44

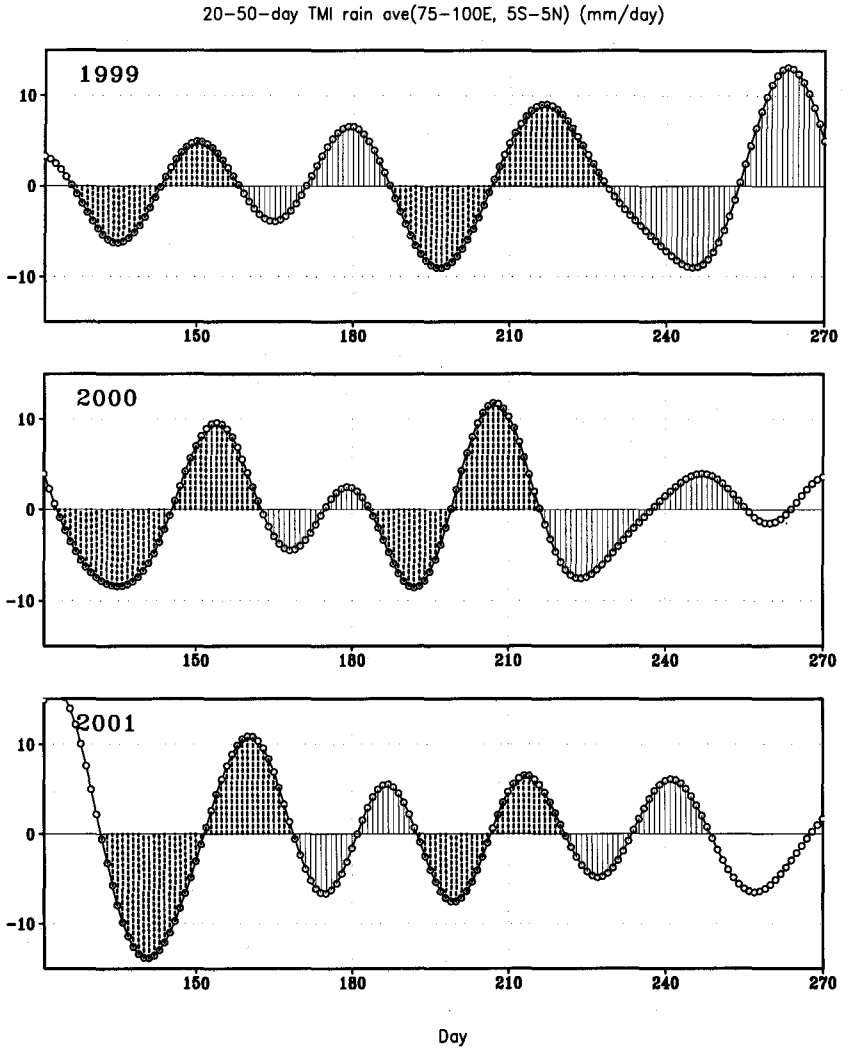

Figure 7.1: Domain averaged 20-50-day TMI rainfall (mm/day) at 75E-100E,5S-5N in May-September, 1999, 2000 and 2001.

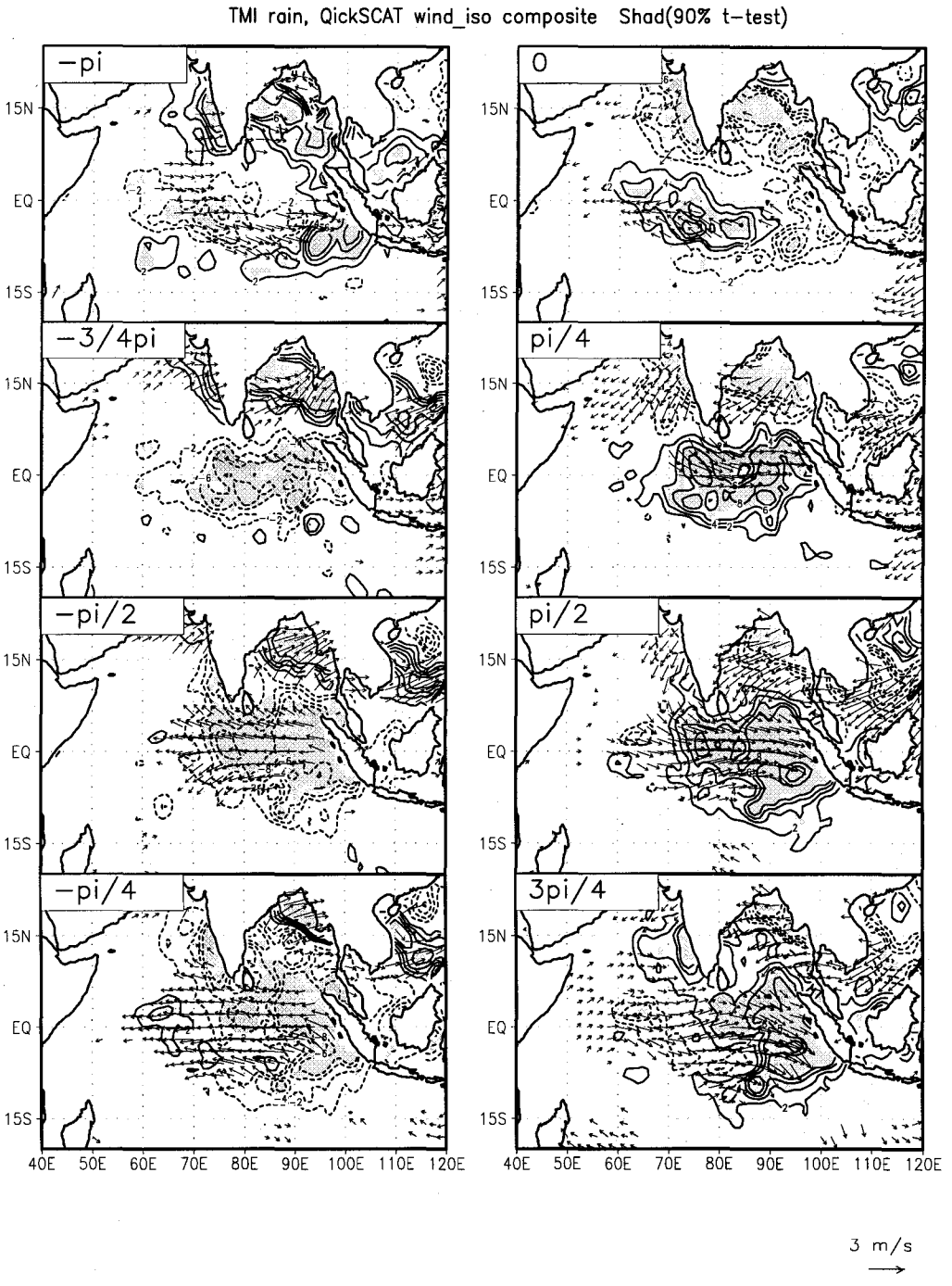

Figure 7.2: The contours are the composite of TMI 20-50-day rainfall (mm/day) at from phase $-\pi$ to $3\pi/4$. Shading indicates the 90% confidence level. The vectors are the composite of QuikSCAT wind. Only those are significant at the 90% level are drawn.

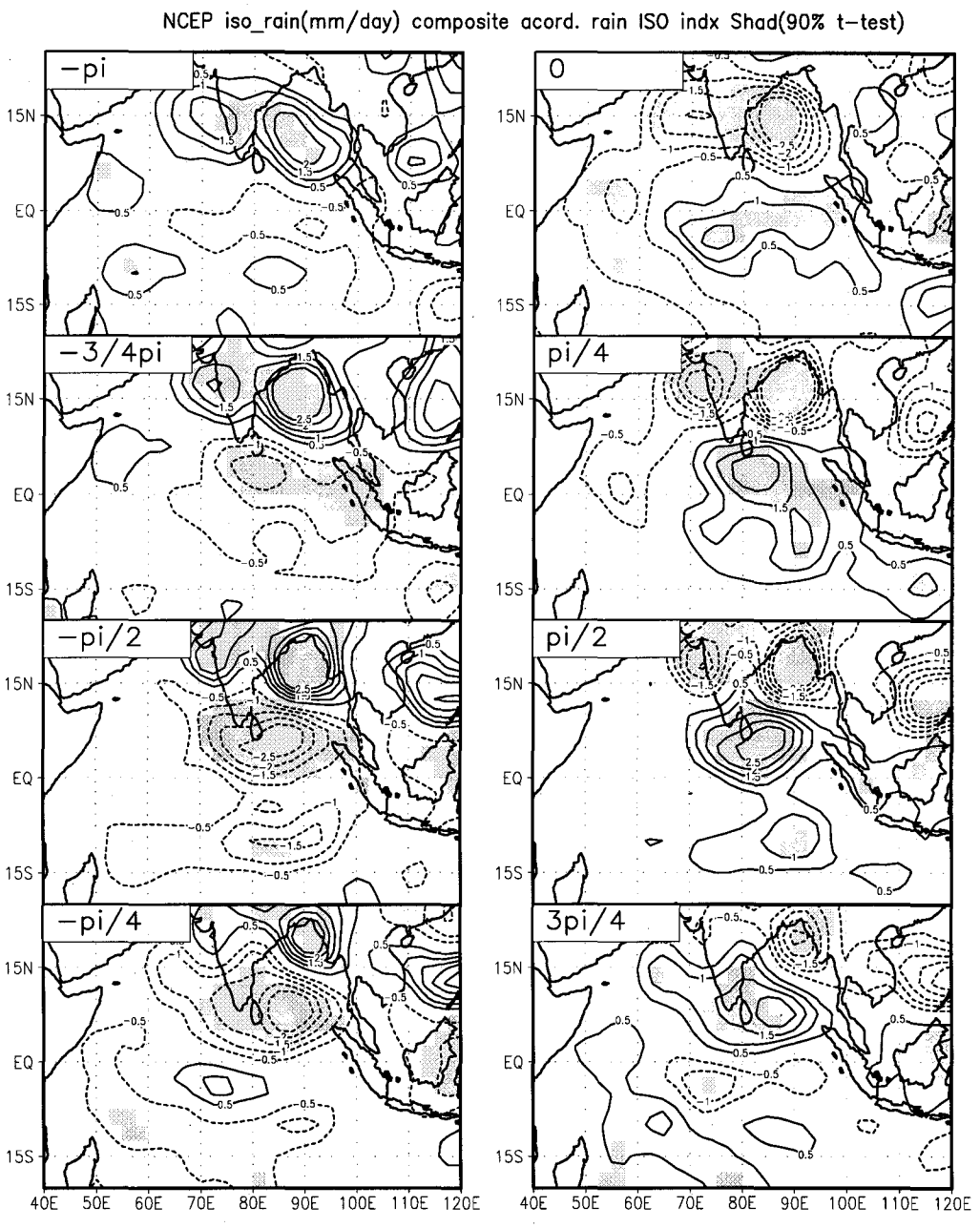

Figure 7.3: Composite of the NCEP Reanalysis precipitation rate (mm/day) at the 8 phases.

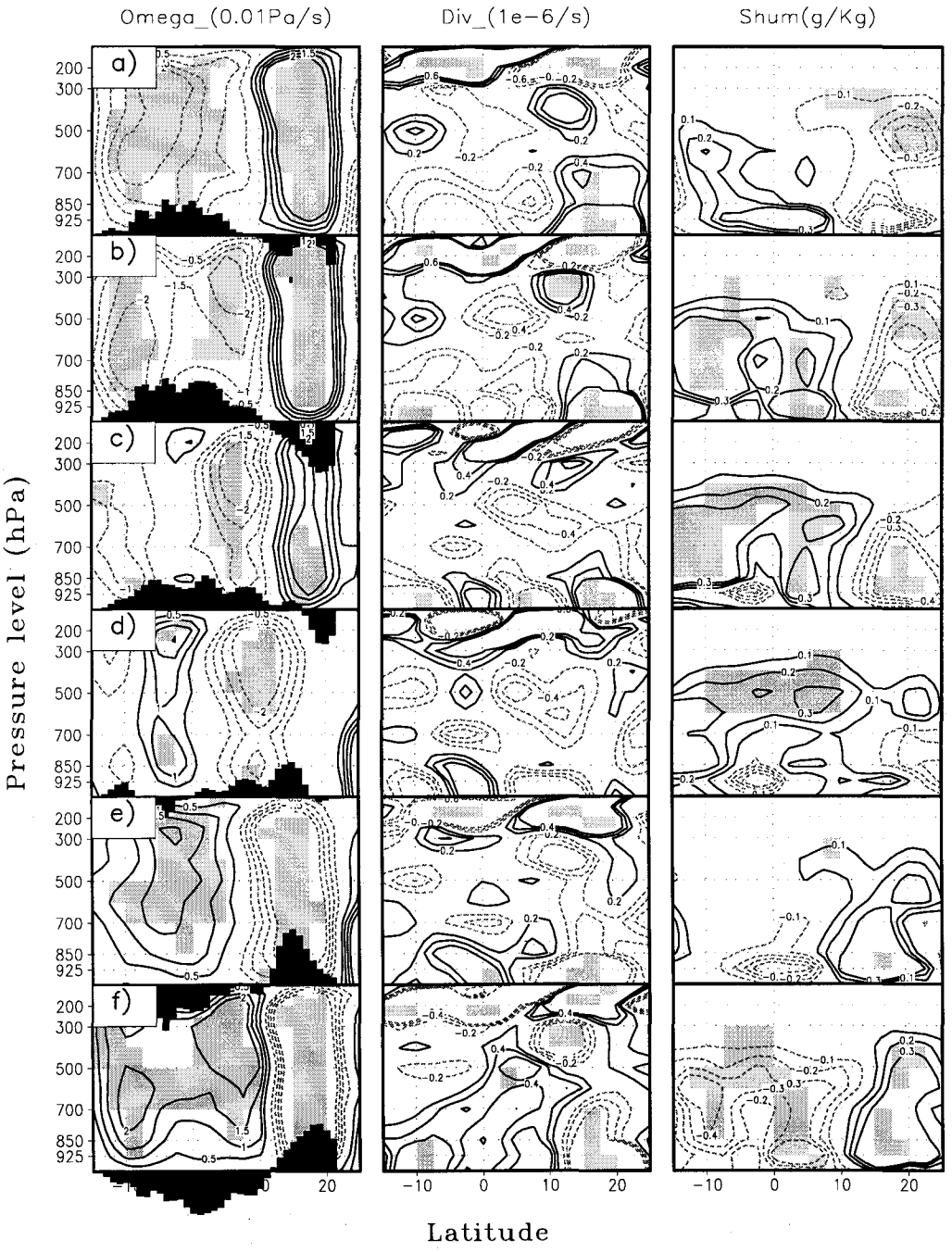

Figure 7.4: Vertical crosssection at 90°E at phase (a) $\pi/4$, (b) $\pi/2$, (c) $3\pi/4$, (d) $-\pi$, (e) $-3\pi/4$, and (f) $-\pi/4$. The three colums are vertical velocity (Pa/s), divergence (s^{-1}), and specific humidity (g/kg). The black shading is the TMI rainfall anomaly at 90°E, which indicates the latitude of the maximum convection center. Yellow shading indicates the 90% confidence level.

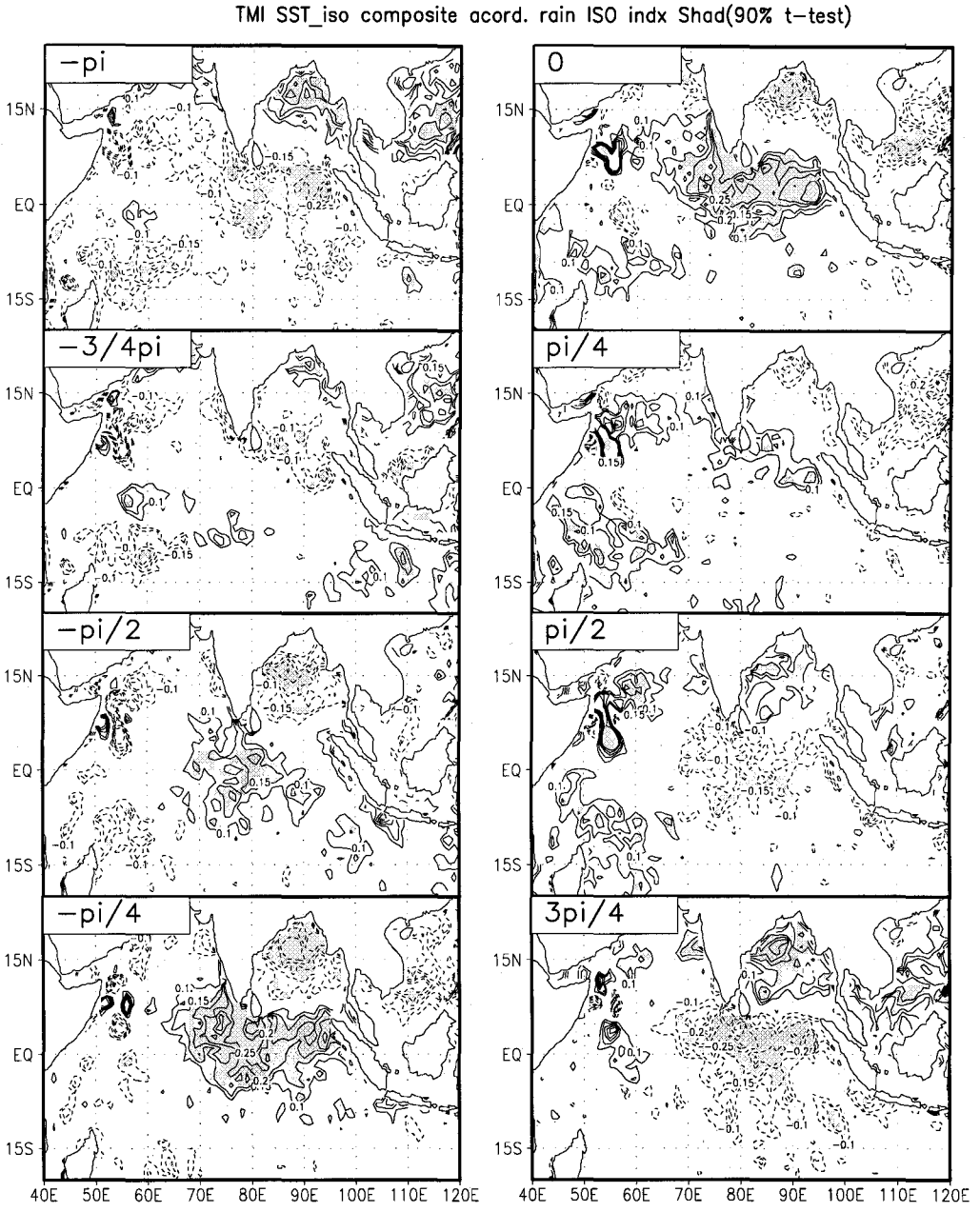

Figure 7.5: Same as Fig. 7.2 but for TMI SST.

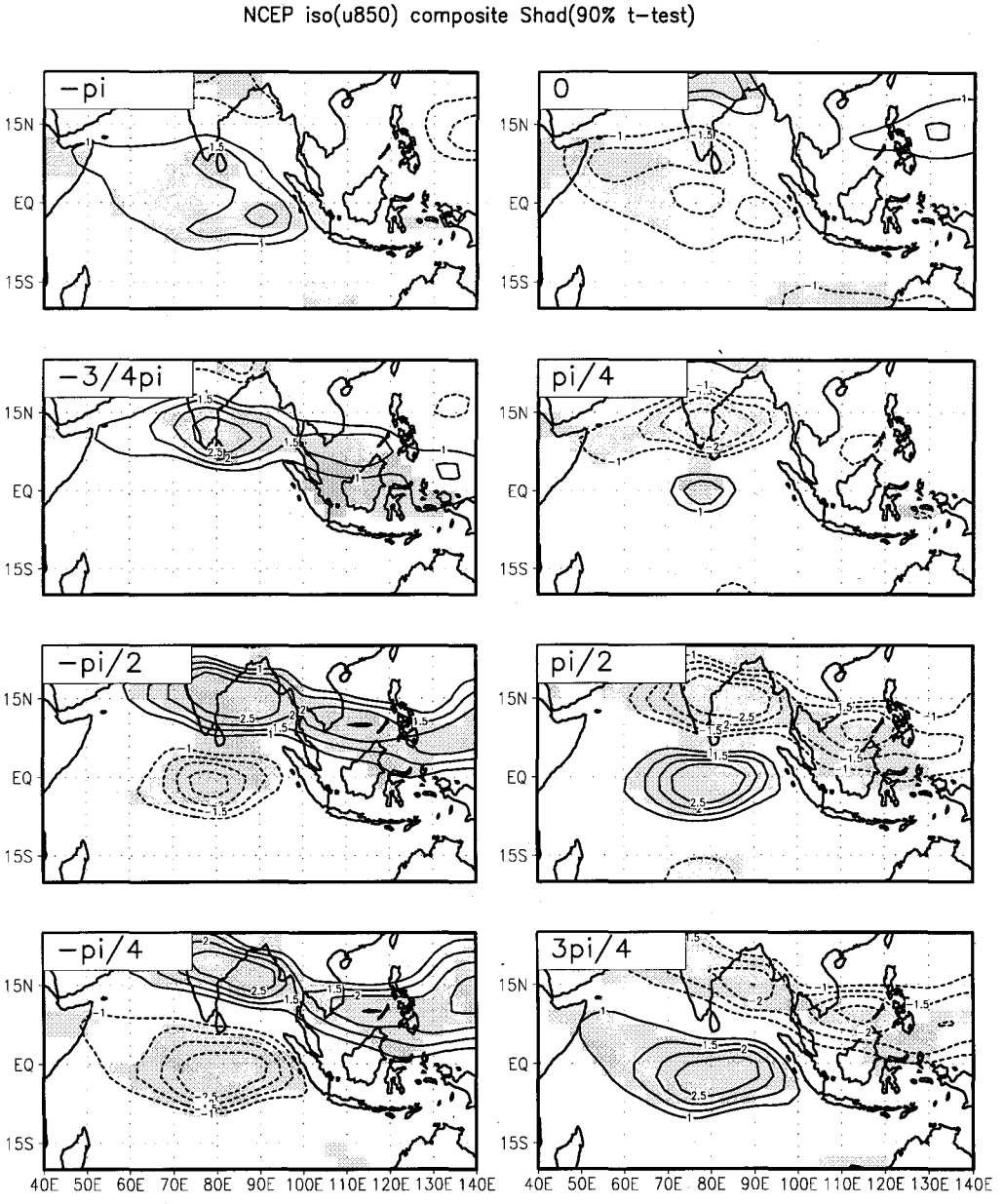

Figure 7.6: Same as Fig. 7.5 but for 850 hPa zonal wind of the Reanalysis dataset.

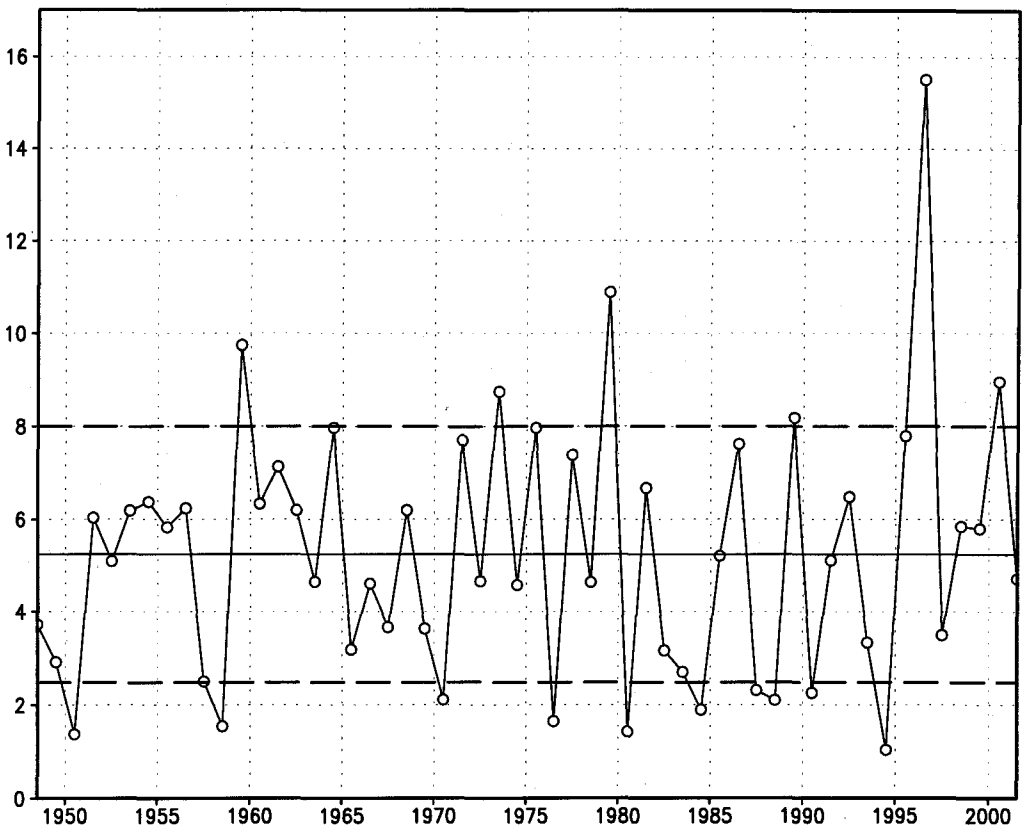

Figure 7.7: The northward propagating ISO index from 1948 to 2001.

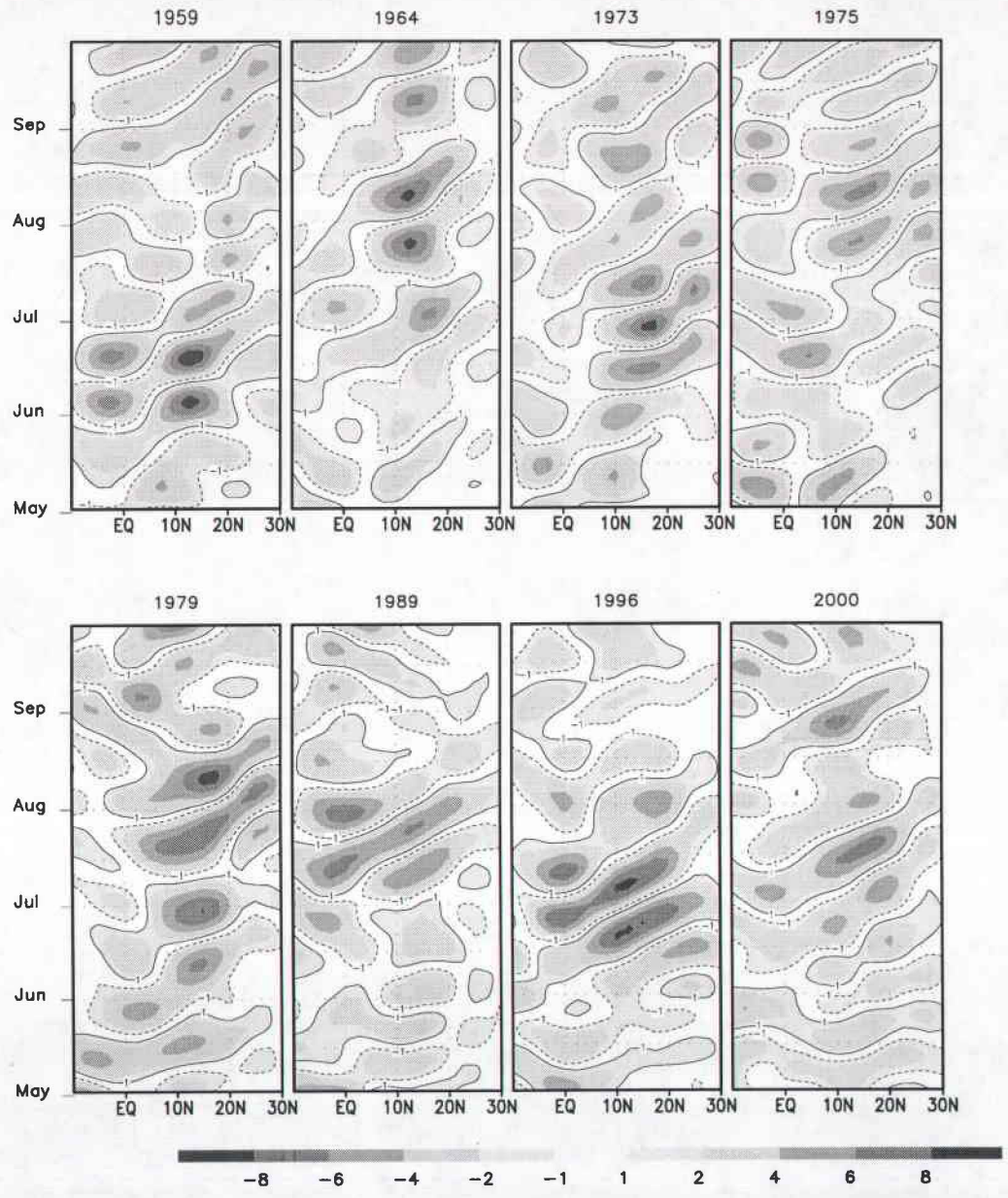

Figure 7.8: Hovemuller diagram of 8 selected years with the strongest northward propagating ISO.

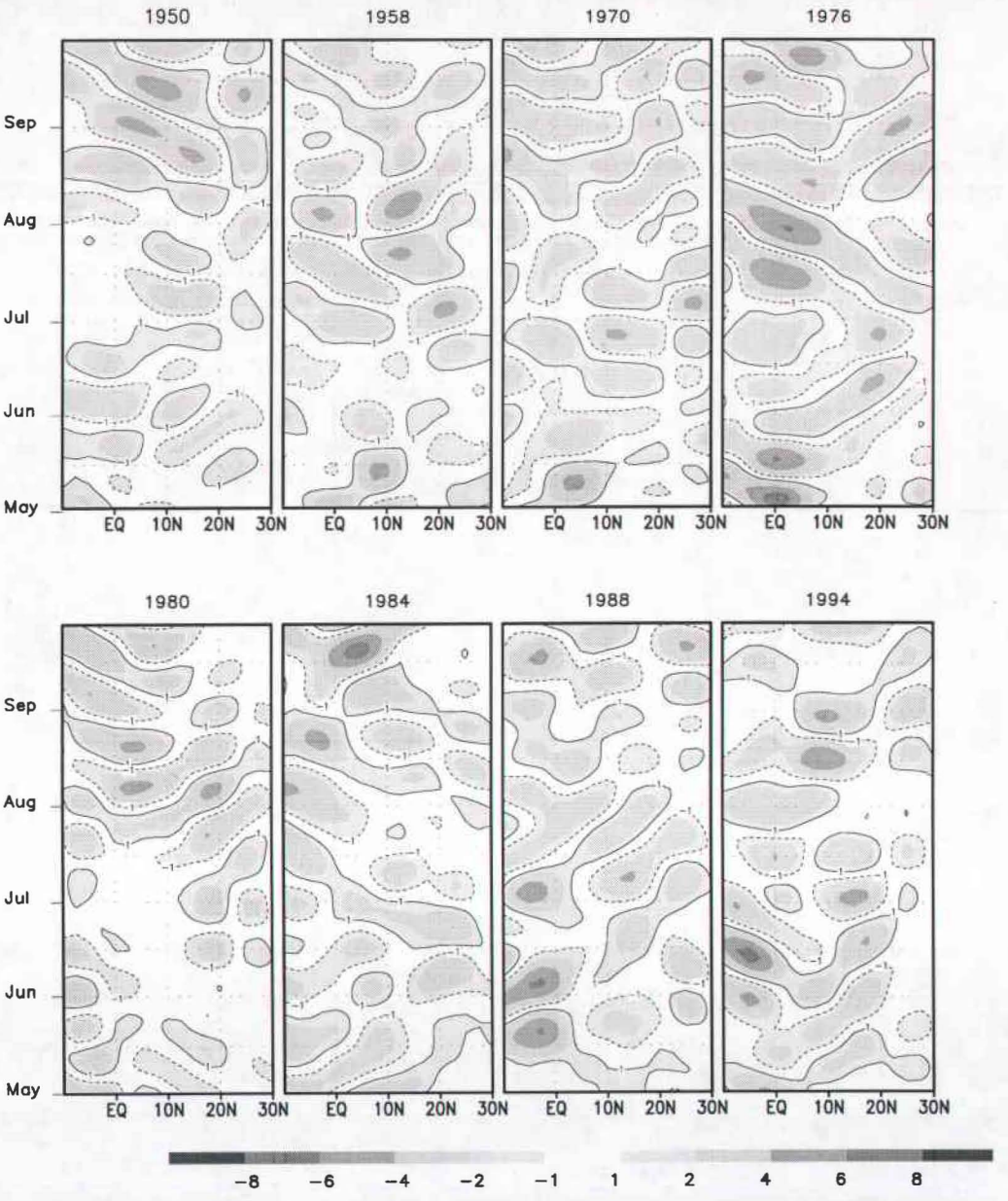

Figure 7.9: Same as Fig. 7.8 but for the years with the weakest ISO.

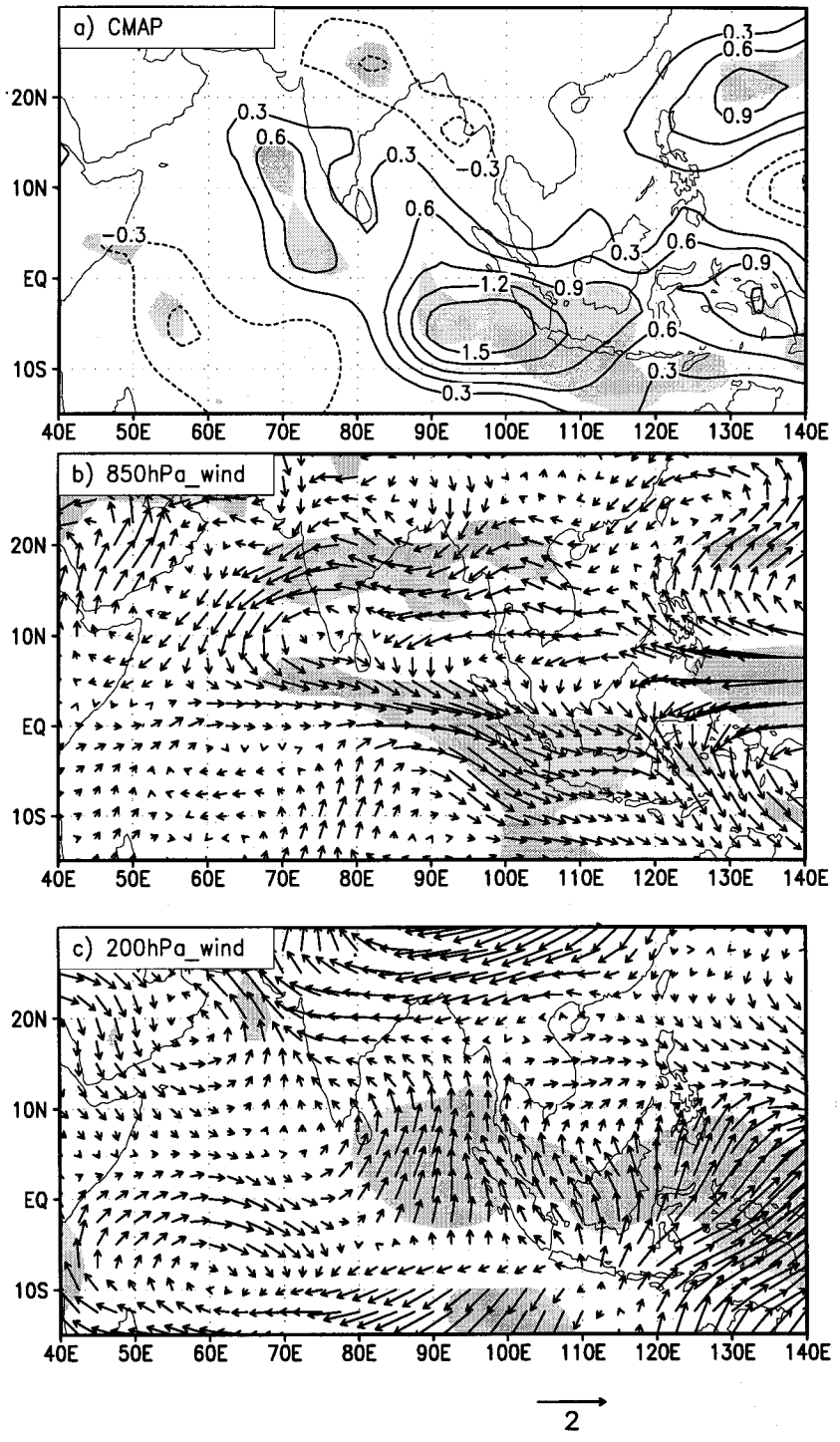

Figure 7.10: Difference of May-Sept mean in (a) CMAP, (b) NCEP 850 hPa and (c) 200 hPa wind between 10 years with the ISO index > 0 and 13 years with the ISO index < 0. Shading indicate the 90% confidence level using two-sample student's t-test.

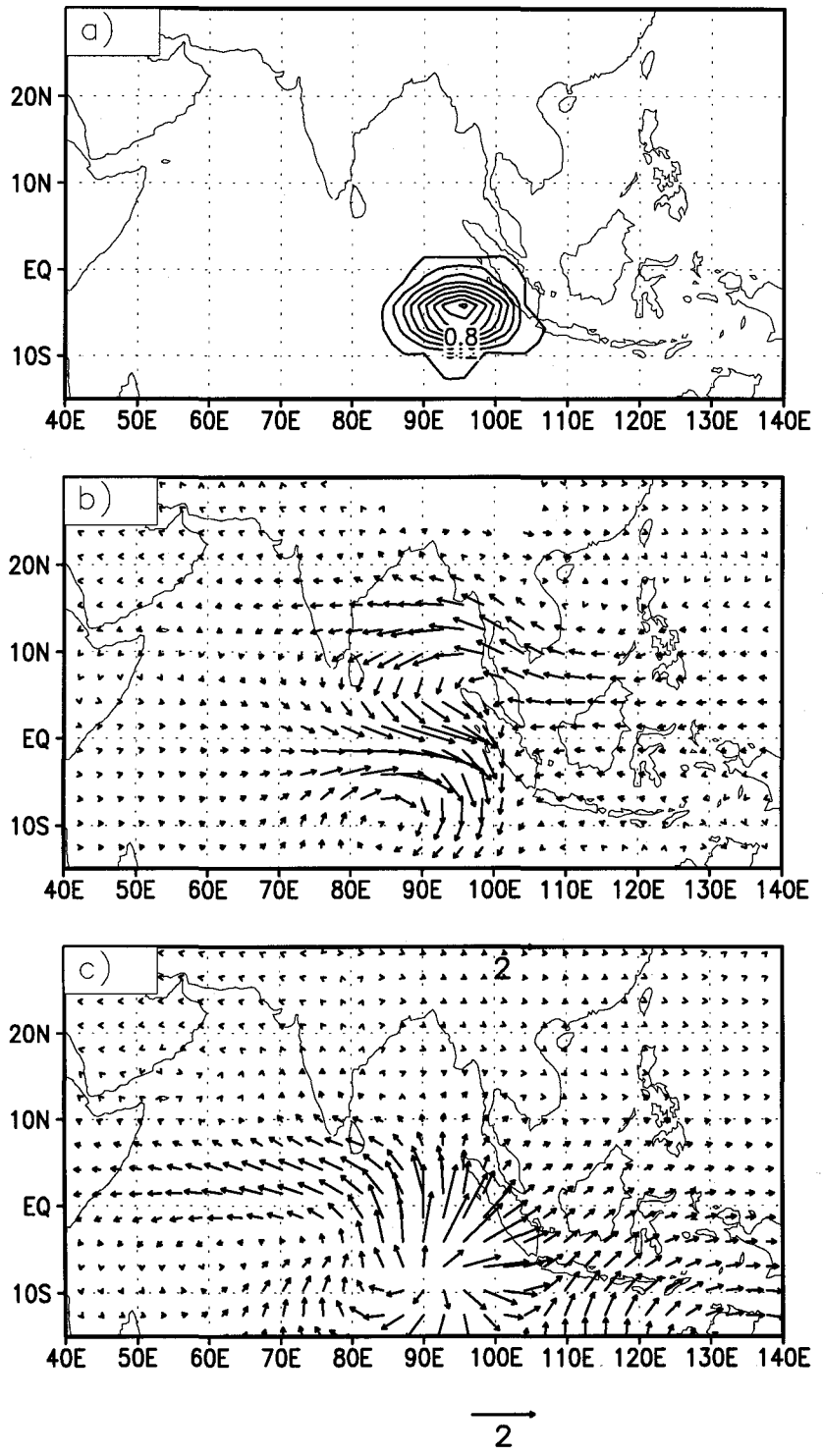

Figure 7.11: The anomalous wind response at 850 hPa (b) and 200 hPa (c) to a heating (a) put at the surface of the equatorial eastern Indian Ocean. The maximum amplitude of the heating rate is $2°Cday^{-1}$.

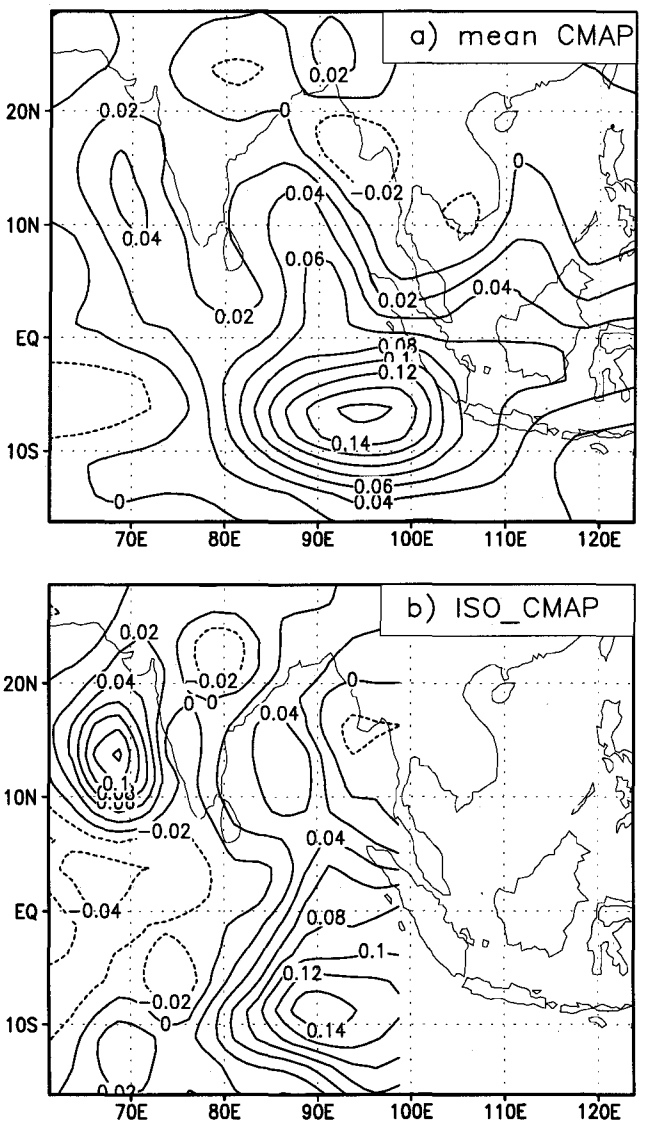

Figure 7.12: The dominant SVD mode between May-Sept mean CMAP and the CMAP boreal summer ISO intensity in May-Sept 1979-2001. They account for 39.7% of the total covariance, compared with 14.7% from the second dominant mode. The dominant mode of the mean CMAP (a) contributes to 22.6% of its total variance. The dominant mode of the boreal summer ISO intensity (b) contributes to 14.6% of its total variance. Correlation between the two temporal coefficients of the first SVD mode is 0.81.

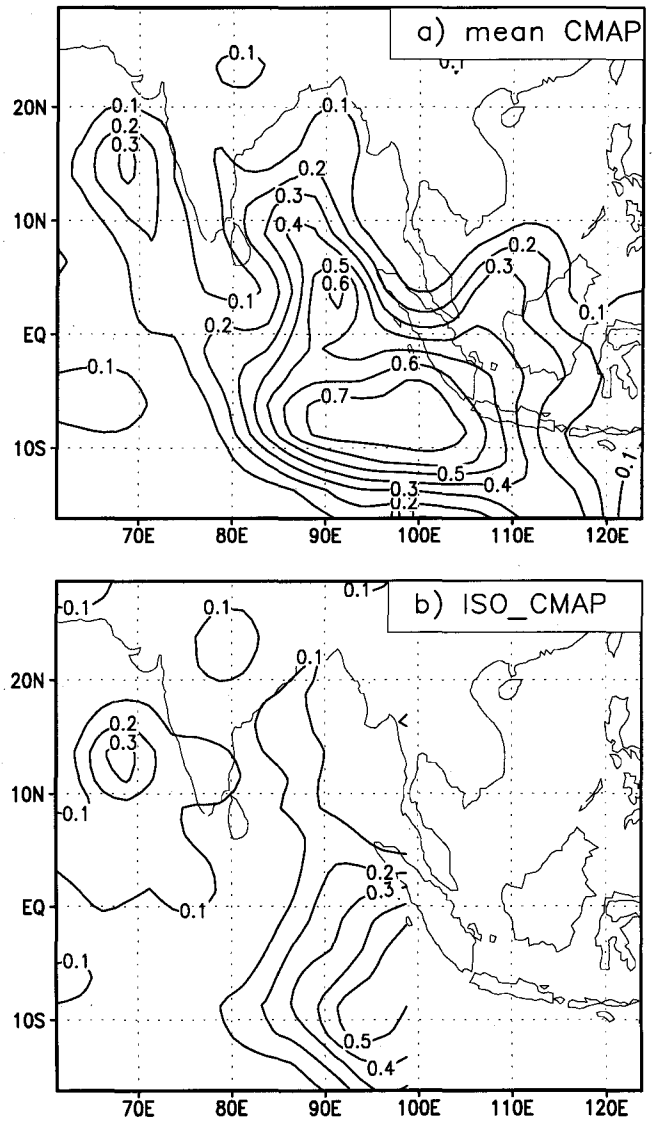

Figure 7.13: Fractional variance that the first SVD mode (Fig. 7.12) contributes to the interannual variance of a) the May-Sept mean CMAP and b) the boreal summer ISO intensity using CMAP at each individual grid point in May-Sept from 1979 to 2001. The values are in percentage.

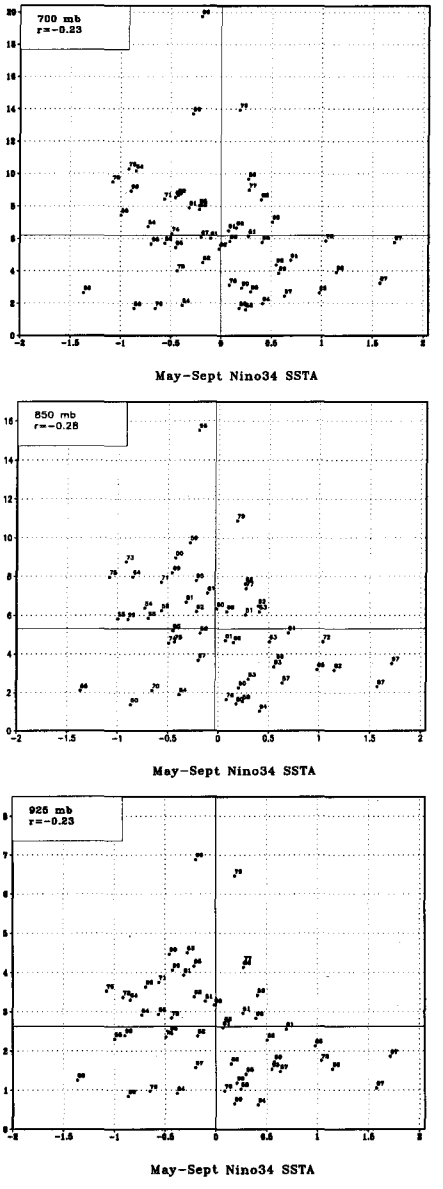

Figure 7.14: Scatter plot of the 20-50-day mean variance of the northward propagating zonal wind vs. Nino3.4 SST. The upper, middle and lower panel are for the zonal wind at 700, 850, and 925 hPa respectively.

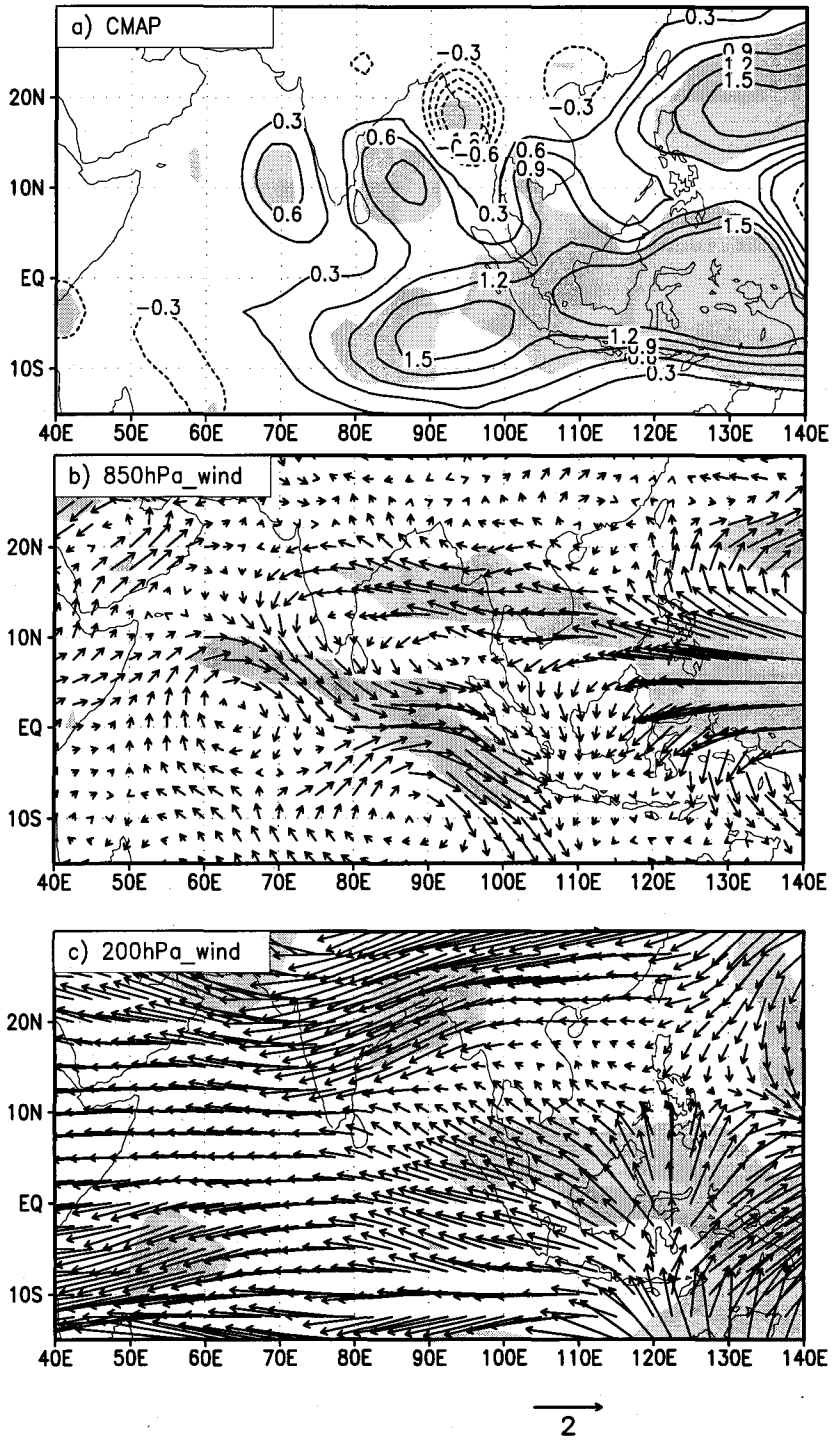

Figure 7.15: Same as Fig. 7.10 but for the composite difference between yeas with May-Sept Nino3.4 smaller (1981, 1984, 1985, 1988, 1989, 1995, 1996, 1998, 1999, 2000) and larger (1979, 1980, 1982, 1983, 1986, 1987, 1990, 1991, 1992, 1993, 1994, 1997 and 2001) than zero.

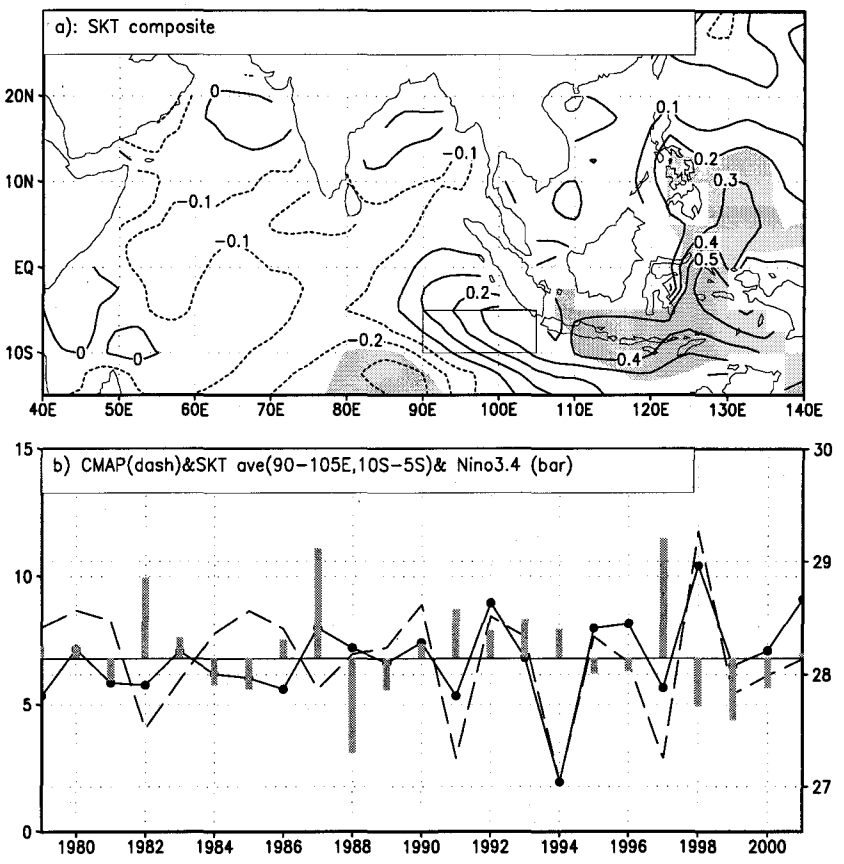

Figure 7.16: (a) Same as Fig. 7.10 but for SST; (b) Domain averaged CMAP (dash) and SST (solid) at 90°E-105°E, 10°S-5°S and Nino3.4 SST anomaly during 1979-2001.

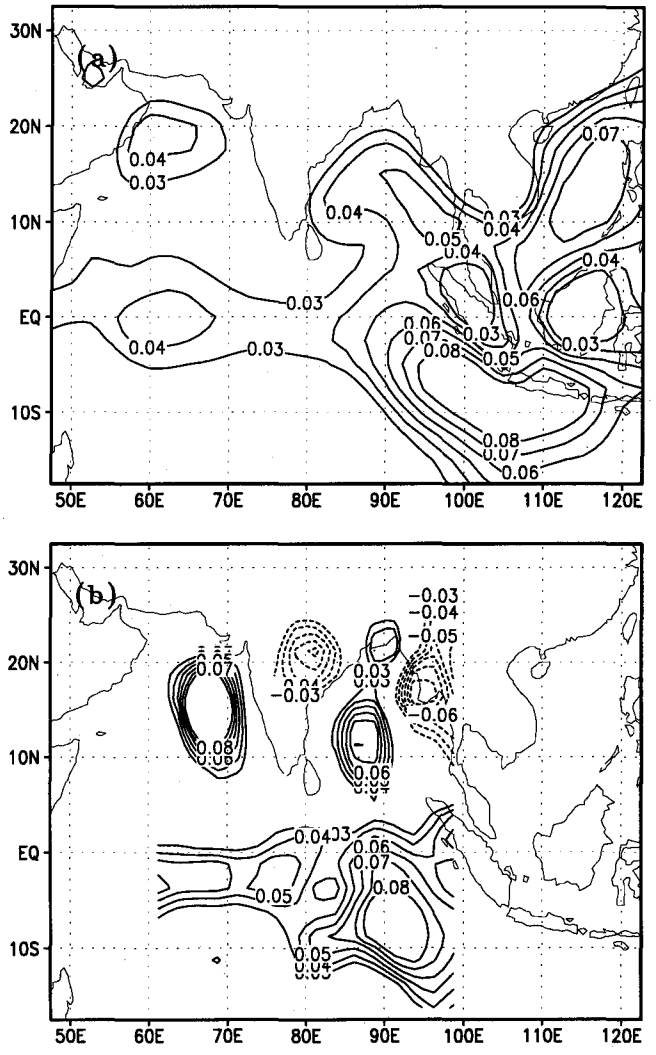

Figure 7.17: The dominant SVD mode between May-Sept mean SST and the CMAP boreal summer ISO intensity in May-Sept 1979-2001. They account for 50.3% of the total covariance, compared with 22.0% from the second dominant mode. The dominant mode of the mean SST (a) contributes to 36.5% of its total interannual variance. The dominant mode of the boreal summer ISO intensity (b) contributes to 12.7% of its total interannual variance. Correlation between the two temporal coefficients of the first SVD mode is 0.79.

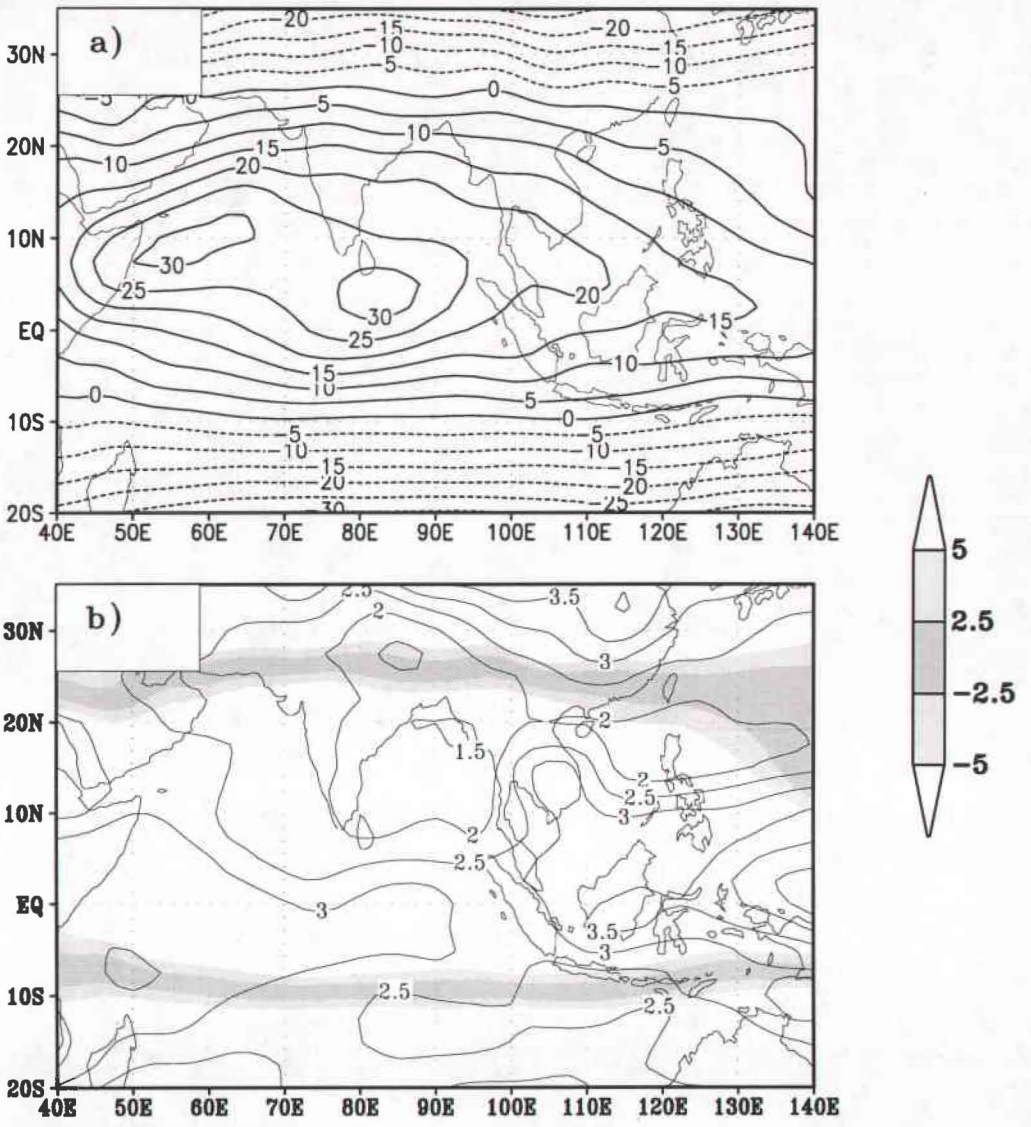

Figure 7.18: a) average and b) standard deviation of $u_{850} - u_{200}$ vertical wind shear during 1948-2001.

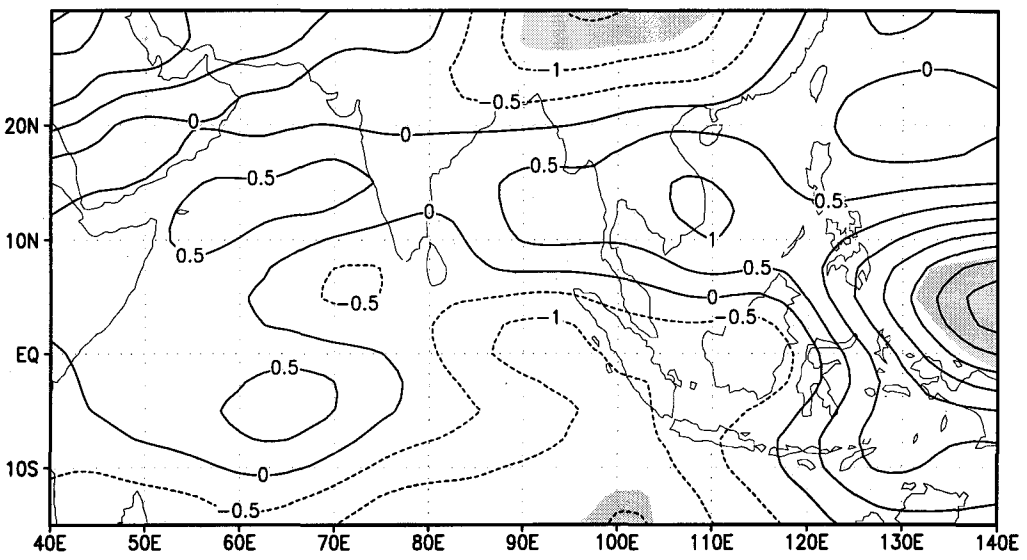

Figure 7.19: Same as Fig. 7.10 but for $u_{850} - u_{200}$ zonal wind shear.

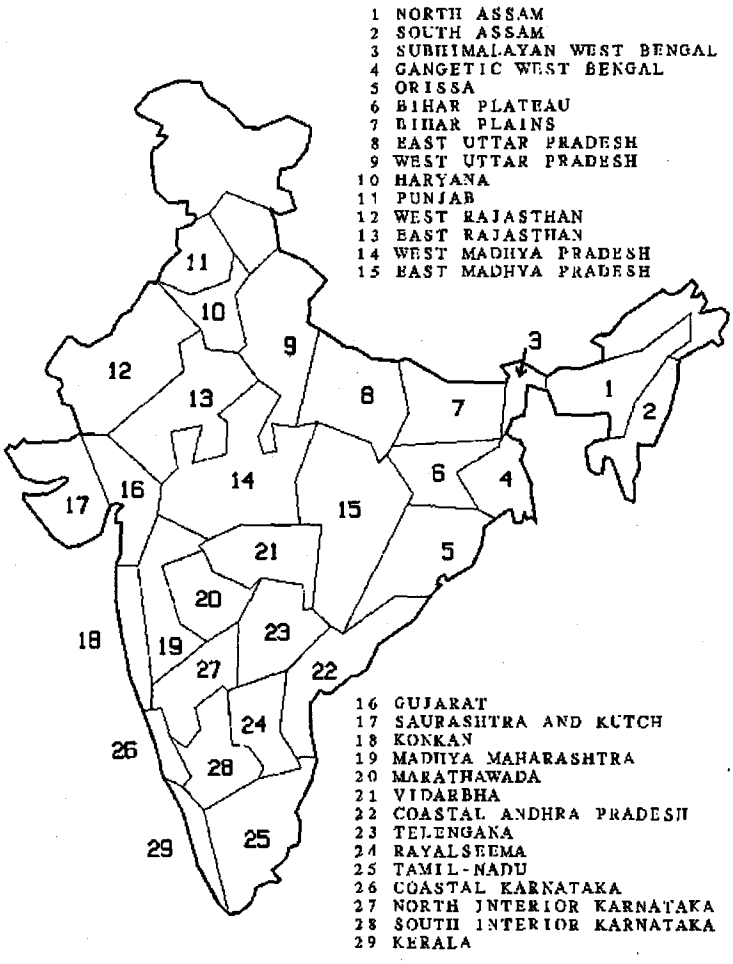

Figure 7.20: Map of the 29 India subdivisions.

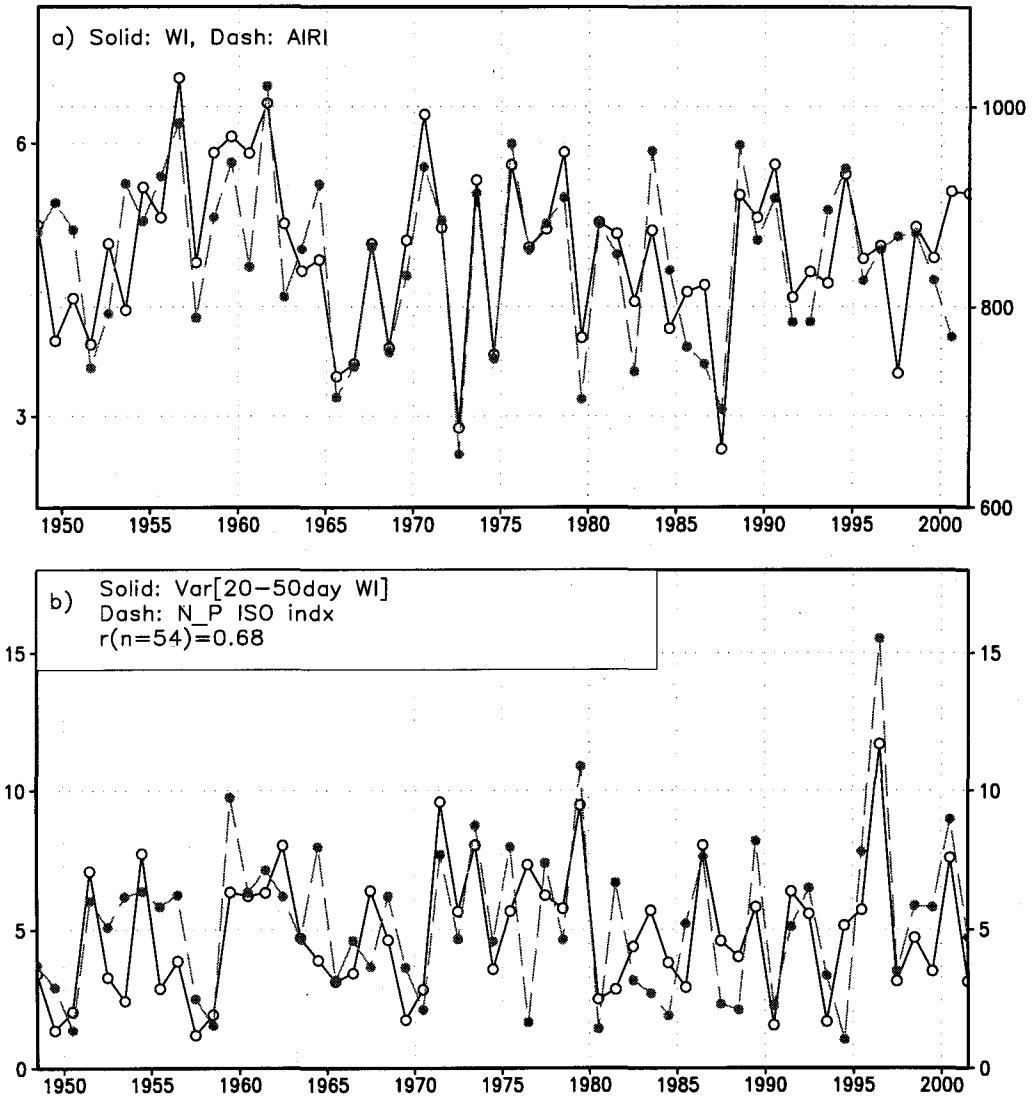

Figure 7.21: May-September Variance of 20-50-day Wang and Fan index (solid) and the northward propagating ISO index (dash). The 54-year correlation coefficient of the two time series is 0.68.

Chapter 8

Summary and Future Work

8.1 Tasks performed in this study

In this study, the following tasks have been performed to investigate the interannual variability of the boreal summer ISO:

1. A new diagnostic approach was proposed to quantify the wave characteristics (intensity, frequency and propagation) of the three summertime ISO modes, including the MJO, the northward propagating ISO in the Indian summer monsoon region and the northwestward propagating ISO in the WNP.

2. The summertime ISO is distinguished from the wintertime MJO in regard to the distribution of the variability center and the horizontal and vertical structures.

3. The interannual variations of the three summertime ISO modes are investigated. A high-resolution life cycle of the ISO in the Indian Ocean was produced by a composite study using the recent TMI and QuikSCAT satellite data. How the interannual variations of the ISO are related to the large-scale change, includ-

ing the mean circulation, convection, and SST are discussed. The ISO-Indian summer monsoon relationship was also investigated.

8.2 Major results

Unlike the wintertime MJO, strong ENSO-ISO linkages exist in the Asian-Pacific summer monsoon region in the boreal summer. The overall ISO intensity at each grid point, which includes both the standing and the propagating variances, has the most pronounced interannual variations in the WNP. The interannual variations of the ISO in the Indian summer monsoon region are much weaker.

By using the wavenumber-frequency analysis, the intensity of the propagating waves in each season is measured. The MJO and the Jul-Oct northwestward propagating ISO in the WNP are closely linked with ENSO. How *El Niño* modifies these modes are summarized in Fig.8.1. During May-Jul, Nino3.4 SST anomaly is usually mild compared with its peak phase in the winter, but it causes significant remote impacts in Indo-Pacific monsoon region. Enhanced mean rainfall at East African coast and the western Indian Ocean and suppressed rainfall in the Maritime Continent are produced. There is also deficient rainfall at 10°N in the Bay of Bengal. The overall MJO is enhanced, despite that local intraseasonal variability in the Maritime Continent does not intensify. The arrows in Fig.8.1a denote a stronger eastward propagation. After the WNP monsoon breaks out in July, enhanced convection band protrudes to 10°N in the WNP and suppressed mean rainfall area expands to Taiwan

and the ocean to the southeast of Japan (Fig.8.1b). The drought area in the Maritime Continent also extends westward to 80°E, 10°S over the southern Indian Ocean. Stronger northwestward propagating ISO is found to the east of the Philippines. *La Niña* casts an inverse impact on both the mean state and the ISO modes.

The linkage between ENSO and the northwestward propagating ISO in the WNP can be explained by the vertical wind shear mechanism. The *El Niño* -induced lower-level westerly and upper-level easterly turn the mean vertical wind shear into an easterly shear, which effectively enhances Rossby wave in the lower troposphere. Consequently, stronger ISO is found to migrate northwestward from the equator to the Philippines. The wind shear mechanism also explains why the interannual variations of the ISO in the Indian monsoon region are less pronounced and less sensitive to ENSO compared with those in the WNP.

During *El Niño* , the enhancement of the MJO in May-Jul cannot be explained by the vertical-shear mechanism because the change in vertical shear does not affect the equatorial Kelvin wave (Wang and Xie 1996). However, *El Niño* suppresses May-Jul mean rainfall over Indonesia and enhances mean rainfall in the equatorial western Indian Ocean and the equatorial central-western Pacific (Fig.8.1a). On the intraseasonal time scale, the total 10-90-day OLR variances increase between 30°E and 90°E and between 140° and 180°E. Due to a stronger MJO, the local 10-90-day OLR variance does not decrease in the Maritime Continent, although the mean convection drops significantly. The active convection in the western Indian Ocean

favors initiation of the MJO, and that in the western and central Pacific facilitates MJO's re-intensification. These factors may contribute to the enhancement of the MJO. After the northwestward propagating ISO dominates in the WNP in Aug-Oct, the MJO reaches the weakest phase in the year. Deficient rainfall is found west of Sumatra as *El Niño* develops. Strong southeasterly wind anomaly is produced over the eastern Indian Ocean, inducing upwelling off the coast of Sumatra and cool sea surface to suppress the convection. The center of the MJO also expands to 10°N, accompanied by the annual march of the thermal equator. The involvement of the Asian-Pacific summer monsoon in Aug-Oct may also add to the breakdown of the MJO-ENSO linkage. All these hypotheses remain to be tested by future studies.

The northward propagating ISO in the Indian summer monsoon region is significantly related with the summer mean convection in the EEIO. The recent satellite datasets reveal that the northward propagating ISO is resulted from Rossby wave emanation from the large-scale convection in the central and eastern equatorial Indian Ocean. During the *El Niño* developing summer, the subsidence in the Maritime Continent suppresses the mean convection in the EEIO. Consequently, negative correlation exists between the seasonal ISO intensity and the Nino3.4 SST. There is no significant relationship between the seasonal activities of the ISO and the strength of the Indian summer monsoon.

8.3 Limitations of this study

The present wavenumber-frequency analysis allows quantitatively describing intraseasonal wave characteristics, yet it has its own limitation. The method can only distinguish wave propagation in one-dimension, either in the zonal or the meridional direction. In the WNP, when the ISO propagates northwestward, the assessment made from separate analyses of the zonal and meridional components may induce errors concerning the wavenumber and frequency. The results will be substantiated if the analysis method can be extended to 2-dimension. The current analysis on the northward propagating ISO only focuses on the wavenumber-1 anomaly. Whether the method can be applied to investigate higher-wavenumber northward propagating anomalies at a finite domain needs to be further examined.

Only three years' TMI and QuikSCAT datasets are employed in the present study. The composite reveals that the northward propagation of the ISO from the equator to 15°N closely resembles the Rossby-wave emanation process. The short record here can not exclude possibility of the "independent northward propagation" (Wang and Rui 1990).

The explanation of why a developing *El Niño* can enhance the May-Jul MJO only advanced a hypothesis. In order to fully understand the mechanism, and explain why the MJO shows different sensitivity to ENSO in different seasons, further numerical and theoretical studies are required.

8.4 Future work

During the study, several interesting issues were encountered. They are listed here in hope to motivate some future studies:

1. Close linkages between ENSO and the May-Jul MJO, the northwestward propagating ISO in the WNP, and the northward propagating ISO in the Indian Ocean are found in the present study. How these relationships can be applied in predicting the ISO (Waliser et al. 2003) requires further endeavors.

2. The ISO in the western hemisphere remains unexplored in the present work. It is shown in Chapter 4 that during the boreal winter, the ISO in the northeastern Brazil is linked with the MJO. In the boreal summer, connection with the MJO is found from the far eastern Pacific to the west of Mexico. The ISO in the eastern Pacific has a strong linkage with the intraseasonal variability in the North American summer monsoon (NASM) (Higgins and Shi 2001), although it may not affect the mean strength of the NASM (Yu and Wallace 2000; Higgins and Shi 2001). The hurricane activity in the eastern Pacific and the Gulf of Mexico is also modulated by the MJO (Maloney and Hartmann 2000a,b). Thus the MJO can provide another linkage between the precipitation in Asia and North America, besides the mid-latitude teleconnection (Lau and Weng 2002). It would be interesting to further explore this connection.

3. Why the MJO is enhanced during May-Jul at the *El Niño* 's developing stage

is not understood. The present work linked the enhanced MJO with the ENSO-induced convective anomalies in the western Indian Ocean and the eastern African coast. Whether the central-eastern Pacific plays a possible role should be further investigated.

4. In addition to the 30-60-day oscillation, a biweekly periodicity has long been found in the Indian summer monsoon (Ramanathy 1969; Murakami 1972 and many others). The bi-weekly anomalies propagate westward in the off-equatorial region (Krishnamurti and Ardanuy 1980; Saha et al. 1981). Its synoptic structure and relationship with the 30-60-day oscillation in 1979 were studied by Chen and Chen (1993). Meanwhile, a bi-weekly oscillation also exists in the WNP typhoon activity (Frank 1987). Furthermore, northwestward propagating 6-9-day waves have also been observed in the WNP (Lau and Lau 1990). The present study showed a broad intraseasonal spectrum in the WNP, but it did not further distinguish those frequencies. There are many questions related to the interactions between the higher- and lower- frequencies, such as: Whether the bi-weekly oscillation has different dynamic structure from the 30-60-day oscillation? How does the different scales interact (Lander 1994; Holland 1995; Maloney and Dickinson 2003)? The bi-weekly mode that propagates from the South China Sea to the Bay of Bengal has a significant relationship with ENSO (Chen and Weng 1998, 1999). How it is related to the interannual variations of the WNP ISO also requires more future efforts.

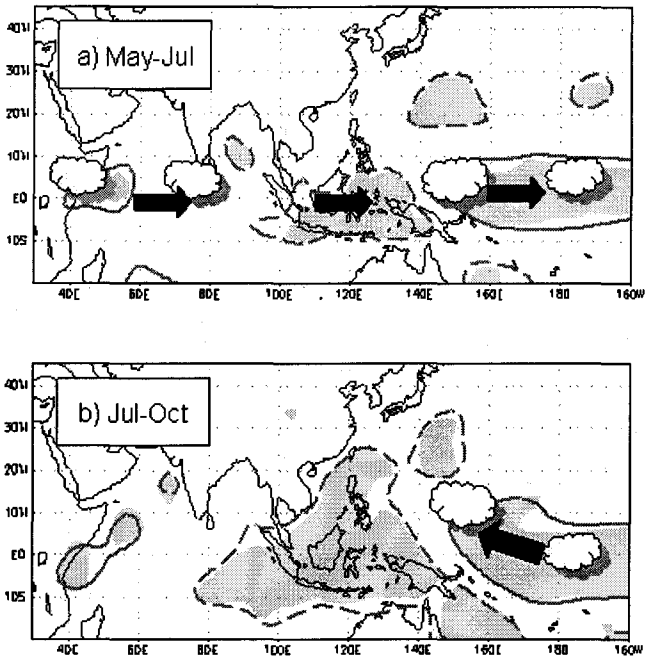

Figure 8.1: Schematic diagram that describes how El Niño modifies (a) the May-Jul MJO and (b) the northwestward propagating ISO in Jul-Oct. Solid and dash contours indicate the region where (a) May-Jul and (b) Jul-Oct mean CMAP rainfall has positive and negative correlation with May-Oct mean Nino3.4 SST anomaly. Shading within the contour shows correlation above the 95% confidence level. Black arrow denotes that (a) the MJO is enhanced in May-Jul and (b) the northwestward propagating ISO is enhanced over the western North Pacific in Jul-Oct in an El Niño summer.

REFERENCE

Allan, R. D. Chambers, W. Drosdowsky, H. Hendon, M. Latif, N. Nicholls, I. Smith, R. Stone, Y. Tourre, 2001: Is there an Indian Ocean dipole, and is it independent of the El Nino - Southern Oscillation? *CLIVAR Exchange*, **6**.

Annamalai, H. and J. M. Slingo, 2000: Active/break cycles: Diagnosis of the intraseasonal variability of the Asian summer monsoon. *Climate Dynamics*.

Annamalai, H. and B. Wang, 2003: Interannual variation of the boreal summer intra-seasonal variability: Role of the low-frequency large and regional scale circulations. *submitted J. Climate.*.

Anyamba, E. K. and B.C. Weare, 1995: Temporal variability of the 40-50 day oscillation in tropical convection. *Int. J. Climatol.*, **15**, 379-402.

Blackmon, M. L., Y.-H. Lee and J. M. Wallace, 1984: Horizontal structure of 500 mb height fluctuations with long, intermediate and short time scale. *J. Atmos. Sci.*, **41**, 961-979.

Chang, C.-P., 1977: Viscous internal gravity waves and low-frequency oscillations in the tropics. *J. Atmos. Sci.*, **34**, 909-910.

Chang, C.-P. and H. Lim, 1988: Kelvin-wave CISK: A possible mechanism for the 30-50 day oscillation. *J. Atmos. Sci.*, **45**, 1709-1720.

Charney, J. G. and J. Shukla, 1981: Predictability of monsoon. *Monsoon Dynamics*, J. Lighthill and R. P. Pearce, Eds, Cambridge University Press, 99-108.

Chen, T-C and J-M Chen, 1993: The 10-20-day mode of the 1979 Indian monsoon: its relation with the time variation of monsoon rainfall. *Mon. Wea. Rev.*, **121**, 2465-2482.

Chen, T-C and S-P Weng, 1998: Interannual variation of the summer synoptic-scale disturbance activity in the western tropical Pacific. *Mon. Wea. Rev.*, **126**, 1725-1733.

Chen, T-C and S-P Weng, 1999: Interannual and intraseasonal variations in monsoon depressions and their westward-propagating predecessors. *Mon. Wea. Rev.*, **127**, 1005-1020.

H. L. Drbohlav and B. Wang, 2003: Mechanism of intraseasonal oscillation in the South Asian summer monsoon region. *submitted J. Climate.*.

Deland, R. J., 1964: Travelling planetary waves. *Tellus*, **16**, 271-273.

Emanuel, K. A., 1987: An air-sea interaction model of intraseasonal oscillations in the tropics. *J. Atmos. Sci.*, **44**, 2324-2340.

Ferranti, L, J.M. Slingo, T.N. Palmer and B.J. Hoskins, 1997: Relations between interannual and intraseasonal monsoon variability as diagnosed from AMIP intergrations. *Quart. J. Roy. Meteor. Soc.*, **123**, 1323-1357.

Fink, A. and E. Speth, 1997: Some potential forcing mechanisms of the year-to-year variability of the tropical convection and its intraseasonal (25-70-day) variability. *Int. J. Climatol.*, **17**, 1513-1534.

Fu, X., B. Wang, T. Li, and J.P. McCreary, 2003: Coupling between northward propagating, intraseasonal oscillations and sea-surface temperature in the Indian Ocean. *jas*, **60**, 60, 1733-1783.

Gray, B.M. , 1988: Seasonal frequency variations in the 40-50 day oscillation. *J. Climatol.*, **8**, 511-519.

Gill, A. E., 1980: Some simple solutions for heat-induced tropical circulations. *Quart. J. Roy. Meteor. Soc.*, **106**, 447-462.

Gutzler, D.S., 1991: Interannual fluctuations of intraseasonal variance of near-equatorial zonal winds. *J. Geophys. Res.*, **96**, 3173-3185.

Hartmann, D.L., M.L. Michelsen, and S.A. Klein, 1992: Seasonal variations of tropical intraseasonal oscillations: a 20-25-day oscillation in the western Pacific. *J. Atmos. Sci.*, **49**, 1277-1289.

Hayashi, Y., 1971: A generalized method of resolving disturbances into progressive and retrogressive waves by space Fourier and time cross-spectral analysis. *J. Meteor. Soc. Japan*, **49**, 125-128.

Hayashi, Y., 1982: Space-time spectral analysis and its applications to atmospheric

waves. *J. Meteor. Soc. Japan*,**60** , 156-171.

Hayashi Y. and D.G. Golder, 1993: Tropical 40-50- and 25-30-day oscillation appearing in realistic and idealized GFDL climate models and the ECMWF data set. *J. Atmos. Sci.*, **50**, 464-494.

Hendon, H. H., C. Zhang, and J. Glick, 1999: Interannual variation of the Madden-Julian oscillation during austral summer. *J. Climate*, **12**, 2538-2550.

Hendon, H. H., 2003: Indonesian rainfall variability: Impacts of ENSO and local air-sea interaction. *J. Climate*, **16**, 1775-1970.

Higgins, R. W. and W. Shi, 2001: Intercomparison of the principal modes of interannual and intraseasonal variability of the North American monsoon system. *J. Climate*, **14**,403-417.

Holland, G. J. 1995: Scale interaction in the western Pacific monsoon. *Meteorol. Atmos. Phys.*, **56**, 57-79.

Hsu, H.-H. and C.-H. Wen, 2001: Northward propagation of the intraseasonal oscillation in the western North Pacific during the boreal summer: Structure and mechanism. *J. Climateaccepted.*

Jiang, X., T. Li, and B. Wang: Structures and Mechanisms of the Northward Propagating Boreal Summer Intraseasonal Oscillation. *J. Climateaccepted.*

Kalnay, E. and co-authors, 1996: The NCEP/NCAR 40-year reanalysis project. *Bull. Amer. Meteor. Soc.*, **77**, 437-471.

Kao, S. K., 1968: Governing equations and spectra for atmospheric motion and transports in frequency-wavenumber space. *J. Atmos. Sci.*, **25**, 32-38.

Kao, S. K., 1970: Wavenumber-frequency spectra of temperature in the free atmosphere. *J. Atmos. Sci.*, **27**, 1000-1007.

Kayano, M. T. and V. E. Kousky, 1999: Intraseasonal (30-60 day) variability in the global tropics: principal modes and their evolution. *Tellus*, **51A**,373-386.

Kemball-Cook, S. and B. Wang, 2001: Equatorial waves and air-sea interaction in the boreal summer intraseasonal oscillation. *J. Climate*, **14**, 2923-2942.

Kessler, W. S. 2001: EOF Representations of the Madden-Julian Oscillation and Its Connection with ENSO. *J. Climate*, **14**, 3055-3061.

Knutson T. R. and K. M. Weickmann, 1987: 30-60 day atmospheric oscillations: Composite life cycles of convection and circulation anomalies. *Mon. Wea. Rev.*, **115**, 1407-1436.

Krishnamurti, T. N., and D. Subrahmanyam, 1982: The 30-50 day mode at 850 mb during MONEX. *J. Atmos. Sci.*, **39**, 2088-2095.

Krishnamurti, T. N., and P. Ardanuy, 1980: The 10- to 20-day westward propagating mode and "breaks in the monsoons." *Tellus*, **32**, 15-26.

Lander, M., 1994: Description of a monsoon gyre and its effects on the tropical cyclones in the western Pacific during August 1991. *Wea. and Forecasting*, **9**,640-654.

Lau, K.-H. and N.-C. Lau, 1990: Observed structure and propagation characteristics of tropical summertime synoptic scale disturbances. *Mon. Wea. Rev.*, **118**, 1888-1912.

Lau, K.-M. and L. Peng, 1987: Origin of low frequency (intraseasonal) oscillation in the tropical atmosphere. Part I. The basic theory. *J. Atmos. Sci.*, **44**, 950-972.

Lau, K.-M. and P.H. Chan, 1986: Aspects of the 40-50 day oscillation during the northern summer as inferred from outgoing longwave radiation. *Mon. Wea. Rev.*, **144**, 1354-1367.

Lau, K.-H. and N.-C. Lau, 1990: Observed structure and propagation characteristics of tropical summertime synoptic scale disturbances. *Mon. Wea. Rev.*, **118**, 1888-1913.

Lau, K.-M. and P.H. Chan, 1988: Intraseasonal and interannual variations of tropical convection: A Possible Link between the 40-50 Day Oscillation and ENSO? *J. Atmos. Sci.*, **45**, 506-521.

Lau, K.-M. and H. Weng, 2002: Recurrent teleconnection patterns linking summertime precipitation variability over East Asia and North America. *J. Meteor. Soc. Japan*, **80**,1309-1324.

Lawrence, D. M. and P. J. Webster, 2001: Interannual variations of the intraseasonal oscillation in the South Asia summer monsoon region. *J. Atmos. Sci.*, **14**, 2910-2922.

Li, T. and B. Wang, 1994: The influence of sea surface temperature on the tropical intraseasonal oscillation: A numerical experiment. *Mon. Wea. Rev.*, **122**, 2349-2362.

Liemann, B. and C.A. Smith, 1996: Description of a a complete (interpolated) outgoing longwave radiation data set. *Bull. Amer. Meteor. Soc.*, **77**, 1275-1277.

LinHo and Wang, 2001: The time-space structure of the Asian-Pacific summer monsoon - A fast annual cycle view. *submitted to J. Climate.*

Madden, R. A. and P. R. Julian, 1971: Detection of a 40-50 day oscillation in the zonal wind in the tropical Pacific. *J. Atmos. Sci.*, **28**, 702-708.

Madden, R. A. and P. R. Julian, 1972: Description of global scale circulation cell in the tropics with a 40-50 day period. *J. Atmos. Sci.*, **29**, 1109-1123.

Madden, R. A., 1986: Seasonal variations of 40-50 day oscillation in the tropics. *J. Atmos. Sci.*, **43**,3138-3158.

Madden, R.A. and P.R. Julian, 1994: Observations of the 40-50-day tropical oscillation - A review. *Mon. Wea. Rev.*, **122**, 814-837.

Matsuno, T., 1966: Quasi-geostrophic motions in the equatorial area. *J. Meteor. Soc. Japan*, **44**, 25-43.

Mehta, A.V. and T.N. Krishnamurti, 1988: Interannual variability of the 30 to 50 Day Wave motions. *J. Meteor. Soc. Japan*, **66**, 535-547.

Maloney, E. D., and D. L. Hartmann, 2000a: Modulation of eastern North Pacific hurricanes by the Madden-Julian oscillation. *J. Climate*, **13**, 1451-1460.

Maloney, E. D., and D. L. Hartmann, 2000b: Modulation of Hurricane Activity in the Gulf of Mexico by the Madden-Julian Oscillation. *Science*, **287**, 2002-2004.

Murakami, T., 1972: Equatorial tropospheric waves induced by diabatic heating sources. *J. Atmos. Sci.*, **29**, 827-836.

Neelin, J. D., I. M. Held and K. H. Cook, 1987: Evaporation-wind feedback and low-frequency variability in the tropical atmosphere. *J. Atmos. Sci.*, **44**,2341-2348.

Nitta, T., 1987: Convective activities in the tropical western Pacific and their impact on the Northern Hemisphere summer circulation. *J. Meteor. Soc. Japan*, **65**, 373-389.

Park, C.-K., D. M. Straus and K.-M. Lau, 1990: An evaluation of the structure of tropical intraseasonal oscillations in three general circulation models. *J. Meteor. Soc. Japan*, **68**, 403-417.

Pratt, R. W., 1976: The interpretation of space-time spectral quantities. *J. Atmos. Sci.*, **32**, 1283-1300.

Parthasarathy, B., A.A. Munot, and D.R. Kothawale, 1995 : Monthly and seasonal rainfall series for All-India homogeneous regions and meteorological subdivisions: 1871-1994. Contributions from Indian Institute of Tropical Meteorology, Research Report RR-065, Aug. 1995, Pune 411 008 INDIA.

Ramanthy, K., 1969: Some aspects of the break in the Indian southwest monsoons during July and August. *Forecasting Manual*, **Iv-18.3**, India Meteorological Department, 1-57.

Rui, H. and B. Wang, 1990: Development characteristics and dynamics structure of tropical intraseasonal convection anomalies. *J. Atmos. Sci.*, **47**, 357-379.

Salby, M. L. and H. H. Hendon, 1994: Intraseasonal behavior of clouds, temperature, and motion in the Tropics. *J. Atmos. Sci.*, **51**, 2207-2224.

Saha, K., F. Sanders, and J. Shukla, 1981: Westward propagating predecessors of monsoon depressions. *Mon. Wea. Rev.*, **109**, 330-343.

Saji, N. H., B. N. Goswami, P. N. Vinayachandran, and T. Yamagata, 1999: A dipole mode in the tropical Indian Ocean. *Nature*,**401**, 360-363.

Singh, S.V., R.H. Kripalani, and D.R. Sikka, 1992: Interannual variability of the Madden-Jullian oscillations in Indian summer monsoon rainfall. *J. Climate*, **5**,

973-978.

Slingo JM, and coauthors, 1996: Atmospheric Model Intercomparison Project (AMIP) intraseasonal oscillations in 15 atmospheric general circulation models. *cd*, **12**, 325-357.

Sperber, K.R., J.M.Slingo, P.M.Inness, K.-M. Lau, 1997: On the maintenance and initiation of the intraseasonal oscillation in the NCEP/NCAR reanalysis and in the GLA and UKMO AMIP simulations. *Climate Dynamics*, **13**, 769-795.

Sperber, K.R. and J. M. Slingo, 2002: Propagation and vertical structure of the Madden-Julian Oscillation. Proceedings from Program for the 27th Annual Climate Diagnostics and Prediction Workshop.

Ueda, H., T. Yasunari and R. Kawamura, 1995: Abrupt seasonal change of large-scale convective activity over the western Pacific in the northern summer. *J. Meteor. Soc. Japan*, **73**, 795-809.

Vecchi, G. and D. E. Harrison, 2001: Monsoon breaks and sub-seasonal sea surface temperature variability in the Bay of Bengal. *J. Climate*, **15**, 1485-1493.

Wang, B. and H. Rui, 1990: Synoptic climatology of transient tropical intraseasonal convection anomalies: 1975-1985. *Meteorol. Atmos. Phys.*, **44**, 43-61.

Wang, B. and H. Rui, 1990b: Dynamics of the coupled moist Kelvin-Rossby wave on an equatorial beta plane. *J. Atmos. Sci.*, **47**, 397-413.

Wang, B. and Y. Ding, 1992: An overview of the Madden-Julian oscillation and its relation to monsoon and mid-latitude circulation. *Adv. Atmos. Sci.*, **1**, 93-111.

Wang, B. and X. Xie, 1996: Low-frequency equatorial waves in vertically sheared zonal flow. Part I : Stable waves. *J. Atmos. Sci.*, **53**, 449-467.

Wang, B. and X. Xie, 1997: A model for the boreal summer Intraseasonal Oscillation. *J. Atmos. Sci.*, **54**, 72-86.

Wang, B. and X. Xu, 1997: Northern Hemisphere summer monsoon singularities and climatological intraseasonal oscillation. *J. Climate*, **10**, 1071-1085.

Wang,B., R. Wu and X. Fu, 2000: Pacific-East Asian teleconnection: How does ENSO affect East Asian Climate? *J. Climate*, **13**, 1517-1536.

Wang, B., Chan, Johnny C. L.. 2002: How Strong ENSO Events Affect Tropical Storm Activity over the Western North Pacific. *J. Climate*, **15**, 1643-1658.

Wang, X.L. and Murakami, T., 1988: Intraseasonal disturbance activity before, during and after the 1982-1983 ENSO. *J. Atmos. Sci.*, **45**, 3754-3770.

Weare and Nasstrom, 1982: Examples of extended empirical orthogonal function analysis. *Mon. Wea. Rev.*, **110**, 481-485.

Webster, P. J., 1983: Mechanisms of monsoon low-frequency variability: Surface hydrological effects. *J. Atmos. Sci.*, **40**, 2110-2124.

Webster, P. J., A. M. Moore, J. P. Loschnigg, and R. R. Leden, 1999: Coupled ocean-atmosphere dynamics in the Indian Ocean during 1997-98. *Nature*, **401**, 356-360.

Webster, P. J. and co-authors, 2002: The JASMINE pilot study. *Bull. Amer. Meteor. Soc.*, **83**, 1603-1630.

Wheeler, M. and G. N. Kiladis, 1999: Convectively coupled equatorial waves: Analysis of clouds and temperature in the wavenumber-frequency domain. *J. Atmos. Sci.*, **56**, 374-399.

Wilks, D. S., 1995: Statistical methods in the atmospheric sciences. Academic Press, 467pp.

Xie, P. and P. A. Arkin, 1997: Global precipitation: A 17-Year monthly analysis based on gauge observations, satellite estimates and numerical model outputs. *Bull. Amer. Meteor. Soc.*, **78**, 2539-2558.

Xie, S.-P., H. Annamalai, F.A. Schott, and J.P. McCreary, 2001: Structure and mechanisms of South Indian Ocean climate variability. *J. Climate*, in press.

Xie, X. and B. Wang, 1996: Low-frequency equatorial waves in vertically sheared zonal flow. Part II: Unstable waves. *J. Atmos. Sci.*, **53**, 3589-3605.

Yasunari, T., 1979: Cloudiness fluctuations associated with the Northern hemisphere summer monsoon. *J. Meteor. Soc. Japan*, **57**, 227-242.

Yasunari, T., 1980: A quasi-stationary appearance of 30 to 40 day period in the cloudiness fluctuations during the summer monsoon over India. *J. Meteor. Soc. Japan*, **58**, 225-229.

Zhu, B. and B. Wang, 1993: The 30-60-Day convection seesaw between the tropical Indian and western Pacific oceans. *J. Atmos. Sci.*, **50**, 184-199.